

**RADIATION AND THERMAL PROCESSING OF ICES AND  
SURFACES RELEVANT TO PREBIOTIC CHEMISTRY IN THE  
SOLAR SYSTEM AND INTERSTELLAR REGIONS**

A Thesis  
Presented to  
The Academic Faculty

by

Margaret Michele Dawley

In Partial Fulfillment  
of the Requirements for the Degree  
Doctor of Philosophy in the  
School of Chemistry and Biochemistry

Georgia Institute of Technology  
May 2013

Copyright © Margaret Michele Dawley 2013

**RADIATION AND THERMAL PROCESSING OF ICES AND  
SURFACES RELEVANT TO PREBIOTIC CHEMISTRY IN THE  
SOLAR SYSTEM AND INTERSTELLAR REGIONS**

Approved by:

Dr. Thomas M. Orlando, Advisor  
School of Chemistry and Biochemistry  
*Georgia Institute of Technology*

Dr. Jiri Janata  
School of Chemistry & Biochemistry  
*Georgia Institute of Technology*

Dr. Facundo M. Fernandez  
School of Chemistry and Biochemistry  
*Georgia Institute of Technology*

Dr. Carol Paty  
School of Earth and Atmospheric Sciences  
*Georgia Institute of Technology*

Dr. Nicholas V. Hud  
School of Chemistry and Biochemistry  
*Georgia Institute of Technology*

Date Approved: February 4, 2013

*To my family,  
for your love, support, and encouragement*

## ACKNOWLEDGEMENTS

Several scientists (and non-scientists) have been instrumental to my success and academic development culminating in this graduate thesis. First, I would like to express my sincere gratitude to my advisor, Professor Thomas Orlando, for his patient guidance, encouragement, advice, and useful constructive criticism. The fundamental knowledge and technical experience I have gained in his lab will be invaluable to my future career. Also, this thesis would not have been possible without my committee members: Dr. Facundo Fernandez, Dr. Jiri Janata, Dr. Carol Paty, Dr. Nicholas Hud, and Dr. Paul Wine (former member), who have assisted with its successful completion and who have been very helpful throughout graduate school. Many current and former lab mates have been a great source of expertise, advice, and friendship. The research scientists, Dr. Alexandr Aleksandrov and Dr. Gregory Grieves, have always been willing and able to answer my scientific and technical questions along the way. Greg has been particularly helpful with Labview questions, and Alex can make a sample holder out of anything. Of particular note, I am indebted to several current and former post-docs, Dr. Jason L. McLain, Dr. Kristin Shepperd, Dr. Heather Abbott-Lyon, and Dr. Claire Pirim, for their help and recommendations regarding the challenging research and technical questions I faced. I will always value their friendship and remember fondly the comic relief they provided. Other current and former lab mates include: Dr. Christopher Lane, Dr. Doogie Oh, Lan Sun, Dr. Babajide Olanrewaju, Irene Anestis-Richard, Marcus Johnson, Torri Rose, Hannah Barks, Michael J. Poston, Alice Johnson DeSimone, Dr. Anton Sidorov, Joshua Symonds, Dr. Jianming Shi,

Dr. Reuben Gaan, and Dr. Chris Bennett. The Orlando Group (EPICS lab) has always provided frank but useful advice for each other, and I am grateful for having been a member of a lab filled with so many intelligent and talented colleagues, many of whom I consider close friends.

In addition, I give my appreciation to our theoretical collaborators, Dr. Andrea Michalkova Scott, Dr. Francis C. Hill, Dr. Jerzy Leszczynski, Dr. Vinh Son Nguyen, and Dr. Minh Tho Nguyen. Andrea was particularly helpful and accessible for any questions I had in regards to her calculations and with writing the kaolinite papers. The Center for Chemical Evolution, NSF, and NASA provided funding for my projects and are appreciated for their support. Many parts for the chamber I built were bought with supply money provided by the GT Department of Chemistry GAANN Fellowship (U.S. Department of Education), and I am grateful for that support as well.

This thesis would not have been possible without the constant love, support, and encouragement of my entire family. I would particularly like to thank my husband, Dr. Denis A. Sokolov, for his love, kind words, strength, and for the long nights debating over important scientific principles. His scientific creativity inspires me everyday. My Russian in-laws are also supportive, even though I have yet to learn Russian. My family, Tonia Nelson, Alexandria Nelson, and Helen Broadwater, are always there to lend an ear. I also thank my friends, Robert and Susan Ainsworth and Dr. Dmitry V. Liskin for the fun times and stimulating conversation. Finally, I owe my deepest thanks to my father, Michael L. Dawley, who first taught me that scientific curiosity can lead to exciting new discoveries. From my first science fair project and all the way through college, his love and encouragement through the years has been unwavering.

# TABLE OF CONTENTS

	Page
ACKNOWLEDGEMENTS .....	iv
LIST OF TABLES .....	xii
LIST OF FIGURES .....	xiv
SUMMARY .....	xviii
 <u>CHAPTER</u>	
I INTRODUCTION .....	1
1.1 Importance of Studying Organic-Mineral Interfaces Relevant to Prebiotic Chemistry .....	1
1.2 Relevance of Thermal Processing .....	2
1.3 Relevance of Non-Thermal Processing .....	3
1.3.1 UV and Lyman-alpha Photons .....	3
1.3.2 Low-Energy Electrons .....	4
1.4 Surface FT-Infrared Spectroscopy Under Vacuum Conditions .....	6
1.5 Probing Surface:Adsorbate Interactions Using Temperature Programmed Desorption (TPD) .....	10
1.6 Thesis Overview .....	13
II ADSORPTION OF FORMAMIDE ON KAOLINITE SURFACES: A COMBINED EXPERIMENTAL AND THEORETICAL STUDY RELEVANT TO EARLY EARTH CHEMISTRY .....	15
2.1 Introduction .....	15
2.2 Experimental Details and Theoretical Methods .....	19
2.2.1 Sample Preparation and Experimental Approach .....	19

2.2.2	DFT Methods Used by Collaborators .....	23
2.3	Results .....	27
2.3.1	Infrared Spectrum of Liquid Formamide .....	27
2.3.2	Infrared Spectra of Kaolinite .....	29
2.3.3	Infrared Spectra of Formamide Adsorbed on Kaolinite .....	30
2.3.3.1	Kaolinite Vibrations .....	30
2.3.3.2	Formamide Vibrations .....	33
2.3.4	TPD of Formamide on Kaolinite .....	37
2.4	Discussion .....	38
2.4.1	Comparison of IR Spectrum of Formamide to Theoretical Spectra .....	38
2.4.2	Changes in Kaolinite Hydroxyl IR Vibrations with Temperature .....	40
2.4.3	Comparison of IR Spectra of Formamide Adsorbed on Kaolinite to Theoretical Spectra .....	42
2.4.4	Temperature Dependence of Hydroxyl and Formamide Bands and Correlation to Adsorption Geometries .....	45
2.4.5	Temperature Programmed Desorption Analysis .....	49
2.4.6	Comparison of Binding Energies to Theory .....	49
2.4.7	Discussion of Binding and Comparison of Theoretically Optimized Structures of Formamide on Kaolinite .....	50
2.5	Conclusions .....	51
III	THERMAL AND RADIATION PROCESSING OF FORMAMIDE ICES ON INTERSTELLAR SILICATE GRAIN ANALOG .....	53
3.1	Introduction .....	53
3.2	Experimental Details .....	57
3.3	Thermal Processing of Pure Formamide Ices on SiO <sub>2</sub> .....	62

3.3.1 Results .....	62
3.3.1.1 IR Spectra of HCONH <sub>2</sub> Ice From 70 K to 465 K .....	62
3.3.1.2 IR Spectra of DCONH <sub>2</sub> Ice From 70 K to 465 K .....	64
3.3.1.3 IR Spectra of HCOND <sub>2</sub> Ice From 70 K to 465 K .....	65
3.3.1.4 Comparison of IR Spectra of Formamide Ices Warmed to 165 K .....	68
3.3.1.5 Experiments to Rule Out Temperature Effects on IR Bands .....	71
3.3.1.6 Analysis of Main C=O Stretch of Formamide Upon Warm-up .....	73
3.3.1.7 TPD of HCONH <sub>2</sub> on SiO <sub>2</sub> Nanopowder .....	75
3.3.2 Discussion .....	77
3.3.2.1 Molecular Rearrangement Upon Warm-up .....	77
3.3.2.2 SiO <sub>2</sub> Changes Upon Warm-up .....	79
3.3.2.3 Temperature Programmed Desorption Analysis .....	80
3.4 Lyman- $\alpha$ Processing of Pure Formamide Ices on SiO <sub>2</sub> .....	81
3.4.1 Results .....	81
3.4.1.1 IR Spectra After Lyman- $\alpha$ Irradiation of HCONH <sub>2</sub> Ice on SiO <sub>2</sub> at 70 K .....	81
3.4.1.2 Product Peak Growth Upon Irradiation .....	83
3.4.1.3 IR Spectra of Post-Irradiation Warm-up of 70 K Ice .....	86
3.4.1.4 IR Spectral and Product Yield Comparison of Irradiated 70 K Ice vs. 165 K Annealed Ice .....	88
3.4.1.5 H <sub>2</sub> TPD of Post-Irradiation Warm-up of 70 K Ice and 165 K Annealed Ice .....	91
3.4.2 Discussion .....	93

3.4.2.1	Column Densities of Products After 72 hr Lyman- $\alpha$ Irradiation .....	93
3.4.2.2	Post-Irradiation Temperature Programmed Desorption Analysis .....	94
3.4.2.3	Product Formation From Lyman- $\alpha$ Irradiation of Pure Formamide Ices .....	95
3.4.2.3.1	SiO <sub>2</sub> Substrate Effects on Product Formation .....	95
3.4.2.3.2	OCN <sup>-</sup> Assignment and Proposed Formation Mechanisms .....	96
3.4.2.3.3	CO Formation .....	99
3.4.2.3.4	Reformation of Formamide .....	99
3.4.2.3.5	Lack of NH <sub>2</sub> , NH <sub>3</sub> , NH <sub>4</sub> <sup>+</sup> , HCN, and H <sub>2</sub> O .....	100
3.5	Lyman- $\alpha$ Processing of Water:Formamide Mixed Ices on SiO <sub>2</sub> .....	102
3.5.1	Results .....	102
3.5.1.1	IR Spectra After Lyman- $\alpha$ Irradiation of Mixed H <sub>2</sub> O:HCONH <sub>2</sub> Ices on SiO <sub>2</sub> at 70 K .....	102
3.5.2	Discussion .....	104
3.5.2.1	Column Density Comparisons Between Pure and Mixed H <sub>2</sub> O:HCONH <sub>2</sub> Ices After Lyman- $\alpha$ Irradiation .....	104
3.6	Electron Irradiation of Pure Formamide and Water:Formamide Mixed Ices on SiO <sub>2</sub> .....	106
3.6.1	Results .....	106
3.6.1.1	IR Spectral Comparison After 1 keV Electron Irradiation of Pure HCONH <sub>2</sub> and Mixed H <sub>2</sub> O:HCONH <sub>2</sub> Ices on SiO <sub>2</sub> at 70 K .....	106
3.6.2	Discussion .....	108

3.6.2.1	Column Density Comparisons Between Electron Irradiation and Lyman- $\alpha$ Irradiation of Pure and Mixed H <sub>2</sub> O:HCONH <sub>2</sub> Ices on SiO <sub>2</sub> at 70 K .....	108
3.7	Conclusions .....	113
IV	THERMAL AND RADIATION STUDIES OF PURE AND MIXED ICES RELEVANT TO TITAN'S CHEMISTRY .....	115
4.1	Introduction .....	115
4.2	Experimental Details .....	119
4.3	Results .....	122
4.3.1	TPD of H <sub>2</sub> From Electron Irradiation of Pure Acetonitrile (CH <sub>3</sub> CN) on Au .....	122
4.3.2	TPD of CH <sub>4</sub> , HCN, CH <sub>3</sub> CN From Electron Irradiation of Pure CH <sub>3</sub> CN on Au .....	124
4.3.3	TPD of m/z 2 and 4 From Electron Irradiation of Pure Acetylene (C <sub>2</sub> D <sub>2</sub> ) on Au .....	125
4.3.4	TPD From Electron Irradiation of Mixed Layered Ices (C <sub>2</sub> D <sub>2</sub> /CH <sub>3</sub> CN) on Au .....	126
4.3.5	Infrared Spectra of Irradiated Mixtures on SiO <sub>2</sub> .....	128
4.3.5.1	IR After 400 eV Electron Irradiation of C <sub>2</sub> D <sub>2</sub> /CH <sub>3</sub> CN .....	128
4.3.5.2	IR After 1 keV Electron Irradiation of C <sub>2</sub> D <sub>2</sub> /CH <sub>3</sub> CN .....	130
4.3.5.3	IR After Lyman- $\alpha$ Irradiation of C <sub>2</sub> D <sub>2</sub> /CH <sub>3</sub> CN .....	131
4.3.6	TPD of Acetylene Fragments From Mixed Ices on SiO <sub>2</sub> .....	132
4.3.7	Coverage-dependent TPD of Acetylene on SiO <sub>2</sub> .....	135
4.4	Discussion .....	136
4.4.1	Irradiation of Pure and Mixed Ices .....	136
4.4.2	Acetylene Trapping .....	140

4.5 Conclusions .....	142
V CONCLUDING REMARKS .....	144
REFERENCES .....	149

## LIST OF TABLES

	Page
2.1	Experimental infrared vibrations for formamide liquid compared to theoretical values (obtained with M05 2X/6 31G(d), M05 2X/6 31G(d,p) and M05 2X/6 31+G(d,p), scaled by 0.9364 and 0.9373) for formamide in gas phase and liquid phase .....28
2.2	Experimental infrared vibrations for kaolinite powder at sample temperatures of 300 K and 110 K .....30
2.3	Experimental infrared kaolinite vibrations for formamide adsorbed on kaolinite at 67 K, 110 K, and 300 K compared to theoretical values (obtained at 110 K using M05 2X/6 31G(d), scaled by 0.9364 and 0.9373) for formamide adsorbed on the octahedral surface of non-hydrated kaolinite (K(o)-FA) and formamide adsorbed on the tetrahedral surface of non-hydrated kaolinite (K(t)-FA) .....32
2.4	Experimental infrared formamide vibrations for formamide adsorbed on kaolinite at dosing temperatures of 67 K, 100 K, 110 K compared to theoretical values (obtained at 110 K using M05-2X/6-31G(d), scaled by 0.9364 and 0.9373) for formamide adsorbed on the octahedral surface of non-hydrated kaolinite (K(o)-FA) and formamide adsorbed on tetrahedral surface of non-hydrated kaolinite (K(t)-FA). Frequencies for the formamide-kaolinite pre-mixed slurry at 80 K and then for subsequent formamide dosed on the slurry at 80 K are also given for comparison .....36
3.1	Infrared vibrational frequencies for formamide isotopes (1100 L dosed at 70 K) after warm-up to 165 K .....70
3.2	Normalized column densities ( $N$ ) of 1388 $\text{cm}^{-1}$ formamide, $\text{OCN}^-$ , and CO bands upon ~3 hr irradiation of pure $\text{HCONH}_2$ ice compared to 0.75:1 and 2:1 $\text{H}_2\text{O}:\text{HCONH}_2$ mixed ices .....105
3.3	Comparison of Lyman- $\alpha$ and electron irradiation total energy doses on an eV/formamide molecule basis for pure $\text{HCONH}_2$ and 0.75:1 $\text{H}_2\text{O}:\text{HCONH}_2$ mixed ice .....108
3.4	Comparison of normalized column densities ( $N$ ) of 1388 $\text{cm}^{-1}$ formamide band for pure $\text{HCONH}_2$ and 0.75:1 $\text{H}_2\text{O}:\text{HCONH}_2$ mixed ice with Lyman- $\alpha$ irradiation compared to electron irradiation .....110
3.5	Comparison of normalized column densities ( $N$ ) of 2163 $\text{cm}^{-1}$ $\text{OCN}^-$ band for pure $\text{HCONH}_2$ and 0.75:1 $\text{H}_2\text{O}:\text{HCONH}_2$ mixed ice with Lyman- $\alpha$ irradiation compared to electron irradiation .....111

3.6	Comparison of normalized column densities ( $N$ ) of $2135\text{ cm}^{-1}$ CO band for pure $\text{HCONH}_2$ and 0.75:1 $\text{H}_2\text{O}:\text{HCONH}_2$ mixed ice with Lyman- $\alpha$ irradiation compared to electron irradiation .....	112
4.1	Comparison of Lyman- $\alpha$ and electron irradiation total energy doses on an eV/acetonitrile molecule basis for 1:0.75 $\text{C}_2\text{D}_2:\text{CH}_3\text{CN}$ mixed ice, based on the initial column density of CN stretch of $\text{CH}_3\text{CN}$ at $2252\text{ cm}^{-1}$ .....	139
4.2	Normalized column densities ( $N$ ) of $2252\text{ cm}^{-1}$ band of $\text{CH}_3\text{CN}$ for 1:0.75 $\text{C}_2\text{D}_2:\text{CH}_3\text{CN}$ mixed ice before and after irradiation with 400 eV electrons, 1 keV electrons, and Lyman- $\alpha$ irradiation .....	140

## LIST OF FIGURES

	Page
1.1 The expected fragmentation pathways upon bombardment of a molecule, AB, with low-energy electrons. Reprinted from previous publications [1,2] with permission from Elsevier (Copyright 2010) and American Chemical Society (Copyright 2000) .....	5
2.1 Schematic representation of the experimental ultra-high vacuum (UHV) chamber. The system is equipped with a temperature controlled sample holder connected to the helium cryostat, a quadrupole mass spectrometer (QMS), and ZnSe windows for transmission of the IR beam from the FT-IR spectrometer through the chamber, onto the sample, and out to the external HgCdTe (MCT) detector .....	20
2.2 Picture (left) and drawing (right) of the sample holder and substrate used for transmission FT-IR spectroscopy and TPD measurements of grain/mineral analogs under UHV conditions .....	21
2.3 The optimized structure of formamide adsorbed on octahedral (a, K(o)-FA) and tetrahedral surface (b, K(t)-FA) of kaolinite used to calculate infrared spectra. Figure courtesy of Andrea Michalkova Scott .....	26
2.4 Experimental transmission infrared spectrum of pure formamide liquid (a) compared to formamide calculated in the gas phase (t) and liquid phase (l, blue) at the M05-2X/6-31G(d) level. Spectra of formamide calculated using 6-31G(d,p) (tp) and 6-31+G(d,p) (tp+) larger basis sets are also shown for comparison (red and green, respectively) .....	27
2.5 Experimental transmission infrared spectra of kaolinite powder at (a) 300 K and (b) 110 K .....	29
2.6 Experimental transmission infrared spectra of kaolinite vibrations when formamide is exposed to kaolinite at (a) 300 K, (b) 110 K, (c) 67 K, and theoretical spectrum (t) of adsorbed formamide on the octahedral surface of kaolinite calculated at 110 K .....	31
2.7 Transmission infrared spectra of formamide vibrations (C=O stretch, CH scissor, and C-N stretch) when formamide is dosed onto kaolinite at temperatures between 67-140 K (all spectra recorded at 67 K after dosing) compared to the pre-mixed formamide-kaolinite slurry (b) at 80 K in which intercalation is most likely evident and subsequent formamide dosing (a) (~1100 L, dosed at 80 K) onto the pre-mixed slurry. The theoretical (t) spectrum of adsorbed formamide on the octahedral surface of kaolinite (K(o)-FA) calculated at 110 K is also shown .....	34

2.8	Transmission infrared spectra of formamide vibrations (top pane - NH stretches, bottom pane - CH stretch) when formamide is dosed onto kaolinite at temperatures between 67-140 K (all spectra recorded at 67 K after dosing) compared to the pre-mixed formamide-kaolinite slurry (b) at 80 K and subsequent formamide dosing (a) (~1100 L, dosed at 80 K) onto the pre-mixed slurry. The theoretical (t) spectrum of adsorbed formamide on the octahedral surface of kaolinite (K(o)-FA) calculated at 110 K is also shown .....	35
2.9	TPD of mass 45 (formamide) after adsorption of 13 L formamide on kaolinite powder at 110 K. TPD taken after cooling sample to 67 K .....	37
3.1	Infrared spectra during warm-up after deposition of 1100 L of HCONH <sub>2</sub> at 70 K .....	63
3.2	Infrared spectra during warm-up after deposition of 1100 L of DCONH <sub>2</sub> at 70 K .....	65
3.3	Infrared spectra during warm-up after deposition of 1100 L of HCOND <sub>2</sub> at 70 K .....	67
3.4	Comparison of infrared spectra at 165 K during warm-up after deposition at 70 K of 1100 L of (A) HCOND <sub>2</sub> , (B) DCONH <sub>2</sub> , (C) HCONH <sub>2</sub> .....	69
3.5	Comparison of infrared spectra of 1100 L HCONH <sub>2</sub> at 70 K after dosing (bottom), upon warm-up to 165 K (middle), and upon cooling back to 70 K (top) .....	72
3.6	C=O stretch (A) infrared maximum peak position and (B) absolute intensity as a function of increasing temperature for three formamide isotopes.....	74
3.7	TPD of mass 45 (HCONH <sub>2</sub> ) after adsorption of formamide on SiO <sub>2</sub> nanopowder at 70 K showing coverage dependence from 0 to 1100 L .....	76
3.8	Infrared difference spectra of 1100 L HCONH <sub>2</sub> ice as a function of increasing Lyman- $\alpha$ irradiation time (hr) at 70 K .....	82
3.9	Infrared spectra of OCN <sup>-</sup> /CO growth as a function of increasing Lyman- $\alpha$ irradiation time (hr) for 1100 L HCONH <sub>2</sub> ice deposited and irradiated at 70 K .....	84
3.10	OCN <sup>-</sup> /CO combined product peak areas for Lyman- $\alpha$ irradiation of 1100 L HCONH <sub>2</sub> ice at 70 K as a function of irradiation time. Inset is close-up of the initial 5.5 hr of irradiation .....	85

3.11	Infrared spectra of post-irradiation (5.5 hr) warm-up from 70 K to 395 K of 1100 L HCONH <sub>2</sub> ice. (A) displays the sharpening of features similar to non-irradiated samples and (B) displays a close-up of the OCN <sup>-</sup> , CO, and CO <sub>2</sub> region .....	87
3.12	OCN <sup>-</sup> /CO combined peak growth comparison during Lyman- $\alpha$ irradiation of 1100 L HCONH <sub>2</sub> ice at (A) 70 K and (B) after annealing to 165 K .....	88
3.13	Combined OCN <sup>-</sup> /CO product peak areas as a function of Lyman- $\alpha$ irradiation time for 1100 L HCONH <sub>2</sub> ices irradiated at 70 K (black) compared to ices annealed to 165 K then cooled to 70 K prior to irradiation (blue) .....	90
3.14	TPD spectra of mass 2 (H <sub>2</sub> ) after adsorption of 1100 L HCONH <sub>2</sub> on SiO <sub>2</sub> nanopowder at 70 K and after annealing to 165 K for both no irradiation (black) and after 72 hours of Lyman- $\alpha$ irradiation (blue) .....	92
3.15	Infrared spectra of OCN <sup>-</sup> and CO production upon Lyman- $\alpha$ irradiation of a 2:1 mixture of H <sub>2</sub> O:HCONH <sub>2</sub> at 70 K .....	103
3.16	Infrared spectral comparison of OCN <sup>-</sup> and CO bands for pure HCONH <sub>2</sub> (FA) after 71.5 hr Lyman- $\alpha$ irradiation (red), pure HCONH <sub>2</sub> after 1 hr of 1 keV electron irradiation (black), and 0.75:1 H <sub>2</sub> O:HCONH <sub>2</sub> after 1 hr of 1 keV electron irradiation (blue). Inset is close-up of the CO band .....	107
4.1	Deposition of energy affecting Titan's chemistry (EUV, electrons, ions, etc.) as a function of altitude. Adapted from Krasnopolsky [3] with permission (Copyright 2009) from Elsevier .....	116
4.2	Post-irradiation TPD of m/z 2 (H <sub>2</sub> ) for layered CH <sub>3</sub> CN ice (1 L x 4) after deposition at 40 K and then 100 eV electron irradiation for 10 minutes .....	123
4.3	Post-irradiation TPD of m/z 16 (black), 27 (red), and 41 (blue) after deposition of 2 L CH <sub>3</sub> CN at 40 K and then 400 eV electron irradiation for 17 minutes .....	124
4.4	TPD of m/z 2 (A) and m/z 4 (B) after deposition of 110 L total C <sub>2</sub> D <sub>2</sub> at 40 K in two layers. TPD after no irradiation shown in black. TPD after 200 eV irradiation of the layers for a total of 1.5 hr shown in red (m/z 2) and blue (m/z 4) .....	125
4.5	Schematic representation of the ice layers for the mixed ices as deposited and irradiated with electrons between each layer. (A) displays the 70 eV experiment and (B) displays the 200 eV experiment .....	126
4.6	Post-irradiation 3D TPD for (A) no irradiation, (B) 70 eV irradiation, and (C) 200 eV irradiation after deposition of 120 L C <sub>2</sub> D <sub>2</sub> and 120 L CH <sub>3</sub> CN (layered) at 40 K .....	127

4.7	Single TPD comparison of m/z 4 for D <sub>2</sub> for no irradiation (black), 70 eV electrons (blue), and 200 eV electrons (red) after deposition of 120 L C <sub>2</sub> D <sub>2</sub> and 120 L CH <sub>3</sub> CN (layered) at 40 K .....	128
4.8	Infrared spectra of pre-irradiated 1:0.75 mixture (C <sub>2</sub> D <sub>2</sub> :CH <sub>3</sub> CN) (black) compared to difference spectra (top four) taken as a function of 400 eV radiation time .....	129
4.9	IR spectra of pre-irradiated 1:0.75 mixture (C <sub>2</sub> D <sub>2</sub> :CH <sub>3</sub> CN) (black) compared to difference spectra (top three) taken as a function of 1 keV radiation time .....	130
4.10	Infrared difference spectra of pre-irradiated 1:0.75 mixture (C <sub>2</sub> D <sub>2</sub> :CH <sub>3</sub> CN) (black) compared to difference spectra (top five) taken as a function of 10.2 eV Lyman- $\alpha$ radiation time .....	132
4.11	TPD for m/z 24 (CC, triple-bonded) after dosing 1100 L pure C <sub>2</sub> D <sub>2</sub> (black) compared to 1:0.75 (1100 L C <sub>2</sub> D <sub>2</sub> : 825 L CH <sub>3</sub> CN) mixed ice (red) .....	133
4.12	TPD for m/z 24 (CC, triple-bonded) after dosing 1100 L pure C <sub>2</sub> D <sub>2</sub> (black) compared to 1:0.75 (1100 L C <sub>2</sub> D <sub>2</sub> : 825 L CO <sub>2</sub> ) mixed ice (blue) .....	134
4.13	TPD for m/z 24 (CC, triple-bonded) after dosing 1100 L pure C <sub>2</sub> D <sub>2</sub> (black) compared to 1:0.75 (1100 L C <sub>2</sub> D <sub>2</sub> : 825 L H <sub>2</sub> O) mixed ice (green) .....	134
4.14	Coverage-dependent TPD of 400 to 1100 L C <sub>2</sub> D <sub>2</sub> (m/z 24 for CC triple-bonded) on SiO <sub>2</sub> nanopowder, showing two peaks representing multilayer ( $\alpha$ 1) and monolayer ( $\alpha$ 2) desorption .....	135

## SUMMARY

A custom ultra-high vacuum (UHV) chamber has been built that is coupled with Fourier Transform-Infrared spectroscopy (FT-IR) and Temperature Programmed Desorption (TPD) using Quadrupole Mass Spectrometry (QMS). These techniques have been used to investigate several organic:surface systems. Novel studies include: 1) formamide's ( $\text{HCONH}_2$ ) interaction with kaolinite ( $\text{Al}_6\text{Si}_6\text{O}_{36}\text{H}_{30}$ ), a clay mineral relevant to early Earth chemistry, 2) Lyman- $\alpha$  photon and low-energy electron processing of pure formamide and  $\text{HCONH}_2\text{:H}_2\text{O}$  mixed ices on an interstellar grain analog ( $\text{SiO}_2$  nanopowder), and 3) low-energy electron (70-1000 eV) and Lyman- $\alpha$  photon processing of acetonitrile ( $\text{CH}_3\text{CN}$ ) and acetylene ( $\text{C}_2\text{H}_2$ ) pure and mixed ices relevant to Titan's chemistry. The unifying theme of this thesis is to investigate the adsorption and radiation and thermal processing of prebiotically-relevant ices and surfaces.

First, in collaboration with a theory group, formamide's interaction with kaolinite has been studied experimentally and theoretically. Formamide is a simple  $\text{HNCO}$  non-volatile molecule believed to exist in liquid pools on early Earth. Kaolinite minerals, also believed to be present on early Earth, can catalyze the formation of nucleic acid bases and amino acids from formamide, but the mechanism of the interaction is not well understood. Energies of desorption for the formamide:kaolinite system have been experimentally determined (using TPD) and compare well with calculated energies, indicating physisorption. Upon cooling, it has been shown previously that some inter-nuclear distances between the  $\text{OH}\dots\text{O}$ 's of kaolinite change, and the preferential availability of adsorption sites could change as well. Indeed, formamide vibrational bands at 67-90 K indicate hydrogen bonding between kaolinite's octahedral face and

formamide's C=O group, which agrees well with theory. However, at 100-110 K the interaction restructures and formamide-formamide dimer interactions become dominant. These results suggest that the temperature dependence of the kaolinite hydroxyl and formamide vibrational frequencies are sensitive probes of formamide interactions with the exposed and inter-layer surfaces of kaolinite.

Second, formamide has also been found in cold interstellar regions. Understanding its reactions can provide key insights into biomolecule formation where cosmic rays and UV photons process interstellar icy grains. Three distinct formamide ice phases (on SiO<sub>2</sub>) have been observed upon warm-up from 70 to 460 K. Slow photochemical production of OCN<sup>-</sup>/CO and the lack of other products indicates that formamide's peptide bond is generally stable at low temperatures, lending credence to its detection in energetically processed interstellar regions. Product yields heavily depend upon the ice structure, and photolysis in the condensed phase is considerably different than in the gas-phase with different products and product branching ratios. In the condensed phase, the yields of OCN<sup>-</sup>, CO, and H<sub>2</sub> are not negligible. Condensed phase interactions and the underlying SiO<sub>2</sub> substrate may provide channels for photoionization below 10.2 eV, as well as increase ion-electron recombination and radical recombination rates. Some products are also likely produced on the surface, which are not detected. Introduction of water to the formamide ice increases the OCN<sup>-</sup> and CO products, with possible implications for OCN<sup>-</sup> observation in water-dominated icy grains that contain formamide. However, electron irradiation of formamide ices appears to induce different pathways that do not involve decarboxylation. The latter is likely due to an increased contribution of dissociative electron attachment resonances.

Third, exploring the reactions of hydrocarbon ices is crucial to determining Titan's role as a prebiotic chemical system in the outer solar system. This investigation of the reactions of  $C_2D_2/CH_3CN$  ices contributes to understanding the possible consumption, trapping, and degradation of these species on the surface of Titan. Acetylene trapping within 94 K  $CH_3CN$  and  $H_2O$  ice has implications for its sublimation behavior and suggests that it could exist within organics on Titan's surface. Electron irradiation is shown to dissociate the parent ices to produce hydrogen/deuterium that desorb at low temperatures. In addition, it was determined that cyanoacetylene ( $HC_3N$ ) is not a major product of  $C_2D_2/CH_3CN$  mixed ice radiation processing.

In summary, this thesis has contributed to the elucidation of radiation and thermal pathways and adsorption of some prebiotic molecules ( $HCONH_2$ ,  $CH_3CN$ ,  $C_2H_2$ , and  $H_2O$ ) on clay surfaces relevant to early Earth and on silicate particle surrogates for primitive interstellar grain surfaces. The research described herein serves to complement other laboratory and observational-based studies in the prebiotic, planetary, radiation chemistry, and astrochemistry fields.

# CHAPTER I

## INTRODUCTION

### 1.1 Importance of Studying Organic-Mineral Interfaces

#### Relevant to Prebiotic Chemistry

Prebiotic molecules, which are involved in reactions that may have led to the molecular origin of life, include amino acids, nucleobases, sugar-like compounds, peptides [4], as well as activated phosphates [5,6]. These could have arisen from reactions of even simpler molecules such as H<sub>2</sub>O, HCN, CH<sub>4</sub>, N<sub>2</sub>, NH<sub>3</sub>, or HCONH<sub>2</sub> (formamide) [7,8]. These molecules are thought to have been in the atmosphere and/or on the surface of prebiotic Earth and have also been found in interstellar icy grains [9] and on planetary bodies [10]. One possible link between prebiotic Earth and interstellar/planetary prebiotic chemistry are meteorites, where peptides, amino acids, and nucleobases have been discovered [6]. Thus, understanding the chemistry of simple molecules and ices is important to both astrophysical and origin-of-life communities.

Minerals were ubiquitous on early Earth [11], and these surfaces could help solve the dilution problem of prebiotic chemistry. Besides serving as surfaces where pools of liquids could concentrate, mineral surfaces (including clay surfaces) could also act catalytically to accelerate reactions [12]. In addition, they could provide sources of chemical energy and help diversify reaction pathways. For example, several minerals have enhanced formamide's reactivity leading to nucleobases [13]. Saladino and Di Mauro et al. have studied formamide's reactivity with many surfaces including TiO<sub>2</sub>

[14], montmorillonites [15], cosmic dust analogues [16], and zirconia [17]. In addition, observational IR spectra of interstellar regions have identified silicates as a main component of icy grains [18,19]. There are many other components in cosmic and planetary dust, such as Fe-rich olivine grains [20], that could also have catalytic effects on ice chemistry. Thus, ice-grain chemistry [21] could affect pathways leading to larger prebiotic molecules.

## **1.2 Relevance of Thermal Processing**

Day-night cycling on prebiotic Earth likely produced conditions in which non-volatile molecules in pools interacting with mineral surfaces [11] could thermally be processed. This thermal processing likely resulted in larger biomolecules. For example, it has been shown that simple heating of formamide to 130-160 °C can induce reactions leading to nucleobases [22]. In addition, it has been reported that molecules such as formaldehyde at cryogenic temperatures can be thermally promoted to form more complex organics [23]. Similarly, warming of icy grains in interstellar regions, due to energy released from star formation, results in higher mobility of radicals and molecules within the ices and induces an increase yield of biomolecules that can sublime or be left behind as residues. Some volatile products may be promoted to the gas phase to further contribute to reactions of the parent species [24]. Finally, on organic-rich planetary bodies, such as Saturn's moon Titan, fluctuations in the temperature due to meteorology can affect aerosol processing, also contributing to rich prebiotic chemistry [25-27].

### 1.3 Relevance of Non-Thermal Processing

Icy surfaces are prevalent in space, including satellites and planets, dust grains of rings, interstellar sources, and comets. These ices are exposed to bombardment by stellar winds, galactic cosmic rays, and in some locations, VUV and UV irradiation. Such processing can lead to fragmentation or sputtering of molecules residing within the ices. Formation of new molecules can also occur from recombination of radicals or ions within the ices. The radiation processes involved in degrading starting species or forming products can be quite different for low-energy electron vs. photon irradiation [28]. Below is a brief overview of the radiation types used herein.

#### 1.3.1 UV and Lyman-alpha Photons

The UV photon fluxes in several regions of space have been estimated. For example, the flux of 10 eV photons in Oort cloud and KBO (Kuiper Belt Object) regions has been estimated at  $\sim 9.6 \times 10^8 \text{ eV cm}^{-2} \text{ s}^{-1}$ , with an energy dose of  $10^8 \text{ eV/molecule}$  [28]. In Jovian and Saturnian satellites (e.g. Europa, Titan, etc.), the 10 eV photon flux could be as high as  $4 \times 10^{13} \text{ eV cm}^{-2} \text{ s}^{-1}$ , with an estimated energy dose of  $10^{13} \text{ eV/molecule}$  for the top  $0.015 \mu\text{m}$  layer of ice [28]. In interstellar cold dense molecular clouds, Oort cloud, and KBO regions, the residence time of ices is  $\sim 10^6\text{-}10^9$  years, and residence times can be as much as  $<1 \times 10^8$  years in Jovian satellites [28]. Thus, UV and VUV photons will interact with icy grains that are present in these regions (e.g., via photoionization or photodissociation). The resulting photochemistry has been the focus of many studies [29-32] including ices containing  $\text{H}_2\text{O}$ ,  $\text{CO}$ ,  $\text{CO}_2$ ,  $\text{NH}_3$ ,  $\text{HCN}$ , among others. However, only a few studies to-date have included relevant grain-ice interfacial investigations [21,33,34].

Lyman-alpha ( $\alpha$ ) radiation or photons are produced from a particular UV emission line (the Lyman- $\alpha$  line) of hydrogen, where the energy level of hydrogen's electron transitions from the  $n=2$  to  $n=1$  orbital. Its wavelength is  $1215 \text{ \AA}$  or  $121.5 \text{ nm}$

(corresponding to 10.2 eV). In interstellar space, the Lyman- $\alpha$  line is produced by star-forming regions and distant galaxies which are often termed Lyman- $\alpha$  emitters. Upon photolysis with Lyman- $\alpha$  radiation, a photon is absorbed with each ionization or excitation event [28].

### 1.3.2 Low-Energy Electrons

The cosmic ray flux in interstellar cold dense molecular clouds has been estimated at  $\sim 1 \times 10^6 \text{ eV cm}^{-2} \text{ s}^{-1}$ , with an estimated energy dose of 0.3 to 3 eV/molecule [28]. This can be much higher around satellites in the outer solar system and in the Oort Cloud and KBO regions ( $\sim 150 \text{ eV/molecule}$ ) [28]. Secondary low-energy electrons play a pivotal role in the reactions induced by such high energy radiation [2]. The cosmic rays that are prevalent throughout space, when deposited in ices, produce a track of secondary electrons that induce numerous ionizations and excitations [28]. These non-thermal low-energy secondary electrons cause most of the chemical changes within the ices due to inelastic scattering events [2].

Upon low-energy electron bombardment of the ice, pathways for fragmentation can occur that lead to reactive species. The fragments that are created can react with other species, desorb, or react with the surface. The pathways for electron-induced fragmentation have been detailed elsewhere [2,35], however, see Figure 1.1 for a summary.

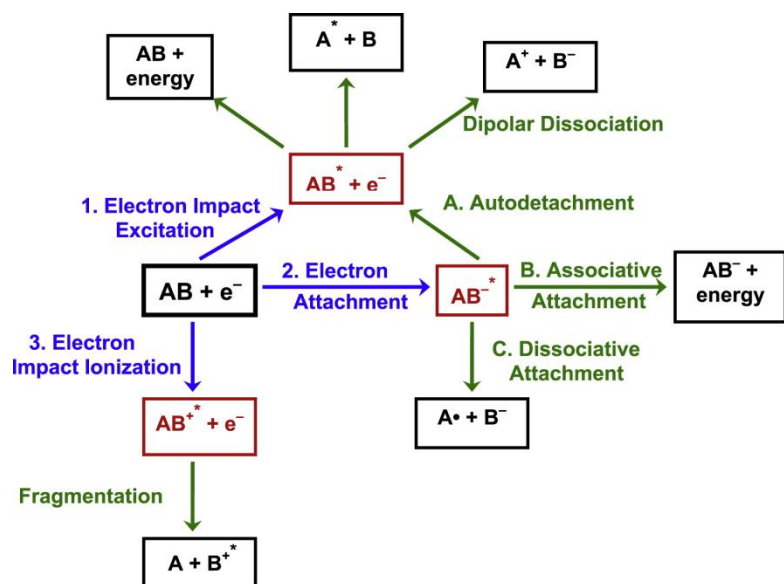


**Figure 1.1:** The expected fragmentation pathways upon bombardment of a molecule, AB, with low-energy electrons. Reprinted from previous publications [1,2] with permission from Elsevier (Copyright 2010) and American Chemical Society (Copyright 2000).

Briefly, there are direct decay channels and transient negative ion (TNI) channels. Of the direct decay channels, some examples include electron impact ionization ( $AB + e^- \rightarrow AB^{+\bullet} + e^-$ ) and electron impact excitation ( $AB + e^- \rightarrow AB^* + e^-$ ). From electron impact ionization, the  $AB^{+\bullet}$  can subsequently produce reactive radical species by fragmenting or undergoing ion-molecule reactions. From electron excitation, the  $AB^*$  may also dissociate into neutral radicals [2]. Thus, direct decay channels of low-energy electron collisions with molecules can induce radical formation in ices that can play a role in very complex chemistry.

Alternatively, during the formation of a TNI, the electron usually interacts with the lowest unoccupied molecular orbital (LUMO) of the molecule, AB. A negative ion is produced from the collision of a captured electron with the molecule ( $AB + e^- \rightarrow AB^{+\bullet}$  or  $AB^-$ ). This occurs via a resonant process and so TNIs are also called negative ion resonances [2]. The relative electronic energies of the TNI can either be due to single-particle shape resonances (with 0-5 eV energy) or core-excited shape

resonances (with 5-15 eV energy) [2]. The negative ion produced can then autodetach from the electron and can become vibrationally excited or it can have a long lifetime in which dissociation is induced. The latter mechanism is called dissociative electron attachment (DEA), and bond scission results in a stable anion along with a neutral atom or molecular radical ( $AB^{*-} \rightarrow A\bullet + B^-$ ). DEA is an interesting decay channel in the context of ice radiation chemistry because stable negative ions, such as  $OCN^-$  that have been identified in interstellar ice spectra [36], could be the result of such a process.

#### **1.4 Surface FT-Infrared Spectroscopy Under Vacuum Conditions**

Infrared spectroscopy is a powerful characterization technique that measures the adsorption of sample molecules in the infrared region of the electromagnetic spectrum. The intensity of the light transmitted through the sample is measured for the entire frequency range [37]. Adsorption requires a change in dipole moment or polarity of the species [38]. Thus, molecules such as  $N_2$  or  $O_2$  cannot exhibit a dipole moment and will not show peaks in an IR spectrum because there is not absorption in the mid-infrared region [38]. Peaks in the IR spectrum are a result of excitations of the molecule leading to vibrations (or rotations) of the bonds in the molecule, and there are several types of vibrational modes (e.g., stretching, bending, torsion, wagging, etc.) that can provide functional group information about the sample. These modes or states are best described by the Morse potential and simple harmonic potential, which describes transitions of the molecule from the ground state ( $\nu = 0$ ) to higher energy levels ( $\nu = 1, 2, 3, 4$ , etc.) [37]. A fundamental transition or mode occurs from the ground state ( $\nu = 0$ ) to the first energy level ( $\nu = 1$ ) [37]. The number of normal or fundamental vibrational modes a molecule will exhibit is defined by  $3n-6$ , where  $n$  equals the number of atoms in the molecule. This comes from the three degrees of freedom a molecule is said to have, based on three

coordinate motion [37]. If a molecule is linear, it will have  $3n-5$  vibrational modes visible in the IR spectrum because rotation about the molecular axis does not exist for linear molecules [37].

Fourier Transform-Infrared (FT-IR) spectrometers are the standard today, and they possess many advantages. Older dispersive instruments required a grating monochromator, which could only record one frequency at a time. FT-IR spectrometers use an interferometer instead, which allows the IR radiation source to be split by a beam splitter into two paths. One goes to a moving mirror while the other goes to a fixed position mirror. Once the beams are reflected, they recombine and produce an interference pattern containing all wavelengths. Then all the frequencies of infrared light are seen by the sample simultaneously and at all times, and as the mirror in the interferometer is continuously scanned, the interference pattern changes. This produces a time domain spectrum (interferogram) which can be converted to the frequency domain with FT. This is called Jacquinot's advantage, resulting in greater throughput or signal-to-noise, due to all the wavelengths being seen at all times. Another advantage is Fellgett's advantage (i.e. a multiplex advantage) which means that the spectral resolution is comparable or better than dispersive spectrometers [38].

There are several successful methods of FT-IR spectroscopy to look at solids and surface species [39]. These include Attenuated Total Reflection (ATR) [40], Diffuse Reflectance Infrared Fourier Transform Spectroscopy (DRIFTS) [41], and Reflection-Absorption Infrared Spectroscopy (RAIRS, also termed IRAS or RAS) [42]. However, those that are very useful with powders, grains, or nanoparticles (ATR and DRIFTS, which provide multiple reflections off the sample) present some challenges

when attempting to couple with ultra-high vacuum (UHV) conditions. In addition, heating or cooling ATR or DRIFTS cells, especially under vacuum, can present additional technical difficulties. The best and easiest technique currently used to study adsorbate:surface interactions under vacuum conditions is RAIRS. This is because the IR beam is simply directed out of the IR spectrometer, reflected off the substrate in the chamber, and collected in an external detector (HgCdTe or MCT covering the mid-IR region). However, RAIRS is usually not successful with powders or grains of any kind because it requires reflectance off the sample. For one, vertically positioned sample holders would have difficulty holding the powder. Indeed, most RAIRS studies have involved metals [39,42] or metal oxide [43] thin films grown on a flat reflective surface that can be held in any position within the chamber. The metal is also necessary for the advantage of doubling the *p*-polarized light at grazing incidence angles in RAIRS. RAIRS is also the technique of choice for most laboratory astrochemists that study ices on inert (usually gold or some other reflective material) substrates, because reflection off the ice is straight forward under vacuum conditions [21,28,29,31]. In some ice experiments, amorphous solid water (ASW) is first adsorbed to use as the substrate [21]. However, because a goal of this thesis has been the observation of adsorbate:surface interactions that involve realistic grain or mineral analogs, the before-mentioned methods all have their disadvantages for the systems studied herein.

An alternative IR method [44] is simple transmission through an IR transparent material (such as SiO<sub>2</sub>, kaolinite, TiO<sub>2</sub>, ZrO<sub>2</sub>, etc.) that also happens to be a relevant grain or prebiotic mineral simulant. The IR transparent material or powder is simply pressed or coated onto a wire mesh that is then vertically affixed in the vacuum chamber. This

transmission IR method has been successfully used by Yates et al. [33,45] in astrochemically-relevant studies, and thus was adopted for the investigations described within this thesis. One limitation to this method lies with non-transparent powders (e.g., graphite, carbon, etc.) unless mixed with an IR transparent material such as KBr. However, using transparent powders, the technique is quite powerful and can provide infrared vibrational spectra of the interaction between adsorbates and mineral or grain analog surfaces. Changes in the molecule as a function of sample temperature (apart from temperature effects on the IR vibrations [37]) or post-irradiation product formation can be observed.

A main reason for the use of IR spectroscopy is that features in the spectra after irradiation can lead to determination of ice column densities of parent species and their products, which can be compared to observed total dust columns through a molecular cloud towards a star as obtained by observational data (e.g., near infrared photometry from the *Two Micron All Sky Survey* [46]). In addition, laboratory ice spectra of molecules on grain analogs are valuable to understanding and assigning features in the vast observational infrared databases of the *Infrared Space Observatory* and the *Spitzer Space Telescope*, which have sampled regions including Young Stellar Objects (YSO) that include interstellar icy grains [47-49]. Finally, as the *James Webb Space Telescope* is expected to launch in 2018, it will begin to explore the distribution of organic molecules and water in star-forming regions and in our own solar system. The main instruments include a mid-IR instrument, a near-IR imager/spectrograph, a near-IR camera, and a near-IR multi-object spectrograph [50]. From this new mission, many new and unassigned IR spectra could soon overwhelm the astrophysical community. For example,

since formamide is one organic molecule found [9] in many of the regions to be explored by the *James Webb Space Telescope*, the IR spectra will likely observe formamide's chemistry. Thus, some of the studies reported here (Chapter 3) may become valuable laboratory data to compare with future observational spectra.

### **1.5 Probing Surface: Adsorbate Interactions Using Temperature Programmed Desorption (TPD)**

The rate of gas evolution or desorption from a surface can change as a surface is heated under vacuum, and at a certain temperature there is a rate maximum (increased gas density) that can provide information about the amount of adsorbed molecules, their chemical nature, and the kinetics of the gas desorption [51]. This method is called Temperature Programmed Desorption (TPD), also known as Thermal Desorption Spectroscopy (TDS). It is a surface science technique that observes desorption of species from a substrate of interest in vacuum by monitoring the number density of a mass-resolved desorbate signal as a function of time, temperature, and heating rate [51,52]. Typically, the temperature is linearly increased while the specific  $m/z$  signal is monitored by a mass spectrometer. The time can be correlated with the increase in temperature, if a constant ramp rate is used. Typical ramp rates employed are 0.01 to 50 K/s [52].

A 3D TPD can also be obtained by slowing the ramp rate and monitoring a range of  $m/z$  signals as temperature is increased. This has the advantage of recording an entire mass spectrum TPD in the same experiment (see Figure 4.6 for example), but since a very slow ramp rate (0.01 to 0.5 K/s) is required to catch an entire mass spectrum for each temperature, the gas could be pumped out of the chamber faster than the QMS can detect ions. Thus, typically faster ramp rates (0.5 to 50 K/s) are employed and only a few masses are monitored at once so that the observed rate of desorption is greater than the

rate of pumping [51]. Monitoring multiple masses simultaneously in an experiment is sometimes referred to as Temperature Programmed Reaction Spectroscopy (TPRS).

Typically, quadrupole mass spectrometers (QMS) are used for TPD since they have the ability to monitor specific masses with time because the mass analyzer can be set to only allow specific ions to pass through during a given experiment [38]. Briefly, a quadrupole mass analyzer consists of four parallel metal rods that have alternating dc and radiofrequency (RF) voltages applied to them. Two opposing rods are positively charged while the other two opposing rods are negatively charged. The trajectory of the ions down the flight path is determined by the applied voltages, and only those ion trajectories that are resonant (have a specific  $m/z$  ratio) with the RF field along the  $z$  axis will make it to the detector [38]. All other ions with non-resonant paths are filtered out. The advantages of using a quadrupole analyzer include fast scanning ability (because of the rapidly varying voltages), high transmission rate, as well as modern compact designs [38]. The aperture of the detector is usually positioned very close to the sample during TPD measurements to limit detection of gas evolving from other surfaces besides the sample in the chamber during heating [52]. A cone is also sometimes attached to the end of the electron impact ionizer to prevent any electrons from escaping the QMS analyzer.

TPD analysis of the desorption can provide kinetic or thermodynamic information about the adsorption binding sites on the substrate [53-55]. The rate of desorption is most commonly described by the Polanyi-Wigner equation [51]

$$-\frac{dN}{dt} = \nu_0^{(n)} N_0^n e^{-\frac{E_{act}}{kT}}$$

where  $-dN/dt$  is the rate of desorption,  $\nu_0^{(n)}$  is the pre-exponential or frequency factor (typically  $10^{13} \text{ s}^{-1}$ ),  $N_0$  is the number of initial molecules on the surface,  $n$  is the order of desorption,  $E_{act}$  is the desorption activation energy (or binding energy),  $k$  is the Boltzmann constant, and  $T$  is the temperature of the surface [52]. The desorption order,  $n$ ,

can be determined by plotting multiple TPD curves taken at different coverages and observing the peak shapes. If there is zero-order desorption ( $n = 0$ ), all coverages will have a common leading edge in the TPD and there will be a rapid drop in desorption rate when all molecules desorb. Thus, zeroth-order desorption does not depend upon adsorbate coverage and is spontaneous. First-order ( $n = 1$ ) desorption shows a maximum desorption temperature that is constant, regardless of increasing coverage. An example of this desorption is shown in Figure 3.7 illustrating the TPD of formamide on  $\text{SiO}_2$  as a function of coverage. The maximum desorption temperature ( $T_m$ ) does not vary with temperature, and desorption depends upon only one single species. Second-order ( $n = 2$ ) desorption shows a  $T_m$  in the TPD that moves to lower temperatures with increasing coverage. Second-order desorption involves recombination of species followed by desorption and depends upon the coverage ( $\theta$ ) squared [52]. The adsorbate-substrate systems described herein mostly involve first-order desorption where  $T_m$  is constant upon increasing coverage. The Redhead analysis method [54], a modified version of the Polanyi-Wigner equation, is used to directly determine the energy of activation for adsorption from the  $T_m$  as is described in Chapters 2 and 3.

TPD can also yield information about the nature of adsorption, i.e., whether there is physisorption or chemisorption with the substrate. Physisorption can be described as a weak interaction with the surface, such as hydrogen bonding or *van der Waals* interactions [51]. Chemisorption, on the other hand, is a chemical bond (covalent or ionic) with the surface [51] that often causes its activation energy of desorption to be higher, and thus the  $T_m$  is usually higher. In addition, by analyzing the TPD peak areas, an estimate of the relative surface coverage of the adsorbate's binding states to the surface can be determined [52]. Because of the way that adsorbates dissociate from the

surface upon heating, low-temperature peaks are often multilayer peaks while high-temperature peaks may represent the monolayer adsorption. Alternatively, they could represent multiple binding sites on the surface.

TPD is thus a powerful method for determining the binding characteristics of a surface:adsorbate interaction. This technique, coupled with FT-IR spectroscopy, can also provide kinetic information about ice-grain or organic-mineral interactions [21]. In addition, TPD can assist with understanding sublimation of ices from grains in star forming regions [21]. Post-irradiation TPD can be useful for observing the production of relatively small molecular species [52], and for observing changes in the parent species adsorbed on the surface.

## 1.6 Thesis Overview

Chapter 2 describes a novel investigation of the interaction of formamide ( $\text{HCONH}_2$ ) with kaolinite. A custom ultra-high vacuum (UHV) chamber was built for this and other investigations described in this thesis. The interaction was studied using *in-situ* transmission FT-IR Spectroscopy and TPD under UHV conditions. Experimental infrared results are compared with calculated infrared frequencies obtained by our collaborators. A full discussion of temperature-dependent hydrogen bonding, formamide diffusion, and competing formamide-formamide interactions is presented. TPD analysis is compared with the calculated values of adsorption energy, and the optimal kaolinite face for adsorption is reported. This research [56], along with a companion theory paper [57], has been published as back-to-back papers.

Chapter 3 presents the first thermal and radiation study of formamide and  $\text{HCONH}_2:\text{H}_2\text{O}$  mixed ices on a relevant icy grain analog ( $\text{SiO}_2$ ) substrate. This chapter includes a detailed discussion of the pure formamide ice phases identified with FT-IR

upon warm-up, as well as the TPD binding energies of  $\text{HCONH}_2$  on  $\text{SiO}_2$ . Much of the chapter is dedicated to Lyman- $\alpha$  processing of pure  $\text{HCONH}_2$  ice and includes a full discussion of the observed photochemical products, proposed formation mechanisms, and the lack of other expected products. In addition, results of Lyman- $\alpha$  processing of mixed  $\text{HCONH}_2:\text{H}_2\text{O}$  ices are provided. Low-energy electron irradiation of pure  $\text{HCONH}_2$  and  $\text{HCONH}_2:\text{H}_2\text{O}$  mixed ices has also been reported for the first time. Product column densities from all reactions are presented and discussed. This research will soon be published as two papers, one on the thermal ice phase changes [58] and one on radiation processing [59].

Chapter 4 reports radiation and thermal processing of acetonitrile ( $\text{CH}_3\text{CN}$ ) and  $\text{D}_2$ -acetylene ( $\text{C}_2\text{D}_2$ ) pure and mixed ices, to simulate reactions that may occur on Saturn's moon, Titan. Both of these organic species have been detected in Titan's atmosphere. Ices were irradiated with both low-energy electrons (70-1000 eV) and Lyman- $\alpha$  photons, and subsequent reaction products were studied using post-irradiation TPD and FT-IR spectroscopy. TPD studies without prior irradiation are also presented and discussed with possible implications for acetylene sublimation behavior when mixed with organics on Titan's surface.

## CHAPTER II

# ADSORPTION OF FORMAMIDE ON KAOLINITE SURFACES: A COMBINED EXPERIMENTAL AND THEORETICAL STUDY RELEVANT TO EARLY EARTH CHEMISTRY<sup>1</sup>

### 2.1 Introduction

Formamide (HCONH<sub>2</sub>) chemistry has been suggested as a plausible prebiotic pathway [60] leading to higher order biomolecules on early Earth due to formamide's simple structure and unique chemical properties. Formamide is a simple HNC=O molecule which has the amide functional group that can provide the peptide linkage. Formamide is reactive at both the carbonyl and amino sites and is also a likely precursor for nucleobases and nucleic acids [22,61]. It also has many unique qualities such as likely prebiotic availability, low volatility compared to other solvents such as water, and stability at moderate temperatures [22]. Formamide's importance is further solidified by its tentative identification in interstellar ices and other outer solar system environments [62], which may provide prebiotic environments for nucleobase and amino acid formation [24]. Saladino et al. have discussed formamide's role in the synthesis of nucleobases and other informational polymers [13,60,63,64]. Recently, Barks et al. [22] have shown that reactions of neat and aqueous formamide solutions under UV irradiation and heat can produce hypoxanthine and the DNA nucleobases guanine and adenine.

---

<sup>1</sup> Reprinted with permission from [56]. Copyright (2012) American Chemical Society.

In the presence of many inorganic oxides, including kaolin (or kaolinite), formamide reactions show an improved yield of nucleobases such as purine and adenine [13]. Kaolinite ( $\text{Al}_2\text{Si}_2\text{O}_5(\text{OH})_4$ ), a clay mineral believed to be on prebiotic Earth [13], is a 1:1 layered mineral consisting of an alumina octahedral sheet and a silica tetrahedral sheet. The sheets share a common plane of oxygen atoms and are hydrogen bonded together [65]. It has extensive potential application as a catalyst and adsorbent. Kaolinite is often classified as non-expanding, and intercalation of organic molecules into the inter-layer kaolinite space is limited [66]. In addition, energy must be provided to overcome the hydrogen bonding between the layers of kaolinite [67]. Thermal contraction in the [001] direction is due to a decrease in inter-layer separation [68], and intercalation of molecules can occur preferentially as a function of temperature. Strongly polar molecules have been shown to adsorb or intercalate between the sheets of kaolinite [69-74]. An example of a molecule that can intercalate into kaolinite is formamide due to its strong polarity and short *van der Waals* molecular diameter [75]. Thus, formamide is extensively used as a precursor for preparation of other kaolinite-organic intercalation compounds [73].

The IR bands representing the kaolinite hydroxyls have been experimentally observed at  $3693\text{ cm}^{-1}$ ,  $3685\text{ cm}^{-1}$ ,  $3670\text{ cm}^{-1}$ ,  $3652\text{-}3656\text{ cm}^{-1}$  [76], and  $3620\text{-}3623\text{ cm}^{-1}$  [76,77]. The first four bands are attributed to the OH stretching mode of the three inner surface hydroxyl groups, and the band at  $3620\text{-}3623\text{ cm}^{-1}$  belongs to the stretching mode of the inner OH group. The OH bands have been shown with Raman and IR spectroscopy to shift with temperature because of extreme sensitivity to minor changes in the kaolinite structure as a function of temperature [68,78]. For example, it

has been shown that the band attributed to the inner hydroxyl shifts by  $5\text{ cm}^{-1}$  from  $3620$  to  $3615\text{ cm}^{-1}$ , and the bands assigned to the inner surface hydroxyls move to higher frequencies due to cooling to  $77\text{ K}$  [67,79]. Other kaolinite IR vibrations include the apical Si-O ( $1115\text{ cm}^{-1}$ ), the Si-O-Si in-plane ( $1033$  and  $1008\text{ cm}^{-1}$ ), and the OH bending ( $937$  and  $914\text{ cm}^{-1}$ ) and OH translational ( $795$  and  $755\text{ cm}^{-1}$ ) vibrations [77], both likely attached to the Al atoms.

Several experimental studies have been published on IR and Raman spectroscopy of formamide-intercalated-kaolinite [67,80,81]. Upon intercalation of the kaolinite with liquid formamide, an additional Raman band attributed to the formation of a hydrogen-bonded complex between the inner surface hydroxyls and the C=O group of the formamide is observed at  $3627\text{-}3628\text{ cm}^{-1}$  at  $298\text{ K}$  and at  $3631\text{ cm}^{-1}$  at  $77\text{ K}$  [67]. Two Raman-active bands for hydrogen-bonded inner surface OH bands in ordered clays were seen at  $3628\text{ cm}^{-1}$  and  $3610\text{ cm}^{-1}$  [80,82]. The C=O group was determined to be linearly linked with the inner surface OH group, indicating vibrational symmetry which results in the vibration being only Raman-active. Diffuse Reflectance Infrared Fourier Transform Spectroscopy (DRIFTS) has been reported and shows a shift in the Al-OH deformation band from  $930\text{ cm}^{-1}$  to  $933\text{ cm}^{-1}$ , and an additional peak at  $1667\text{ cm}^{-1}$  was assigned to C=O hydrogen bonding to an inner surface hydroxyl of kaolinite. In addition, two bands at  $3336\text{ cm}^{-1}$  and  $3466\text{ cm}^{-1}$  correspond to two types of hydrogen bonding between the siloxane layer of kaolinite and the amide group of formamide [82]. Another study [83] involving intercalation of formamide into kaolinite after grinding and heating ( $230\text{-}350\text{ }^{\circ}\text{C}$ , in Argon atmosphere) presented DRIFTS bands representing Al-O=C=O and similar structures. Most notable are the bridge complex from  $1817\text{-}1755\text{ cm}^{-1}$  (with

C=O bridged between two O-Al bonds) and the bidentate complex from 1698-1637  $\text{cm}^{-1}$  (with C=O bridged between one Al bonded to two O connected to the carbon).

Although many studies focus on formamide-kaolinite intercalation, for the purpose of understanding kaolinite's role as a surface in prebiotic environments, it is imperative to also study the interfacial interaction of kaolinite with formamide under ultra-high vacuum conditions. This research focuses on the fundamental IR vibrations of formamide on kaolinite surfaces [56]. These interactions are studied both experimentally and theoretically. The experimental approach uses typical surface science techniques and report transmission Fourier Transform-Infrared (FT-IR) spectra as a function of temperature. The binding energies for formamide adsorbed on kaolinite have also been measured [56] using Temperature Programmed Desorption (TPD).

In a companion theoretical paper not detailed in this thesis [57], our collaborators investigated the adsorption of formamide on non-hydrated tetrahedral and octahedral surfaces of kaolinite. The presence of water and sodium cation(s) were also examined. The results showed that the binding of formamide to the kaolinite surfaces is governed by the surface termination and presence of sodium cation(s). Formamide adsorbs due to the formation of hydrogen bonds with the cation free surfaces, but formamide is chemisorbed in the case of non-hydrated octahedral surfaces containing a sodium cation. The optimized formamide-kaolinite adsorption structures obtained in the companion paper [57] are used to calculate the theoretical IR spectra provided for comparison to the experiments presented here.

## 2.2 Experimental Details and Theoretical Methods

### 2.2.1 Sample Preparation and Experimental Approach

Transmission IR measurements were performed using a Bruker Equinox 55 FT-IR spectrometer coupled to a stainless steel ultra-high vacuum (UHV) chamber (base pressure  $\sim 1 \times 10^{-10}$  Torr) with an external LN<sub>2</sub> cooled HgCdTe (MCT mid-IR) detector. The chamber shown schematically in Figure 2.1 was built for simultaneous FT-IR and TPD measurements. ZnSe windows allow for IR transmission to the sample, and off-axis parabolic mirrors direct the IR light into the chamber and out into the HgCdTe detector through a purged enclosure. The FT-IR and external beam path were both purged with N<sub>2</sub>. The IR spectra were recorded in the range of 4000-400 cm<sup>-1</sup> with 2 cm<sup>-1</sup> resolution averaged over 250 scans using OPUS software from Bruker. Smoothing and baseline correction of the spectra were done carefully to prevent loss of spectral features.

The UHV chamber is also equipped with a quadrupole mass spectrometer (QMS) with an electron impact ionization source to detect the neutral species desorbing from the sample surface. The TPD measurements were obtained with a custom Labview program that controlled the QMS and maintained a linear temperature ramp (0.5 K/s) by controlling the heater power supply and providing a feedback loop to the computer.

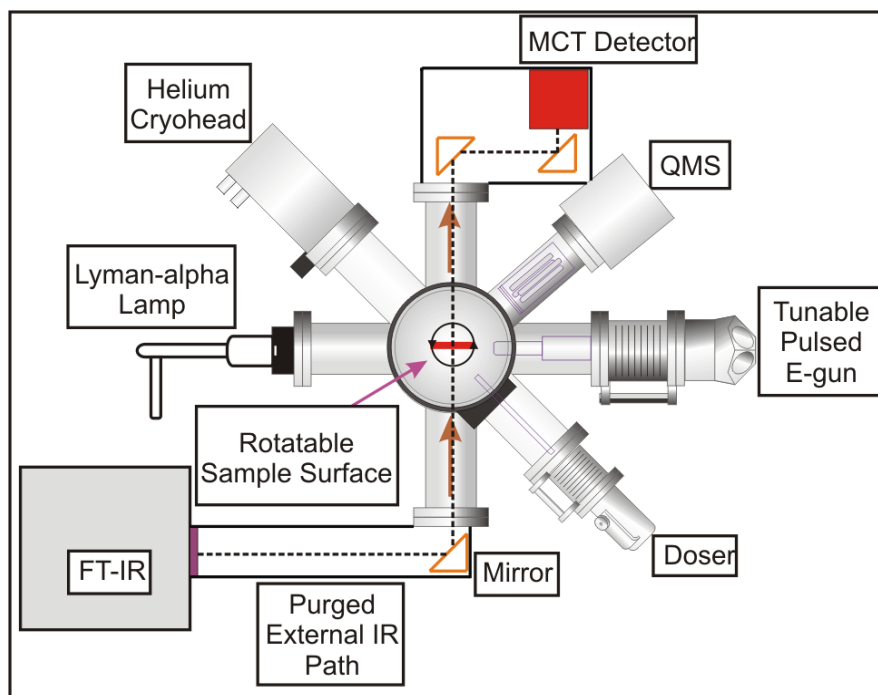


**Figure 2.1:** Schematic representation of the experimental ultra-high vacuum (UHV) chamber. The system is equipped with a temperature controlled sample holder connected to the helium cryostat, a quadrupole mass spectrometer (QMS), and ZnSe windows for transmission of the IR beam from the FT-IR spectrometer through the chamber, onto the sample, and out to the external HgCdTe (MCT) detector.

A 1" × 1" Ni wire mesh purchased from Buckbee-Mears with ~ 57% transmission and 134 lines per inch was used to mount the kaolinite sample in the UHV chamber. Total surface area of the mesh without kaolinite was  $8.31 \times 10^{-4} \text{ m}^2$ . Kaolinite powder (BET surface area is  $9.2341 \text{ m}^2/\text{g}$ ) was purchased from Sigma-Aldrich. The Ni mesh was dip-coated with a mixture of 0.55 g kaolinite to 2.5 mL nanopure H<sub>2</sub>O, and the weight of kaolinite on the mesh was 0.0034 g. The mesh was baked in an oven at 110 °C overnight to remove the H<sub>2</sub>O from the kaolinite. The kaolinite-coated mesh was then spot-welded to two horizontal pieces of tantalum attached to the sample holder, leaving the center of the mesh open for FT-IR transmission measurements. The tantalum strips were attached to ultrapure oxygen-free copper bars that connect the sample holder to a

closed-cycle helium cryostat that sits vertically in the UHV chamber. See Figure 2.2 below for a picture and drawing of the sample holder used with kaolinite powder affixed to it for mineral transmission FT-IR and TPD measurements under vacuum.

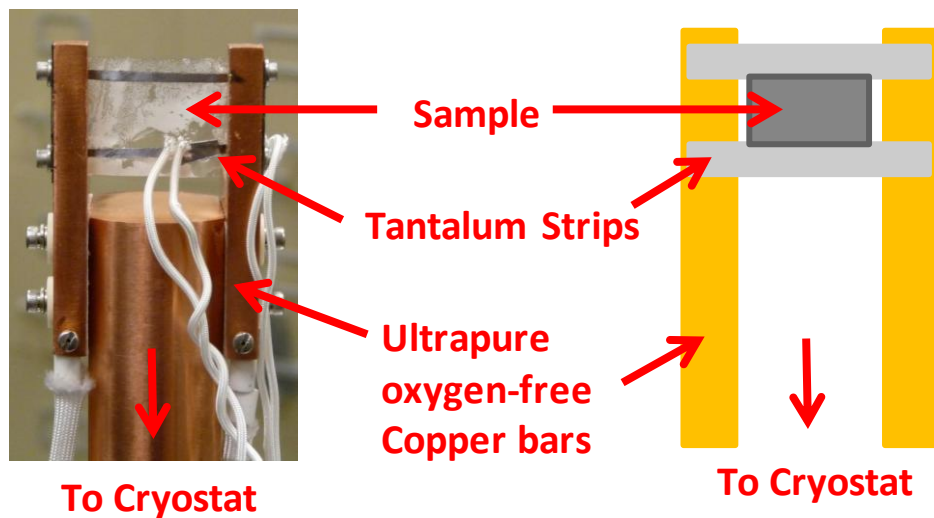


**Figure 2.2:** Picture (left) and drawing (right) of the sample holder and substrate used for transmission FT-IR spectroscopy and TPD measurements of grain/mineral analogs under UHV conditions.

The tantalum strips allowed for effective heating and cooling of the wire mesh sample with a range of ~67 to 800 K. A type-K thermocouple was spot-welded to the sample for temperature measurement. A high-current feedthrough (30 amps) allows for effective heating of the sample. The kaolinite-coated sample holder was never heated above 600 K to prevent removal of hydroxyls [84]. The whole sample holder construction was attached to a rotation stage to allow for 360° horizontal rotation within the chamber. Once the kaolinite-coated sample had been affixed to the holder, the chamber was sealed, evacuated, and baked at 100 °C for 24-48 hours to remove contaminants from the sample.

Formamide was purchased from VWR International. The formamide vapor was dosed on the sample (67-300 K) in the chamber by a precision leak valve from a

dedicated dosing line, and the pressure was monitored by an ion gauge near the sample to maintain a controlled chamber pressure for a specific time. Doses of 1 Langmuir (L) up to ~250 L were employed. While a Langmuir equals 1 monolayer coverage for single crystal flat surfaces [51], a powder surface is more complex. Assuming unity sticking probability at low temperatures, and a calculated arrival rate of  $3.02 \times 10^{14}$  molecules  $\text{cm}^{-2}\text{s}^{-1}$  for formamide, we estimate [51] that monolayer coverage equals ~10-25 L dosed. The dosing line was equipped with a turbo-molecular pump and was baked (60-100 °C) during and after each experiment to keep the line clean. The formamide liquid was purified by freeze-pump-thawing cycles prior to dosing. The line often had to be heated to 60 °C to effectively facilitate dosing since formamide's vapor pressure is very low. IR measurements were obtained before and after dosing of formamide once the chamber pressure equilibrated. Heating of the sample for TPD measurements was done after an IR spectrum of the dosed formamide was obtained and once the chamber pressure equilibrated after dosing. The sample was cleaned between experiments by flashing to 600 K.

For the formamide liquid IR spectrum (see Section 2.3.1), the UHV chamber was not needed, and the internal sample compartment and internal DTGS detector of the Bruker instrument were used instead. The liquid sample was pressed between two NaCl plates and was placed in the sample holder of the sample compartment for the transmission IR measurement at ambient pressure and temperature.

Pre-mixed formamide-kaolinite slurry experiments were also carried out for comparison with the formamide-adsorbed experiments. A mixture of 0.55 g kaolinite to 2.5 mL formamide was deposited wet onto a clean Ni mesh affixed to the sample holder

outside of vacuum. The sample holder assembly was then placed in the vacuum chamber. The chamber was subsequently put under vacuum ( $\sim 2 \times 10^{-9}$  Torr). The sample was cooled to 80 K, and the IR spectrum was measured. A thick formamide ice was then dosed (1100 L) onto the pre-mixed formamide-kaolinite slurry, and IR spectra were also obtained for a comparison of the formamide vibrations.

### **2.2.2 DFT Methods Used by Collaborators**

The calculations of the IR spectra of all formamide-kaolinite complexes studied were performed by our collaborators at Jackson State University using the density functional theory with the newly developed M05-2X functional [85-87] and 6-31G(d) basis set [88] as implemented in the Gaussian09 program package [89]. M05-2X is a high non-locality functional with double the amount of nonlocal exchange (2X) that is parameterized only for nonmetals. This functional has shown the best performance for thermochemical kinetics and noncovalent interactions (especially weak interactions such as hydrogen bonding) [85,86]. For all optimized structures of the calculated systems, the harmonic vibrational frequencies were calculated and scaled with factors established by Merrick and co-workers [90]. The IR spectra of the formamide molecule were also calculated using larger basis sets (6-31G(d,p) and 6-31+G(d,p)) to test the accuracy of this level of theory in calculations of the vibrational frequencies. Two different scaling factors of vibrational frequencies have been employed as recommended by Merrick et al. [90]. For the method and basis set used (M05-2X/6-31G(d)), the authors suggest 0.9364 as frequency scale factor for low-frequency vibrations ( $< 1800 \text{ cm}^{-1}$ ) and 0.9373 for fundamental vibrations ( $> 1800 \text{ cm}^{-1}$ ).

The modeling of the kaolinite mineral was performed using the crystal structure data [91] of this mineral. The chemical formula of kaolinite is the following:  $\text{Al}_2\text{O}_9\text{Si}_2\text{H}_4$ . This layered aluminosilicate consists of a  $\text{SiO}_4$  tetrahedra sheet connected with a gibbsite-like (dioctahedral)  $\text{Al}(\text{OH})_3$  sheet. The model of kaolinite was constructed as a cut off from its periodic structure so that it contains one ring of the octahedral sheet connected with one ring of the tetrahedral sheet. Dangling bonds of the cluster model, which occur due to the cut off, were saturated by hydrogen atoms. The number of silicon, aluminum, oxygen and hydrogen atoms included in the clusters employed to model the kaolinite mineral are reflected in the stoichiometric formula of the cluster:  $\text{Al}_6\text{Si}_6\text{O}_{36}\text{H}_{30}$ , with the total number of atoms equal to 78.

More specific details regarding the calculations and modeling can be found in the companion paper [57] including an explicit description of the model construction and properties calculated. The optimized structures of formamide adsorbed on the octahedral and tetrahedral kaolinite surfaces used to calculate the IR spectra are illustrated in Figure 2.3, courtesy of Andrea Michalkova Scott [56]. Other optimized structures of formamide adsorbed on different kaolinite surfaces as well as a discussion of the interactions and energetics of all formamide-kaolinite complexes are presented in the companion paper [57]. Abbreviations used in the text and tables include K(o) for the octahedral side of kaolinite, K(o)-FA for the adsorption of formamide on octahedral side of kaolinite, K(t) for the tetrahedral side of kaolinite, and K(t)-FA for the adsorption of formamide on tetrahedral side of kaolinite.

Due to a fact that calculated vibrational spectra are obtained using the cluster model of kaolinite, in which dangling bonds on the edges are saturated by hydrogen

atoms, discussion of the theoretical results concentrates on vibrational features of formamide and changes of the IR bands upon adsorption. Discussion of the IR spectra of bare kaolinite focuses on the experimental results and comparison with other already published experimental IR spectra of kaolinite [68,78,92].

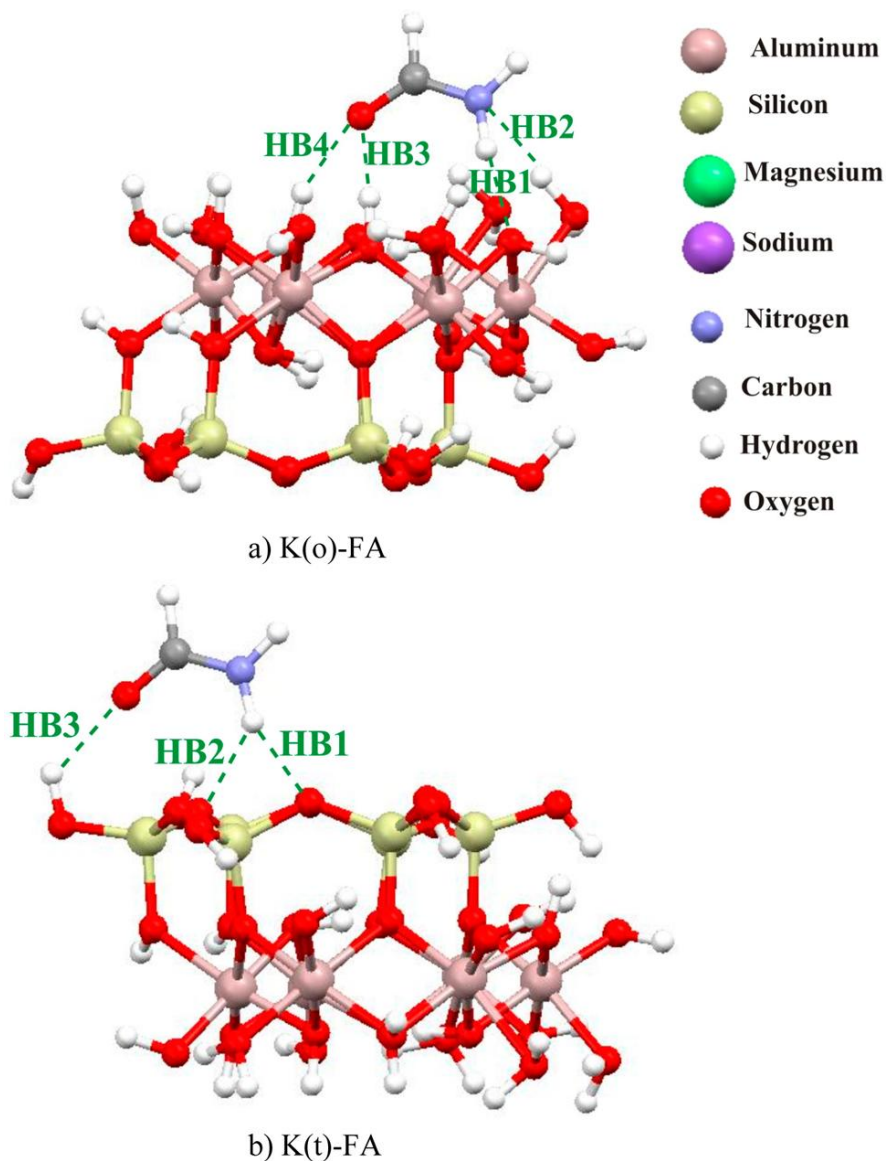


**Figure 2.3:** The optimized structure of formamide adsorbed on octahedral (a, K(o)-FA) and tetrahedral surface (b, K(t)-FA) of kaolinite used to calculate infrared spectra. Figure courtesy of Andrea Michalkova Scott.

## 2.3 Results

### 2.3.1 Infrared Spectrum of Liquid Formamide

The transmission IR spectrum of formamide liquid taken at ambient temperature is presented in Figure 2.4(a). To compare, the theoretical spectra for formamide calculated in gas phase (denoted t) and liquid phase (in blue denoted l) at the M05-2X/6-31G(d) level are also illustrated in Figure 2.4. Assignments given in Table 2.1 were made based on literature values for gas, liquid, and condensed phase (frozen) samples [24,93-98].

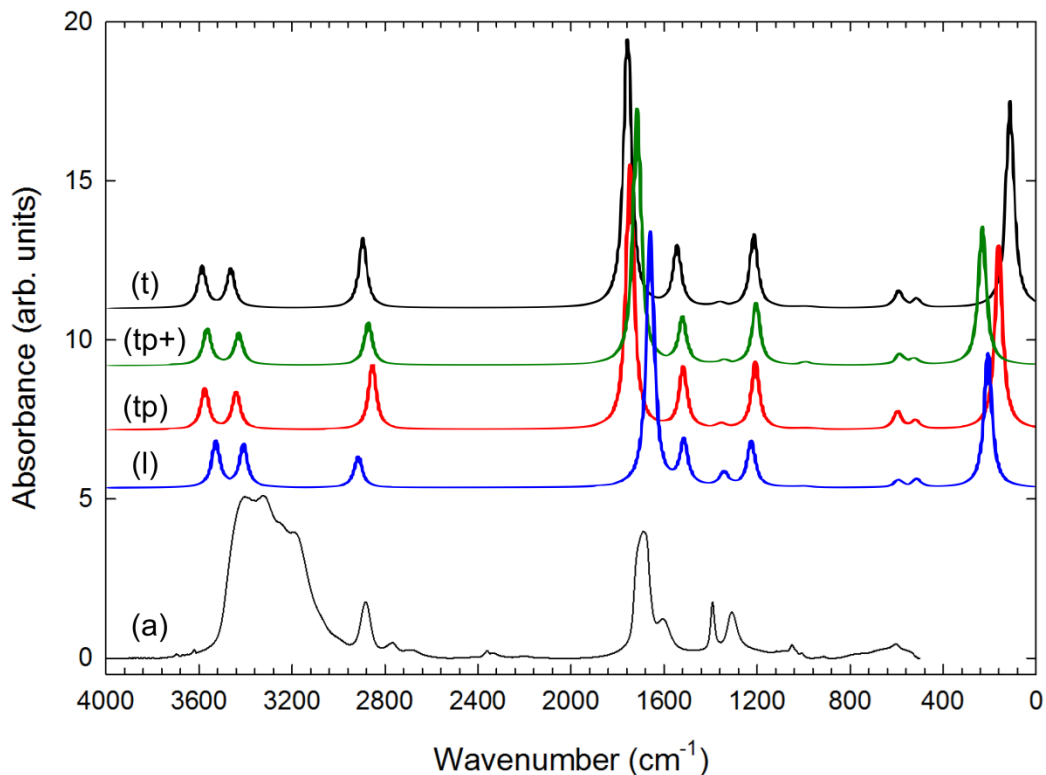


**Figure 2.4:** Experimental transmission infrared spectrum of pure formamide liquid (a) compared to formamide calculated in the gas phase (t) and liquid phase (l, blue) at the M05-2X/6-31G(d) level. Spectra of formamide calculated using 6-31G(d,p) (tp) and 6-31G(d,p) (tp+) larger basis sets are also shown for comparison (red and green, respectively). Experimental spectra offset, baseline corrected and smoothed for ease of comparison.

**Table 2.1:** Experimental infrared vibrations for formamide liquid compared to theoretical values (obtained with M05-2X/6-31G(d), M05-2X/6-31G(d,p) and M05-2X/6-31+G(d,p), scaled by 0.9364 and 0.9373) for formamide in gas phase and liquid phase. See Figure 2.4 for corresponding IR spectra.

Assignment [24,93-98]	FA Exp. Liquid (a)	FA Liquid Th.(l) 6-31G(d)	FA Th. (t) 6-31G(d)	FA Th. (tp) 6-31G(d,p)	FA Th.(tp+) 6-31+G(d,p)
$\nu_1$ (NH <sub>2</sub> asym. str.)	3422	3536	3567	3584	3574
$\nu_2$ (NH <sub>2</sub> sym. str.)	3321	3418	3444	3449	3438
$\nu_3$ (CH str.)	2883, 2766, 2683	2928	2885	2865	2882
$\nu_4$ (C=O str.)	1688	1680	1761	1757	1726
$\nu_5$ (In-plane NH <sub>2</sub> sci.)	1604	1537	1550	1529	1531
$\nu_6$ (In-plane CH sci.)	1392	1365	1392	1364	1352
$\nu_7$ (C-N str.)	1313	1249	1224	1219	1214
$\nu_8$ (In-phase NCO/NH <sub>2</sub> bend)	1050	1025	1008	1002	1002
$\nu_9$ (Out-of-phase NCO/NH <sub>2</sub> bend)	*	545	534	532	536
$\nu_{10}$ (Out-of-plane CH def.)	1009	1025	1010	1012	1002

\* = too close to detection limit of detector to give accurate value

### 2.3.2 Infrared Spectra of Kaolinite

Figure 2.5 shows the experimental IR spectra of kaolinite. The transmission IR spectra of kaolinite powder taken at sample temperatures of 300 K (a) and 110 K (b) are presented. Only the regions of interest showing the kaolinite vibrations are presented. There are no appreciable peaks in the omitted region ( $3575\text{-}1200\text{ cm}^{-1}$ ) of Figure 2.5. Table 2.2 presents a corresponding list of the experimental assignments.

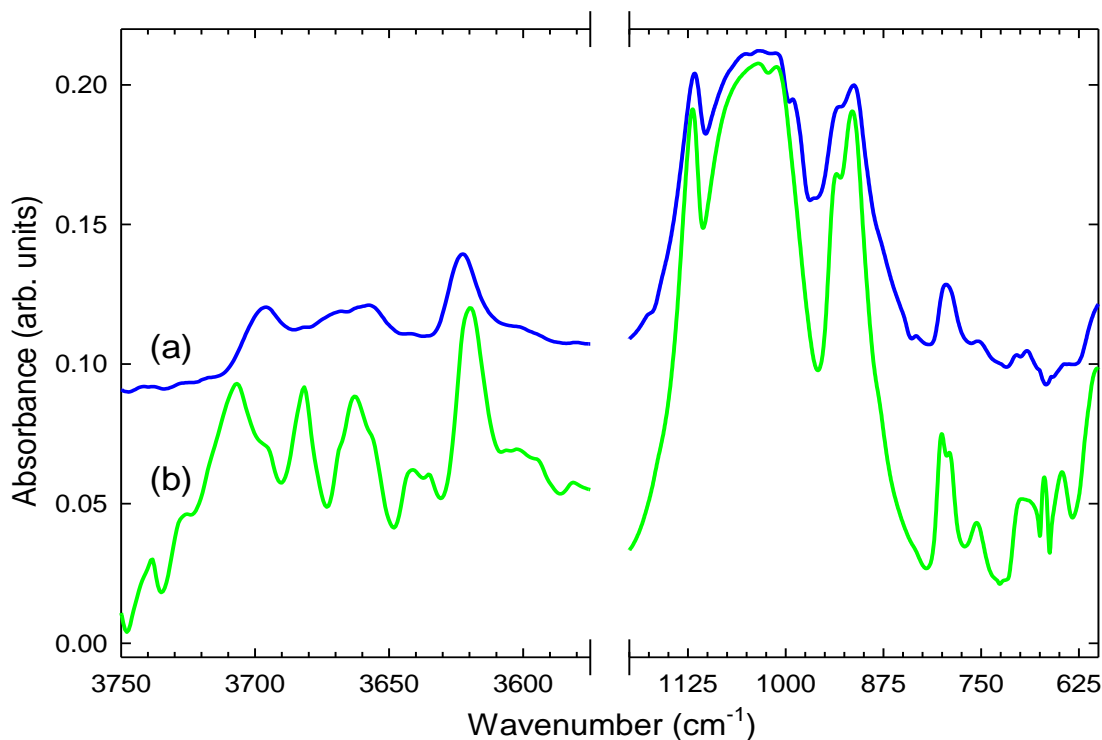


**Figure 2.5:** Experimental transmission infrared spectra of kaolinite powder at (a) 300 K and (b) 110 K. Spectra offset, baseline corrected and smoothed for ease of comparison.

**Table 2.2:** Experimental infrared vibrations for kaolinite powder at sample temperatures of 300 K and 110 K. See Figure 2.5 for corresponding IR spectra.

Assignment	300 K Exp.	110 K Exp.
Inner surface OH str.	3699	3707
Inner surface OH str.	3674	3682
Inner surface OH str.	3654	3663
Inner OH str.	3621	3620
Apical Si-O	1120	1120
Si-O-Si in-plane bend	1031, 1012	1031, 1012
Inner surf OH def.	935	935
Inner OH def.	913	913
Al-OH bend	793, 755	800 & 790 (split), 755

### 2.3.3 Infrared Spectra of Formamide Adsorbed on Kaolinite

#### 2.3.3.1 Kaolinite Vibrations

Figure 2.6 illustrates the experimental transmission IR spectra and calculated IR spectra of *kaolinite vibrations* after exposure to formamide. Formamide dosed in these experiments was between 13 and 25 L to obtain near monolayer coverage. Substrate temperatures studied were 300 K (a), 110 K (b) and 67 K (c). The theoretical (t) spectrum of adsorbed formamide on the octahedral surface of kaolinite (K(o)-FA) calculated at 110 K is illustrated in Figure 2.6 only for comparison purposes. The corresponding frequencies are given in Table 2.3, including additional calculated vibrations for formamide adsorption on the tetrahedral surface of kaolinite (K(t)-FA). The optimized structures of formamide adsorbed on the octahedral and tetrahedral kaolinite surfaces used to calculate the IR spectra are illustrated in Figure 2.3.

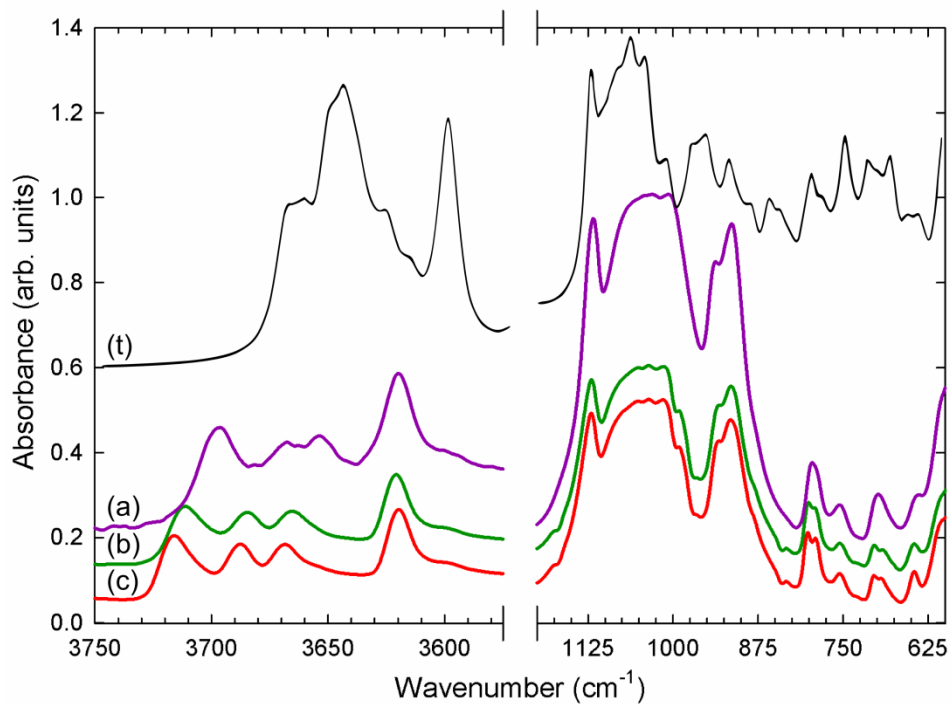


**Figure 2.6:** Experimental transmission infrared spectra of *kaolinite vibrations* when formamide is exposed to kaolinite at (a) 300 K, (b) 110 K, (c) 67 K, and theoretical spectrum (t) of adsorbed formamide on the octahedral surface of kaolinite calculated at 110 K. Experimental spectra offset, baseline corrected and smoothed for ease of comparison.

**Table 2.3:** Experimental infrared *kaolinite vibrations* for formamide adsorbed on kaolinite at 67 K, 110 K, and 300 K compared to theoretical values (obtained at 110 K using M05-2X/6-31G(d), scaled by 0.9364 and 0.9373) for formamide adsorbed on the octahedral surface of non-hydrated kaolinite (K(o)-FA) and formamide adsorbed on the tetrahedral surface of non-hydrated kaolinite (K(t)-FA). See Figure 2.6 for corresponding IR spectra.

Assignment	300 K Exp.	110 K Exp.	67 K Exp.	K(o)-FA	K(t)-FA*
Inner surface OH str.	3696	3711	3716	-	-
Inner surface OH str.	3668	3685	3688	3673	3687
Inner surface OH str.	3654	3665	3668	3604,3554, 3504, 3408	3655, 3551, 3406
Inner OH str.	3620	3621	3620	3630	3623
Outer OH str.	-	-	-	3473	3587
Apical Si-O	1120	1120	1120	1123	1115
Si-O-Si in-plane bend	1036, 1014	1036, 1014	1036, 1015	1086	1093
Inner surf OH def.	935	932	935	951	934
Inner OH def.	914	915	915	914	918
Al-OH bend	795, 755	800 & 792 (split), 755	802 & 791 (split), 755	782, 748	776, 759

\* = not shown in Figure 2.6

### 2.3.3.2 Formamide Vibrations

Figure 2.7 gives the experimental and calculated IR spectra of *formamide vibrations* (C=O stretch, CH scissor, and C-N stretch) when formamide is dosed as a function of temperature onto kaolinite compared to spectra of a pre-mixed formamide-kaolinite slurry taken at 80 K (b) and subsequent formamide dosed (1100 L) on the slurry also at 80 K (a). Spectra taken when formamide is dosed onto kaolinite (25-50 L doses) at temperatures ranging from 67-140 K are presented. Note the spectra were obtained when the sample was cooled to 67 K after dosing to prevent temperature effects on the vibrations. The background kaolinite spectrum has been subtracted out to highlight features from formamide or formamide surface interactions. As a comparison, the theoretical (t) spectrum of adsorbed formamide on the octahedral surface of kaolinite (K(o)-FA) calculated at 110 K is also shown. Figure 2.8 shows the NH stretching region (top pane) and the CH stretching region (bottom pane) for the experimental (67-140 K) and calculated (t) formamide vibrations when formamide is dosed onto kaolinite and then compared to the pre-mixed formamide-kaolinite slurry (b) and subsequent formamide dosed on the slurry (a). Table 2.4 summarizes the experimental and theoretical IR formamide vibrations at relevant sample temperatures while dosing at 110, 100, and 67 K, with comparison to the calculated spectra and the experimental frequencies of the pre-mixed slurry and subsequent formamide dosed on the slurry, both taken at 80 K. See Section 2.4.4 for a detailed discussion of the temperature dependence and explanation of experimental spectral signatures from Figures 2.7 and 2.8.

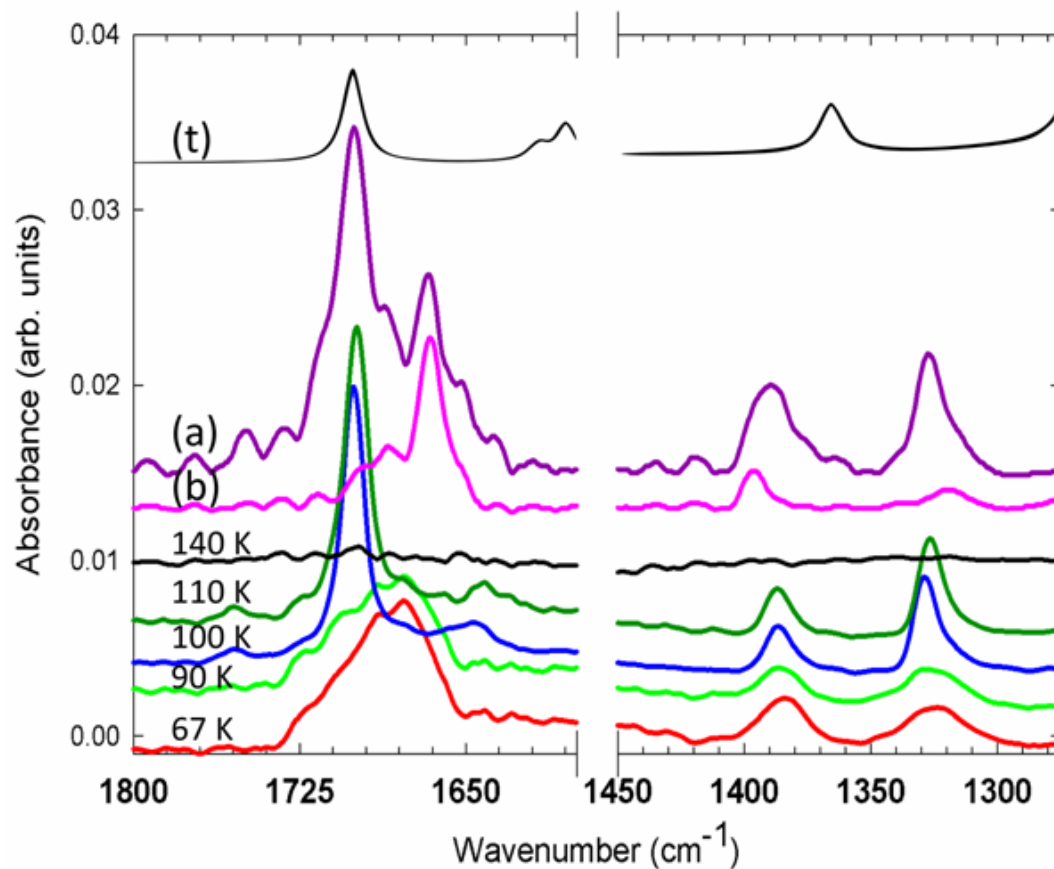


**Figure 2.7:** Transmission infrared spectra of *formamide vibrations* (C=O stretch, CH scissor, and C-N stretch) when formamide is dosed onto kaolinite at temperatures between 67-140 K (all spectra recorded at 67 K after dosing) compared to the pre-mixed formamide-kaolinite slurry (b) at 80 K in which intercalation is most likely evident and subsequent formamide dosing (a) (~1100 L, dosed at 80 K) onto the pre-mixed slurry. The theoretical (t) spectrum of adsorbed formamide on the octahedral surface of kaolinite (K(o)-FA) calculated at 110 K is also shown. Experimental spectra offset, baseline corrected and smoothed for ease of comparison.

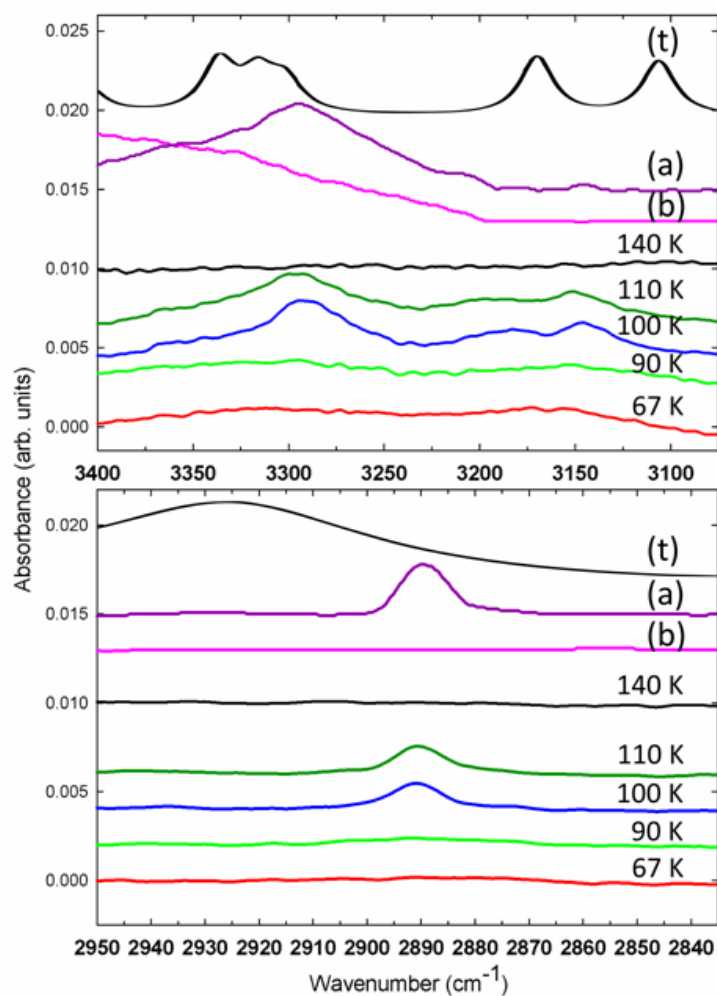


**Figure 2.8:** Transmission infrared spectra of *formamide vibrations* (top pane - NH stretches, bottom pane - CH stretch) when formamide is dosed onto kaolinite at temperatures between 67-140 K (all spectra recorded at 67 K after dosing) compared to the pre-mixed formamide-kaolinite slurry (b) at 80 K in which intercalation is most likely evident and subsequent formamide dosing (a) (~1100 L, dosed at 80 K) onto the pre-mixed slurry. The theoretical (t) spectrum of adsorbed formamide on the octahedral surface of kaolinite (K(o)-FA) calculated at 110 K is also shown. Experimental spectra offset, baseline corrected and smoothed for ease of comparison.

**Table 2.4:** Experimental infrared *formamide vibrations* for formamide adsorbed on kaolinite at dosing temperatures of 67 K, 100 K, 110 K compared to theoretical values (obtained at 110 K using M05-2X/6-31G(d), scaled by 0.9364 and 0.9373) for formamide adsorbed on the octahedral surface of non-hydrated kaolinite (K(o)-FA) and formamide adsorbed on tetrahedral surface of non-hydrated kaolinite (K(t)-FA). Frequencies for the formamide-kaolinite pre-mixed slurry at 80 K and then for subsequent formamide dosed on the slurry at 80 K are also given for comparison. See Figures 2.7 and 2.8 for corresponding IR spectra.

Assignment	110 K Exp.	100 K Exp.	67 K Exp.	Pre- mixed slurry	Slurry+FA	K(o)-FA	K(t)-FA **
$\nu_1$ (NH <sub>2</sub> asym. str.)	3297	3295	-	-	3297	3490	3546
$\nu_2$ (NH <sub>2</sub> sym. str.)	3154	3148	3157 (w)	-	3149 (w)	3112	3414
$\nu_3$ (CH str.)	2891	2891	-	-	2891	2926	2934
$\nu_4$ (C=O str.)	1700	1701	1682	1685, 1667	1701, 1668	1706	1718
$\nu_5$ (In-plane NH <sub>2</sub> sci.)	1647	1649	-	-	1652 (sh)	1585, 1597	1569
$\nu_6$ (In-plane CH sci.)	1389	1388	1386	1396	1391	1371	1373
$\nu_7$ (C-N str.)	1328	1330	1326	1318	1329	1273	1275
$\nu_8$ (In-phase NCO/NH <sub>2</sub> bend)	-	-	-	-	-	1061	1031
$\nu_9$ (Out-of-phase NCO/NH <sub>2</sub> bend)	*	*	-	-	-	531	705
$\nu_{10}$ (Out-of-plane CH def.)	-	-	-	-	-	1024	1023

(w) = weak vibration; (sh) = shoulder; \* = too close to detection limit of detector to give accurate value; no vibration given means no signal above noise level

\*\* = not shown in Figures 2.7 and 2.8, given for comparison only.

### 2.3.4 TPD of Formamide on Kaolinite

Temperature Programmed Desorption (TPD) of formamide (mass 45) after formamide adsorption on kaolinite was performed to experimentally determine activation energies of desorption. See Figure 2.9 for a representative TPD of formamide after adsorption of 13 L of formamide dosed at 110 K (near monolayer coverage) onto kaolinite powder. The TPD was started after cooling the sample to 67 K. It is clear from Figure 2.8 that desorption from kaolinite begins near 140 K, with peak maximum at ~186 K. Desorption is near completion by ~300 K. This agrees well with the IR spectra at 140 K shown in Figures 2.7 and 2.8, where no formamide vibrations are seen at this temperature, indicating desorption of formamide from the surface of the kaolinite. One broad TPD physisorption peak indicates slow diffusion through the kaolinite.

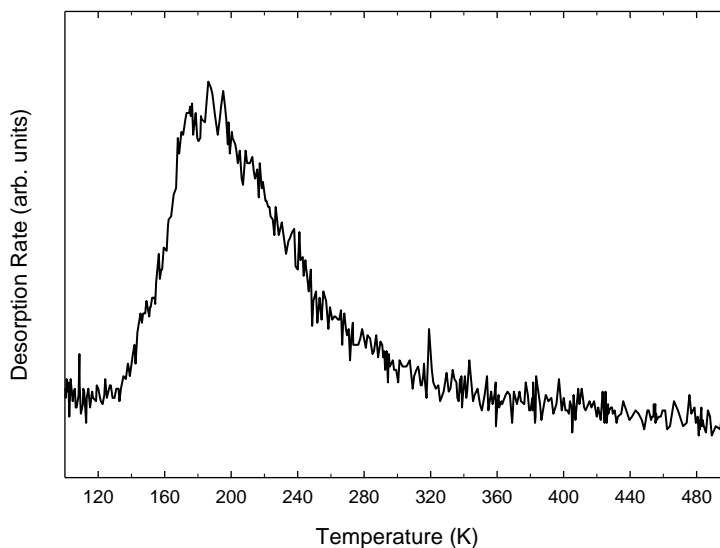


**Figure 2.9:** TPD of mass 45 (formamide) after adsorption of 13 L formamide on kaolinite powder at 110 K. TPD taken after cooling sample to 67 K; Ramp rate = 0.5 K/s.

## 2.4 Discussion

### 2.4.1 Comparison of IR Spectrum of Formamide to Theoretical Spectra

The calculated fundamental vibrations of formamide show generally good agreement with both published data [93,95,96,98,99] and with our experimental IR spectrum (see Figure 2.4 and Table 2.1). In the region above  $3000\text{ cm}^{-1}$ , the gas-phase bands (t) calculated for symmetric and asymmetric  $\text{NH}_2$  stretching at  $3444\text{ cm}^{-1}$  and  $3567\text{ cm}^{-1}$  (and liquid phase at  $3418\text{ cm}^{-1}$  and  $3536\text{ cm}^{-1}$ ) show good agreement with prior experimental and theoretical values ( $3448, 3570, 3403, 3542\text{ cm}^{-1}$ ) [94,96]. Our collaborators also calculated three vibrations for gas-phase formamide at  $1224, 1761$  and  $2885\text{ cm}^{-1}$  (at  $1249, 1680$  and  $2928\text{ cm}^{-1}$  for liquid phase) which are attributed to C-N, C=O and CH stretching, respectively. The gas-phase theoretical bands correspond well with the experimentally measured bands of King et al. ( $1255, 1755$  and  $2855\text{ cm}^{-1}$ ) [96]. In a prior theoretical study [94], these bands were calculated at  $1198, 1707, 2803\text{ cm}^{-1}$ . We assign the theoretical gas-phase band at  $1550\text{ cm}^{-1}$  ( $1537\text{ cm}^{-1}$  for liquid) to in-plane  $\text{NH}_2$  scissors, and it is shifted to lower frequency (by about  $30$  and  $40\text{ cm}^{-1}$ ) when compared with prior experimental IR spectra [96,98] of formamide, in which the  $\text{NH}_2$  scissors band is seen  $\sim 1580\text{ cm}^{-1}$ . However, in a prior theoretical study, the MP2/6-311G(d,p) level calculations show a frequency of  $1518\text{ cm}^{-1}$  for the  $\text{NH}_2$  scissors [94]. The in-plane CH scissors mode for formamide was observed by King et al. [96] at  $1390\text{ cm}^{-1}$ , which is consistent with  $1392\text{ cm}^{-1}$  calculated for gas-phase formamide by our collaborators. This vibration also matches our experimental liquid value at  $1392\text{ cm}^{-1}$ . On the other hand, it is higher than that obtained in the theoretical study [94] calculated at the MP2 level ( $1345\text{ cm}^{-1}$ ), which is close to our calculated liquid phase value at  $1365\text{ cm}^{-1}$ .

Additional peaks for the NH<sub>2</sub> bending and NH<sub>2</sub> out-of-phase deformation are calculated at 1008 and 534 cm<sup>-1</sup> (calculated liquid values are 1025 and 545 cm<sup>-1</sup>) in our work. Similarly, these values are only slightly shifted compared with the results in other published studies [93,94]. The out-of-plane CH deformation mode is also shifted (by about 20-40 cm<sup>-1</sup>) to lower frequency (1010 cm<sup>-1</sup> in gas phase) than observed in another report at 1055 and 1032 cm<sup>-1</sup> [99]. However, our calculated value matches well with our own experimental work (1009 cm<sup>-1</sup>). The 1032 cm<sup>-1</sup> value [99] is consistent with our calculated liquid phase band at 1025 cm<sup>-1</sup>. Based on the overall good agreement with prior experimental and calculated frequencies as well as with our own experimental values, it was determined that the calculations for the fundamental bands of formamide are within reason to proceed with calculations of formamide's interaction with kaolinite.

Here, the IR spectra of isolated formamide obtained using 6-31G(d,p) and 6-31+G(d,p) basis sets by our collaborators will be briefly discussed, which are also given in Table 2.1 and illustrated in Figure 2.4 (red and green, denoted as tp and tp+). These calculations using larger basis sets lead to insignificant changes in the vibrational frequencies (mostly less than 20 cm<sup>-1</sup>) when compared with the 6-31G(d) gas-phase results. A slightly larger difference (of about 30-40 cm<sup>-1</sup>) was found only for the C=O stretching (6-31+G(d,p)) and in-plane CH scissors bands (using both 6-31G(d,p) and 6-31+G(d,p) basis sets). However, the theoretical frequency values obtained using the 6-31G(d) basis set showed better agreement with published experimental formamide frequencies [94-98] than the results obtained using the larger basis sets. This shows that such calculations provide reasonably accurate vibrational analysis data. Therefore, the M05-2X/6-31G(d) level of theory was used by our collaborators in all further calculations

of the IR spectra of the formamide-kaolinite adsorption complexes. Moreover, the 6-31G(d) basis set was employed in published theoretical studies of the vibrational frequencies of adsorbed systems on titanium silicalite catalysts using cluster and periodic models [100], and for the surface complex structures of carbonate, phosphate, sulfate, arsenate and arsenite [101].

#### **2.4.2 Changes in Kaolinite Hydroxyl IR Vibrations with Temperature**

IR vibrations can become sharp at lower temperatures and broad at higher temperatures, depending on the composition of the condensed phase and presence of hydrogen bonding. Bands that overlap at room temperature can become resolved into distinct bands at low temperatures [37]. The four major kaolinite OH vibrations between 3750-3600  $\text{cm}^{-1}$  sharpen and become more resolved with decreasing sample temperature in our experiments (see Figure 2.5 and Table 2.2). In addition, the inner surface hydroxyl stretches blue shift (to higher frequencies) as the sample temperature decreases. These temperature effects on the hydroxyl vibrations agree with previous experiments [68,92], and have been accounted for in terms of correlation with inter-layer hydrogen bonding distance changes as a function of temperature and contraction of the interlayer space [68]. Prior studies proposed that the higher frequency OH vibrations have the weakest participation in hydrogen bonding and correspond to the longest inter-layer OH...O distances [68]. Our assignments for the four primary OH stretches are consistent with prior low-temperature kaolinite IR studies [68]. Specifically, at 300 K, we see bands at 3699, 3674, 3654, and 3621  $\text{cm}^{-1}$ , whereas Johnston et al. [68] reported similar bands at 3691, 3669, 3652, and 3620  $\text{cm}^{-1}$ . At temperatures near 110 K, the prior study also reported frequencies within 5  $\text{cm}^{-1}$  of our values [68]. These results were for a Georgia

kaolin with a high Hinckley-Index, which is correlated with lower defect density [68]. In addition, a prior experimental and theoretical study by Balan et al. [102] reports the four OH stretching modes at 3695, 3669, 3652, and 3620  $\text{cm}^{-1}$  from their experiments, which are also within 10  $\text{cm}^{-1}$  or less of our values. In our experiments, the apical Si-O, Si-O-Si in-plane bending, and Al-OH bending modes show negligible shift with decreasing temperature, indicating a perturbation of primarily surface and inter-layer hydroxyls due to temperature. See Figure 2.5 and corresponding Table 2.2. Our assignments for the Si-O stretching modes are also consistent with those of Balan et al. [102], who report experimental frequencies at 1112  $\text{cm}^{-1}$ , 1103  $\text{cm}^{-1}$ , 1032  $\text{cm}^{-1}$ , and 1008  $\text{cm}^{-1}$ , which are also within 5-10  $\text{cm}^{-1}$  of our values. We also show a vibration for the Al-OH bending mode splitting to 800 and 790  $\text{cm}^{-1}$  from 793  $\text{cm}^{-1}$  as the temperature is lowered from 300 K to 110 K. Unlike the OH stretches, the OH deformation modes do not appear to shift with temperature. These are found at 935  $\text{cm}^{-1}$  and 913  $\text{cm}^{-1}$ , for inner surface OH deformation and inner OH deformation, respectively. Small differences in the frequencies compared to prior works could be the result of the sizes or shapes of the kaolinite particles used in these experiments or due to structural defects such as impurities and stacking faults in the OH groups of the sample [102]; however, the overall frequency agreement with a high Hinckley-Index kaolin suggests that our sample also has a low defect density.

### 2.4.3 Comparison of IR Spectra of Formamide Adsorbed on Kaolinite to Theoretical Spectra

Here, the formamide vibrations for formamide adsorbed on kaolinite calculated by our collaborators (K(o)-FA, K(t)-FA) are compared to the formamide-adsorbed experimental IR spectra (Table 2.4) and to the calculated spectrum of pure formamide (Table 2.1). Although the calculations are performed either with adsorption on the octahedral or tetrahedral face of kaolinite, note that the experiments cannot satisfactorily distinguish between the two different adsorption faces. However, later in the discussion it will be shown that the interactions occur more likely between formamide and the octahedral surface of kaolinite.

For the calculated K(o)-FA, a decrease in frequency (from 40 to 70  $\text{cm}^{-1}$ ) for formamide's  $\text{NH}_2$  symmetric stretching (3112  $\text{cm}^{-1}$ ),  $\text{NH}_2$  scissors (1585 and 1597  $\text{cm}^{-1}$ ), and C-N stretching (1273  $\text{cm}^{-1}$ ) was found when compared with our formamide-adsorbed experiments at 67-110 K. See Table 2.4. A smaller increase ( $\sim 30 \text{ cm}^{-1}$ ) for the CH stretching (from 2891  $\text{cm}^{-1}$  in the experiments to the calculated value of 2926  $\text{cm}^{-1}$ ) was revealed. However, a much larger increase (200  $\text{cm}^{-1}$ ) in the theoretical frequency was seen for the  $\text{NH}_2$  asymmetric stretching (from 3297  $\text{cm}^{-1}$  in the 110 K experiment to 3490  $\text{cm}^{-1}$  in the calculation). Our collaborators observed two bands theoretically for the  $\text{NH}_2$  stretching at 3112  $\text{cm}^{-1}$  and 3490  $\text{cm}^{-1}$ . The theoretical bands seen in the region of 3150-3350  $\text{cm}^{-1}$  correspond to the stretching vibrations of the terminated OH groups of the siloxane sheet that were added to the kaolinite cluster model to saturate the dangling bonds. The shifts in the theoretical  $\text{NH}_2$  stretches compared to the experiments can occur also because the band at 3112  $\text{cm}^{-1}$  represents NH that is hydrogen bonded with the

surface oxygen atom, and the band at  $3490\text{ cm}^{-1}$  represents NH that faces the free space, which is not hydrogen bonded with the octahedral surface. In the experiments, we do not observe such shifts and thus may not sample NH bonding with the kaolinite surface. On the other hand, a good consistency in theoretical and experimental values for the C=O stretching band at 110 K (calculated at  $1706\text{ cm}^{-1}$ , difference only  $6\text{ cm}^{-1}$ ) and only a slight decrease for the CH scissors mode (calculated at  $1371\text{ cm}^{-1}$ , difference about  $18\text{ cm}^{-1}$ ) was found.

A comparison of the calculated spectrum of K(o)-FA (Table 2.4) to the calculated spectrum of pure formamide (Table 2.1) shows the most significant shifts to lower frequencies for the  $\text{NH}_2$  stretching regions. For the  $\text{NH}_2$  symmetric band occurring at  $3444\text{ cm}^{-1}$ , this shift is  $\sim 330\text{ cm}^{-1}$  (from  $3112\text{ cm}^{-1}$ ), and for the asymmetric stretch occurring at  $3567\text{ cm}^{-1}$ , this shift is  $\sim 80\text{ cm}^{-1}$  (from  $3490\text{ cm}^{-1}$ ). For the calculated complex at 110 K, the shift in K(o)-FA NH stretches indicates that the  $\text{NH}_2$  group of formamide is involved in hydrogen bonds with the surface of kaolinite. The same conclusion about shifting of  $\text{NH}_2$  bands to lower frequencies (between  $3360$  and  $3507\text{ cm}^{-1}$ ) upon intercalation of formamide into kaolinite was made in a theoretical PM3 study [103]. The remaining formamide peaks are shifted by about  $50\text{ cm}^{-1}$  after the adsorption of formamide on the octahedral surface, which also demonstrates the tightly bound structure of formamide with kaolinite. Among other shifts is an increase in frequency of the C-N stretching vibration from that of pure formamide (shift of  $\sim 50\text{ cm}^{-1}$ ). A similar increase in frequency of this vibration was observed by Frost et al. experimentally for formamide-intercalated kaolinite (from  $1300\text{ cm}^{-1}$  to  $1320\text{ cm}^{-1}$ ) [80].

Our collaborators also calculated the formamide vibrations when formamide was adsorbed on the tetrahedral surface of kaolinite at 110 K (Table 2.4). In the case of K(t)-FA, only one peak was observed for the NH<sub>2</sub> scissors (1569 cm<sup>-1</sup>) instead of two seen for K(o)-FA. The rest of the vibrations in the range between 1250-1800 cm<sup>-1</sup> belong to the in-plane CH scissors (1373 cm<sup>-1</sup>), C=O stretching (1718 cm<sup>-1</sup>), and C-N stretching (1275 cm<sup>-1</sup>). All of these values are very close to the results obtained for formamide adsorbed on the octahedral surface of kaolinite (difference is less than 15 cm<sup>-1</sup>). On the other hand, the bands above 2900 cm<sup>-1</sup> assigned to CH stretching (2934 cm<sup>-1</sup>) and NH<sub>2</sub> stretching (3546 and 3414 cm<sup>-1</sup>) occur at much higher frequencies than in K(o)-FA. The theoretical spectrum of K(t)-FA also shows good agreement with the experimental values for the CH scissor and C=O stretching vibrations (difference is less than 20 cm<sup>-1</sup>). However, the NH<sub>2</sub> stretching and NH<sub>2</sub> scissor vibrations are shifted more in K(t)-FA than in K(o)-FA when compared to the experiment (~250 cm<sup>-1</sup> and ~80 cm<sup>-1</sup>, respectively).

Comparison of the calculated K(t)-FA spectrum (Table 2.4) with the calculated spectrum of pure formamide (Table 2.1) shows smaller vibrational shifts (from 10 to 50 cm<sup>-1</sup>) than found for the K(o)-FA complex. For example, the bands for NH<sub>2</sub> stretching are increased when compared with K(o)-FA, which leads to smaller shifts (20-30 cm<sup>-1</sup>) when comparing to formamide. In another theoretical study, a strong red shift was seen for the NH<sub>2</sub> stretching bands of formamide after intercalation into kaolinite [103]. The authors suggested that this shifts explains the hydrogen bonds formed with the siloxane ring. Moreover, the low frequency NH<sub>2</sub> bend (1031 cm<sup>-1</sup>) and CH deformation (1023 cm<sup>-1</sup>) vary only slightly (by less than 30 cm<sup>-1</sup>) from these bands in K(o)-FA and from the vibrations for pure formamide.

#### 2.4.4 Temperature Dependence of Hydroxyl and Formamide Bands and Correlation to Adsorption Geometries

Prior studies have shown that with decreasing temperature the OH stretching bands shift to higher frequencies, which have been assigned to increases in the inter-nuclear distances of the OH...O bonds of kaolinite upon cooling [68,78]. Our formamide-kaolinite experimental spectra are comparable with our experimental bare kaolinite in the regions of the inner surface OH stretches as a function of temperature. Compare Figures 2.5 and 2.6. The kaolinite deformation OH bending modes and Si-O and Si-O-Si modes do not significantly shift with temperature after adsorption of formamide, similar to bare kaolinite. Also similar to bare kaolinite, the Al-OH bending mode ( $\sim 800\text{ cm}^{-1}$ ) splits at 110 and 67 K compared to 300 K. This split may indicate that the inner surface hydroxyls attached to Al may undergo a surface reconstruction, i.e., the kaolinite layers move upon cooling which could allow formamide to physisorb on the surface at low temperature [66,67]. This has been suggested by Frost et al. as an explanation of Raman kaolinite band shifts after cooling to 77 K [66,67] and by Johnston et al. for the kaolinite OH IR vibrational shifts with temperature [68].

IR vibrations expected at  $3336$  and  $3466\text{ cm}^{-1}$  representing the two types of hydrogen bonds between the siloxane layer of kaolinite and the NH group of formamide [82] are not seen in these experiments. Even in the pre-mixed formamide-kaolinite slurry, the bands at  $3336$  and  $3466\text{ cm}^{-1}$  do not appear, indicating that they may be Raman-active and not IR-active for adsorbed formamide. On the other hand, despite the fact that calculated spectra are obtained using the cluster model of kaolinite, good agreement of the theoretical frequencies for inner and inner surface hydroxyl groups of the

formamide-kaolinite complex with prior experimental values [82] is revealed. An example of such agreement is a band at  $3473\text{ cm}^{-1}$  for the K(o)-FA complex which is attributed to a stretching vibration of the OH group forming a hydrogen bond with the nitrogen atom of formamide. This theoretical value is less than  $10\text{ cm}^{-1}$  different from the previously mentioned band observed with DRIFT spectroscopy at ( $3466\text{ cm}^{-1}$ ) [82].

When formamide is dosed at 67-90 K, many formamide vibrations are weak, broad or not present. The strong C=O stretch ( $1682\text{ cm}^{-1}$ ) shown in Figure 2.7 is visible but broad ( $75\text{ cm}^{-1}$ ), and it is shifted compared to the peak at 100-110 K (by  $19\text{ cm}^{-1}$ ). For temperatures as low as 67-90 K, broadening is not usually expected. However, prior work using DRIFT spectroscopy proposes that a peak at  $1667\text{ cm}^{-1}$  is C=O hydrogen bonded to kaolinite's inner surface hydroxyl [82]. To understand what may be causing the broadened C=O stretch, we compared the 67-90 K spectra to the spectrum of a pre-mixed formamide-kaolinite slurry, shown in Figures 2.7(b) and 2.8(b). We assume that the pre-mixed formamide-kaolinite slurry has some hydrogen bonding between formamide and kaolinite since it was mixed thoroughly prior to deposition on the sample holder. As seen in Figure 2.7(b), the C=O stretch for the slurry is at  $1667\text{ cm}^{-1}$  with a slight shoulder at  $1685\text{ cm}^{-1}$ . We interpret the peak at  $1667\text{ cm}^{-1}$  as hydrogen bonding between the C=O of formamide and the Al-OH, since it compares well with the assignment in prior DRIFTS work [82]. Because the C=O stretch in our 67-90 K experiments matches this peak within  $15\text{ cm}^{-1}$ , we also interpret this as hydrogen bonding between the C=O of formamide and the Al-OH in our low temperature (67-90 K) formamide adsorption experiments. Therefore, we suggest that the experimental peaks can be more likely assigned to the adsorption of formamide on the octahedral surface of kaolinite.

Previously published experimental studies [104,105] have also shown that formamide and other amides are adsorbed onto the kaolinite surfaces by hydrogen bonding to the inner surface hydroxyl groups. The theoretical IR spectra results and adsorption energy values for the K(o)-FA and K(t)-FA complexes confirm that the octahedral surface of kaolinite is the most favorable adsorption face when interacting with formamide.

The broadening of the C=O stretch at low temperatures may be due to combination with new unresolved bands, similar to broadening of NH stretches for urea-intercalated kaolinite at 77 K [106]. In addition, the lack of the NH<sub>2</sub> stretches and CH stretching mode in the 67-90 K experiments (see Table 2.4; Figure 2.8) also compares well to the pre-mixed slurry (Figure 2.8(b)) spectral features, and may be due to a competition and mixing between formamide-formamide and formamide-kaolinite interactions under these low-temperature conditions, which is consistent with the temperature-dependent kaolinite OH features [66,67,98,99] (shown in Figure 2.6).

Formamide was then dosed purposefully onto the pre-mixed formamide-kaolinite slurry for additional comparison. The relevant formamide features are shown in Figures 2.7(a) and 2.8(a). An additional sharp C=O stretch appears at 1701 cm<sup>-1</sup> and matches the 100-110 K C=O bands well. *Ab initio* calculations and matrix isolation experiments performed by Mardyukov et al. [107] have reported bands near 1700 cm<sup>-1</sup> as C=O in formamide dimers. In addition, the peaks at 1391 cm<sup>-1</sup> (CH sci.) and 1329 cm<sup>-1</sup> (C-N str.) sharpen similarly to the 100-110 K formamide-adsorbed data. Also, shown in Figure 2.8(a), the NH and CH stretches become distinct, similarly to the 100-110 K data. One of the possible explanations for these similarities is that formamide-formamide ice interactions/dimers are dominant (these vibrations also have stronger oscillator strengths)

at 100-110 K even at low coverages, although some hydrogen bonding may still be occurring. The 100-110 K temperature may allow more freedom of motion while formamide is adsorbed on kaolinite. In addition, at 100-110 K, the kaolinite OH...O distances likely change compared to 67-90 K, possibly affecting formamide-kaolinite binding even at low coverages [66-68,99].

Experiments at higher doses (250 L, not shown) were also performed at low temperature (67-90 K), and all the formamide vibrations became much stronger. At the higher doses, formamide condenses on itself as porous ice layers, and this coupling could be competitive with binding on kaolinite. In order to better understand the coupling, interactions of two formamide molecules were calculated by our collaborators. In the most stable system, formamide molecules bind with each other through two N-H...O-H bonds formed between the molecular amide group and carbonyl oxygen atom. The interaction energy (calculated at the same level of theory as for all of the adsorption systems explained here [56] and in the companion theory paper) [57] of the most stable formamide-formamide system is -14.6 kcal/mol. This energy is comparable to the binding energy of formamide with the octahedral and tetrahedral non-hydrated surface of kaolinite (-14.8 and -13.7 kcal/mol, see companion theory paper [57]). Formamide-formamide interactions are indeed very competitive with the formamide-kaolinite interaction, and the favorable formamide-formamide energetics may also be one reason why at increased dosing temperatures (100-110 K), the formamide molecules prefer to bind with each other primarily as dimers than to interact with the surface.

### 2.4.5 Temperature Programmed Desorption Analysis

The Redhead peak maximum method [54] was used to extract the activation energies of desorption ( $E_{act}$ ) from the TPD experiments, using the formula

$$E_{act} = RT_m \left[ \ln \left( \frac{\nu T_m}{b} \right) - 3.46 \right],$$

where  $R$  is the Boltzmann constant,  $\nu$  is the frequency factor typically employed ( $10^{13} \text{ s}^{-1}$ ),  $T_m$  is the peak maximum, and  $b$  is the heating rate (0.5 K/s). The mean values were calculated from several low coverage and low temperature TPD experiments.

The formamide desorption for all experiments performed were similar with no major differences in peak maximum (range of 174-188 K) or calculated activation energy (range of 11.1 to 12.0 kcal/mol). We can conclude from the relatively low binding energy that there is an interaction between formamide and kaolinite representing hydrogen bonding/strong physisorption.

It has been reported that, on a Ni(111) surface, formamide multilayers (third layer and above) desorb at ~160 K, while the second layer desorbs at ~170 K, and the first layer of formamide molecules desorbs near ~190 K [108]. The peak maximum for desorption in our TPD experiments was at ~183 K. Thus, our TPD results also signify that we are probing the first to second layer of formamide molecules on the powder with doses of 5-50 L.

### 2.4.6 Comparison of Binding Energies to Theory

For all experiments at low coverages (5-50 L) and at sample temperatures between 67 and 110 K, the mean  $E_{act}$  was  $11.7 \pm 0.24$  kcal/mol ( $0.51 \pm 0.01$  eV) at a mean desorption peak maximum temperature of 183 K. This value is very close to the energies of adsorption calculated in the companion theoretical paper [57] for formamide

adsorption on the octahedral and tetrahedral surface of kaolinite (-14.8 and -13.7 kcal/mol, respectively).

#### **2.4.7 Discussion of Binding and Comparison of Theoretically Optimized Structures of Formamide on Kaolinite**

The adsorption process of formamide on octahedral and tetrahedral surfaces of kaolinite is discussed in detail in the companion paper [57]. Therefore, here I will only briefly mention the main differences in intermolecular binding of the K(o)-FA and K(t)-FA adsorption complexes, as discussed by our collaborators [57]. In the K(o)-FA system, formamide binds with the surface through the formation of four hydrogen bonds formed between the formamide oxygen atom and  $\text{NH}_2$  group and four different surface hydroxyl groups (see Figure 2.3(a), structure adopted from companion paper [57]). In K(t)-FA, adsorption occurs due to formation of three hydrogen bonds between the formamide molecule and siloxane sheet of kaolinite (see Figure 2.3(b), structure adopted from companion paper [57]). The adsorption with the octahedral site was found to be stronger than with the tetrahedral sheet as it is demonstrated by adsorption energies of K(o)-FA (-14.8 kcal/mol) and K(t)-FA (-13.7 kcal/mol). As mentioned in Section 2.4.4, our experimental results also suggest that adsorption on the octahedral site is preferential.

## 2.5 Conclusions

The experimental IR spectra of formamide interacting with the surface of kaolinite have been examined as a function of temperature, and results were compared with calculated IR spectra obtained from our theoretical collaborators. Reasonable agreement between experiment and theory has been found with formamide as well as with the formamide-kaolinite complexes. Comparison of experimental and theoretical IR spectra for formamide interacting with kaolinite showed good agreement (with exception of the  $\text{NH}_2$  stretching vibrations of formamide), and only small shifts (less than  $20\text{ cm}^{-1}$ ) occur for most of the inherent frequencies (among them are the  $\text{C}=\text{O}$  stretching and  $\text{CH}$  scissor modes). Under ultra-high vacuum conditions, the experiments show changes in the kaolinite inner surface hydroxyl bands due to temperature. This likely has an effect on how formamide binds at different temperatures due to kaolinite surface reconstructions. In the theoretical IR spectra, the existence of peaks attributed to the stretching vibrations of inner surface OH groups of the octahedral surface of kaolinite involved in the hydrogen bonding with formamide carbonyl ( $3604$  and  $3504\text{ cm}^{-1}$ ) and with the  $\text{NH}_2$  group of formamide ( $3554$  and  $3473\text{ cm}^{-1}$ ) were revealed. However, the calculated bands assigned to the OH stretching vibrations of OH groups forming the hydrogen bonds with formamide were not observed experimentally. The preferential availability of adsorption sites could increase due to changes in some inter-nuclear distances between the  $\text{OH}\dots\text{O}'\text{s}$  of kaolinite at low temperatures [68]. Indeed, IR spectra at  $67\text{-}90\text{ K}$  suggests adsorption between formamide's  $\text{C}=\text{O}$  and kaolinite's octahedral face, which is consistent with the theoretical calculations. Thus, this study shows evidence for preferential binding of formamide to the octahedral site of kaolinite. In addition, several of the formamide

vibrational bands (C=O, CH, C-N, NH) shift, become sharp or visible with increasing temperature near 100-110 K, which may be related to restructuring of formamide on the kaolinite with increasing temperature and/or dominant formamide-formamide dimer interactions. Experimental TPD analysis yielded a mean activation energy of desorption of  $11.7 \pm 0.24$  kcal/mol. This value agrees well with the calculated adsorption energies of formamide adsorbed on the non-hydrated octahedral (-14.8 kcal/mol) and tetrahedral (-13.7 kcal/mol) kaolinite surfaces.

## CHAPTER III

### THERMAL AND RADIATION PROCESSING OF FORMAMIDE ICES ON INTERSTELLAR SILICATE GRAIN ANALOG

#### 3.1 Introduction

Formamide (HCONH<sub>2</sub>) has been tentatively identified in interstellar ices (NGC 7538 IRS9 and W33A) [62] and has been detected toward the galactic center sources of Sgr A and Sgr B [109]. In 2006, Hollis et al. reported two gas-phase transitions of formamide toward Sagittarius B2(N) [110], a giant molecular cloud with temperatures as low as 40 K in the surrounding envelope and up to 300 K in the dense star-forming regions [111]. Formamide was also detected from the Hale-Bopp comet (C/1995 O1) in an abundance of 0.01-0.02% compared to water with an out-gassing production rate of  $9\text{-}23 \times 10^{26}$  molecules s<sup>-1</sup> [112]. That report also suggested a link between cometary and interstellar materials. The amide family gained recent attention when the identification of both acetamide and formamide toward Sgr B2(N) was reported using the Submillimeter Telescope (SMT) and the Arizona Radio Observatory [9]. For formamide, 79 individual transitions were identified, and column densities for the cold component ( $1.6 \pm 0.7 \times 10^{14}$  cm<sup>-2</sup>) and warm component ( $4.0 \pm 1.2 \times 10^{14}$  cm<sup>-2</sup>) were reported. Fractional abundances for the cold and warm components were also reported to be  $5.3 \times 10^{-11}$  and  $1.3 \times 10^{-10}$ , respectively, compared to H<sub>2</sub> [9].

The presence of formamide in interstellar regions has been partially explained by several laboratory experiments. For example, exposure of several known interstellar ices

(H<sub>2</sub>O, CH<sub>3</sub>OH, CO, and NH<sub>3</sub>) to UV irradiation showed the production of more complex molecules, including formamide, upon warm-up [113]. Another study reported formamide formation upon UV and thermal processing of methanol-containing ices [114]. Chen et al. reported formamide features in low temperature ice mixtures composed of H<sub>2</sub>O, CO<sub>2</sub>, and NH<sub>3</sub> [32]. More recently, Jones et al. reported formamide formation from mixed CO:NH<sub>3</sub> ices upon high energy electron bombardment [112], and Gerakines et al. reported the production of formamide from proton irradiation of HCN mixed ices [115].

Very few studies have examined formamide's radiation chemistry in the condensed phase (ice). Proton (200 keV) bombardment of formamide ice at 20 K has been published by Brucato et al. [24,116]. The irradiation products included CO, CO<sub>2</sub>, N<sub>2</sub>O, HNCO, and NH<sub>4</sub><sup>+</sup>OCN<sup>-</sup>. Some of these products are stable up to 300 K [24]. In another publication, the effect of a cosmic dust analog surface (MgFeSiO<sub>4</sub>) on product synthesis from formamide was studied, indicating that formation of NH<sub>3</sub> and CN<sup>-</sup> is inhibited by the surface while changes occurred in the relative abundances of the other products [116].

Formamide's decomposition channels have been studied theoretically [61] and experimentally [117-122]. A recent theoretical study of formamide decomposition in the gas phase [61] reported that H<sub>2</sub>O loss (dehydration of formamide to HCN + H<sub>2</sub>O) was the most favorable channel and occurred through a multistep pathway involving a formimidic acid (H-N=C(H)-OH) intermediate. In addition, CO elimination (decarboxylation to CO + NH<sub>3</sub>) is the second most kinetically favored pathway. Finally, H<sub>2</sub> loss (dehydrogenation to H<sub>2</sub> + HNCO) was found to occur primarily through a one-step

process, although a two-step mechanism is competitive. Recent formamide gas-phase laser spark experiments indicate the formation of HCN, CO, NH<sub>3</sub>, CO<sub>2</sub>, N<sub>2</sub>O, hydroxylamine, and methanol from formamide [117].

Several studies have also focused on the photo-decomposition of formamide in matrices, leading to HNCO + H<sub>2</sub> and NH<sub>3</sub> + CO [118] or dehydration products (HCN + H<sub>2</sub>O, HNC + H<sub>2</sub>O) [119,120]. Other studies include liquid formamide irradiation by 200 nm femtosecond pulses [121], and irradiation of ~300 K formamide by synchrotron radiation at 10-20 eV [122]. The latter study demonstrated formation of the HNCO<sup>+</sup> ion from two pathways, one involving H<sub>2</sub> loss and the other involving H + H [122]. That work also reports the gas-phase ionization energy (IE or IP) of formamide as 10.220 +/- 0.005 eV, which may result in a negligible ionization of formamide in interstellar regions where hydrogen Lyman- $\alpha$  emission is prevalent [122]. However, a recent DFT, *ab initio* HF, and Møller–Plesset perturbational theory (MP) study has calculated formamide's adiabatic and vertical ionization potentials (AIP and VIP, respectively) to be ~10 eV for gas-phase and ~8 eV for aqueous solution [123]. This suggests that the IP could be lowered in a condensed-phase ice.

A recent study reported formamide's thermal decomposition from 300 to 850 °C, indicating that a polymer called poly(hydrogen cyanide) or PHC could be responsible for the emission of HCN or CN radicals from cometary emissions [124,125]. However, detailed laboratory ice studies of formamide's decomposition and chemical transformation need to be carried out in the condensed phase. In addition, a more thorough study of formamide ice is warranted when considering a eutectic frozen primitive Earth scenario where HCN would have been concentrated sufficiently to

polymerize [126]. In addition, though formamide's abundance is small relative to the main interstellar ice components ( $\text{H}_2\text{O}$ ,  $\text{CO}$ , etc.), its identification in astrophysical environments, as well as its possible prebiotic function require more detailed laboratory studies of formamide ices under conditions that mimic interstellar/cometary sources. In order to mimic regions where UV photon flux dominates, such as cold diffuse clouds [29], simulated laboratory Lyman- $\alpha$  experiments are warranted to determine formamide's stability and expected relative product ratios.

In this research, thermal and radiation experiments of formamide ice on  $\text{SiO}_2$  nanoparticles under ultra-high vacuum (UHV) conditions over a temperature range of 70 to 465 K are reported. The  $\text{SiO}_2$  surface is used as a model for interstellar silicate dust grains [33], and the temperature range was chosen to mimic warming in interstellar sources where formamide has been detected [111]. In addition, the temperature range overlaps what is expected to be found on early Earth [126]. Mid-IR spectra of formamide ( $\text{HCONH}_2$ ,  $\text{DCONH}_2$  and  $\text{HCOND}_2$ ) ices were taken upon warm-up from 70 K to 465 K. Product analysis after Lyman- $\alpha$  irradiation of pure  $\text{HCONH}_2$  was performed with transmission FT-IR spectroscopy, and TPD measurements. Lyman- $\alpha$  and electron beam irradiation of mixed  $\text{HCONH}_2:\text{H}_2\text{O}$  ices were also performed for comparison.

### 3.2 Experimental Details

The stainless steel UHV chamber (base pressure  $\sim 1 \times 10^{-10}$  Torr) has been described previously in Chapter 2; however, details relevant to this study will be briefly mentioned. The UHV chamber is coupled to a Bruker Equinox 55 FT-IR spectrometer with an external HgCdTe LN<sub>2</sub>-cooled detector for transmission FT-IR experiments of the sample under vacuum. For all experiments described here, FT-IR spectra were recorded in the range of 4000-400 cm<sup>-1</sup> with 2 cm<sup>-1</sup> resolution averaged over 250 scans for both the background and sample scans using OPUS Bruker software. All absorption spectra shown in this study were produced via subtracting out the spectra of the SiO<sub>2</sub> powder at 70 K via the Beer-Lambert law ( $A = -\log(I/I_0)$ ), where  $I$  is the single channel spectrum taken after formamide adsorption, and  $I_0$  is the single channel spectrum taken of the bare SiO<sub>2</sub> powder at 70 K. This subtraction results in the removal of SiO<sub>2</sub> bands from the spectra except for those that change during the experiment. Positive peaks indicate an increase in the IR absorbance intensities, and negative peaks indicate a decrease in intensity. For the irradiation experiments,  $I_0$  is the single channel spectrum taken of the formamide deposited on SiO<sub>2</sub> powder before irradiation began (time = 0). This subtraction (absorbance difference) allowed easy identification of irradiation products. Smoothing of the spectra was done with the OPUS Bruker software; however, care was taken to ensure no loss of spectral features.

The UHV chamber is also equipped with a quadrupole mass spectrometer (QMS) to perform simultaneous TPD measurements using custom LabView software that controls the QMS and maintains a linear temperature ramp (0.5 K/s) by providing a feedback loop to the computer and heater power supply.

The sample holder has been described in Chapter 2 (Figure 2.2). Briefly, a 1" × 1" tungsten (W) wire mesh, purchased from Unique Wire Weaving Company, Inc., was used to mount the silicon oxide (SiO<sub>2</sub>) nanopowder sample in the UHV chamber, which was used as an interstellar grain analog. The tungsten mesh has a 74.8% open area, with 0.0058" size openings between each plain weave, 150 wires per inch, and a wire diameter of 0.0009". The white, amorphous, porous silicon oxide (SiO<sub>2</sub>, 99.5%) nanopowder (BET surface area = 640 m<sup>2</sup>/g) was purchased from US Research Nanomaterials, Inc., with a reported particle size of 15-20 nm (determined via TEM by the company). It has been spectroscopically determined that this nanopowder is composed of SiO<sub>2</sub> and Si-OH groups, and the hydroxyl content was >45%. To produce the SiO<sub>2</sub> coated substrate, the tungsten mesh was dipped in a mixture of ~0.48 g SiO<sub>2</sub> nanopowder to 2 mL nanopure H<sub>2</sub>O. The dip-coated mesh was baked in an oven at 110 °C overnight to remove the H<sub>2</sub>O from the SiO<sub>2</sub>. The resulting weight of the SiO<sub>2</sub> on the mesh was 0.0165 g, after baking. The silicon oxide-coated tungsten mesh sample was then spot-welded to two tantalum horizontal strips and attached to the sample holder (described previously in Chapter 2). After affixing the silicon oxide-coated mesh to the sample holder, the chamber was sealed, pumped down, and baked for 24-48 hours at 100 °C to remove any contaminants from the chamber and sample. Effective cooling to 70 K and heating to 900 K is possible with this sample, as measured by attaching a K-type thermocouple directly to the tungsten grid.

Formamide (HCONH<sub>2</sub>, ≥99.5%) was purchased from Sigma-Aldrich, and isotopic labeled formamide samples (DCONH<sub>2</sub> and HCOND<sub>2</sub>) were purchased from C/D/N Isotopes, Inc. with a purity of 99.5% D and 99.9% D, respectively. The dosing manifold

is equipped with a turbo-molecular pump and dry backing pump to effectively evacuate any contaminants before each experiment. Formamide liquid attached to the manifold was freeze-pump-thawed prior to dosing, and formamide was dosed into the chamber and onto the cold SiO<sub>2</sub> substrate via a precision leak valve. An ion gauge located near the sample monitored the chamber pressure during dosing to maintain a controlled pressure ( $\sim 1 \times 10^{-6}$  Torr) for a specific time. Doses of 25 Langmuir (L) up to  $\sim 1100$  L were employed. Formamide's arrival rate was calculated from the standard kinetic theory formula [51] to be  $3.02 \times 10^{14}$  molecules  $\text{cm}^{-2}\text{s}^{-1}$ , and assuming unity sticking probability at 70 K and the density of formamide ice ( $0.937 \text{ g cm}^{-3}$ ) [24] we estimate [51] that our maximum ice thickness is  $\sim 0.80$  nm per ML (monolayer). Though the surface roughness and high surface area precludes a uniform thickness, an upper limit of the formamide ice thickness can be estimated to be  $\sim 880$  nm for an 1100 L dose.

Some experiments involved co-dosing distilled H<sub>2</sub>O with HCONH<sub>2</sub> in either 0.75:1 or 2:1 mixtures, respectively. These were co-dosed with separate leak valves to prevent cross-contamination. For the 0.75:1 mixed experiments, 825 L H<sub>2</sub>O to 1100 L HCONH<sub>2</sub> were dosed, and for the 2:1 mixed experiments, 1100 L H<sub>2</sub>O to 550 L HCONH<sub>2</sub> were dosed. Doses were calculated based on pressure.

To simulate radiation emitted from star-forming regions, we have chosen to use a hydrogen discharge plasma flow lamp. Specifically, the 121.6 nm irradiation studies were performed using a Lyman- $\alpha$  lamp (resonance line source), purchased from Ophos Instruments, Inc. and modified to be a hydrogen-flow lamp. A pre-mixed ultra-high purity gas mixture of helium (He), argon (Ar), and hydrogen (H<sub>2</sub>) at 80, 18, and 2%, respectively, flowed into the lamp at  $\sim 15$  sccm. The flow was controlled with a Matheson

Tri-Gas flow tube. The outlet side on the lamp was connected to a needle valve that was controlled to keep a pressure of 3.5 Torr in the lamp during operation [127]. The gas mixture, flow rate, and pressure were chosen based on prior work of Y. Benilan et al. [127], which reported that these conditions maximize the 121.6 nm line emission while diminishing the 160 nm H<sub>2</sub> emission [127]. In particular, adding ~20% Ar to the gas mixture is reported to increase (x2) the Lyman- $\alpha$  emission [127], while decreasing the H<sub>2</sub> emission bands. The lamp is coupled to the UHV chamber via a MgF<sub>2</sub> window sealed to the end of the lamp. The lamp faces normal to the rotatable-sample, with a working distance of ~15 cm from the sample. The lamp is excited using an Opthos microwave generator connected to a tunable RF cavity placed on the lamp between the gas inlet and gas outlet. Typical operation was at a discharge power of ~40-50 W, which gives a photon flux of  $\sim 1 \times 10^{15}$  photons s<sup>-1</sup> [127]. The Lyman- $\alpha$  photon flux at our 3.75 cm<sup>2</sup> sample is thus calculated to be  $\sim 2.7 \times 10^{14}$  photons s<sup>-1</sup> cm<sup>-2</sup>. When multiplied by the value for  $\langle E \rangle$  (energy) of 10.2 eV, this corresponds to a total energy flux of  $2.75 \times 10^{15}$  eV cm<sup>-2</sup> s<sup>-1</sup>. The total energy doses can then be calculated for the irradiation times employed, in units of eV cm<sup>-2</sup> [115].

The UHV chamber is also equipped with a pulsed, tunable electron gun that can emit 5-1000 eV electrons. Electron irradiation was performed as a comparison to Lyman- $\alpha$  irradiation. The e-gun is directed normal to the rotatable sample on the opposite side of the chamber as the Lyman- $\alpha$  lamp. The typical electron current density is  $\sim 10^{14}$  electrons cm<sup>-2</sup>s<sup>-1</sup> with a beam spot size of  $\sim 1.5$  mm. The sample position is imaged with a custom-built Labview program by measuring the current on the sample (with picoammeter) to determine the region to raster over the sample. The entire sample

area ( $3.75 \text{ cm}^2$ ) can be rastered with 1 keV electrons in ~5 minutes during irradiation experiments.

Typical experiments were carried out as follows. The  $\text{SiO}_2$  sample was heated to ~500 K prior to each experiment, and once the pressure had dropped ( $\sim 10^{-8}$  Torr), the sample was then cooled back to 70 K. A background FT-IR spectrum was obtained at 70 K of the bare  $\text{SiO}_2$  substrate prior to dosing formamide. Once dosed, an FT-IR spectrum was again obtained at 70 K. For the warm-up experiments, subsequent FT-IR spectra were taken as a function of increasing temperature. For Lyman- $\alpha$  experiments, ices were either held at 70 K or annealed to 165 K prior to beginning irradiation. The sample was rotated to face the lamp during irradiation experiments. Most Lyman- $\alpha$  irradiation experiments lasted ~5.5 hr, which we concluded was the minimum necessary time to obtain sufficient product formation and to limit significant background water dosing. Post-irradiation FT-IR and TPD measurements were also obtained as a function of increasing temperature. Mixed  $\text{H}_2\text{O}:\text{HCONH}_2$  70 K ices were also irradiated with Lyman- $\alpha$  for comparison to pure  $\text{HCONH}_2$  ices. For electron irradiation experiments, 1 hour of 1 keV electron irradiation was performed on 70 K ice that was either pure or mixed with  $\text{H}_2\text{O}$ . The sample was cleaned by flashing to ~500 K between experiments to sufficiently sublime all the formamide ice from the  $\text{SiO}_2$  substrate.

### 3.3 Thermal Processing of Pure Formamide Ices on SiO<sub>2</sub>

#### 3.3.1 Results

##### 3.3.1.1 IR Spectra of HCONH<sub>2</sub> Ice From 70 K to 465 K

IR peaks have been assigned based on prior HCONH<sub>2</sub>, DCONH<sub>2</sub>, and HCOND<sub>2</sub> gas-phase, liquid, and condensed-phase reports [95,128-134]. It is important to note here that the IR frequency changes are not due to temperature effects on the vibrations, since the spectra of the ices do not change reversibly at the different temperatures (see Section 3.3.1.5 for clarification). As shown in Figure 3.1, the main visible IR vibrations for HCONH<sub>2</sub> at 75 K include the asymmetric and symmetric NH<sub>2</sub> stretches (3317, 3163 cm<sup>-1</sup>), a C-H stretch (2885 cm<sup>-1</sup>), the strong C=O stretch (1693 cm<sup>-1</sup>), the weak and broad NH<sub>2</sub> bending mode (1633 cm<sup>-1</sup>), the C-H bending mode (1385 cm<sup>-1</sup>), and the C-N stretch (~1327 cm<sup>-1</sup>). Two weak, broad peaks at 682 and 630 cm<sup>-1</sup> represent NH<sub>2</sub> wagging and NH<sub>2</sub> torsion modes [133], respectively.

Upon warm-up to 165 K (Figures 3.1 and 3.4C), several IR bands sharpen including the NH<sub>2</sub> and C-H stretches, NH<sub>2</sub> (1643 cm<sup>-1</sup>) and C-H (1390 cm<sup>-1</sup>) bending modes, C-N stretch (1329 cm<sup>-1</sup>), and the NH<sub>2</sub> wagging and torsion modes at 652 and 631 cm<sup>-1</sup>, respectively. The sharpening of the bands at 652 and 631 cm<sup>-1</sup> is in contrast to a prior study in which the bands were sharper (and splitting) at lower temperature (108 K compared to 208 K) [130]. Another main change seen is the splitting and shifting of the C=O stretch and the appearance of a shoulder at 1750 cm<sup>-1</sup> upon warm-up.

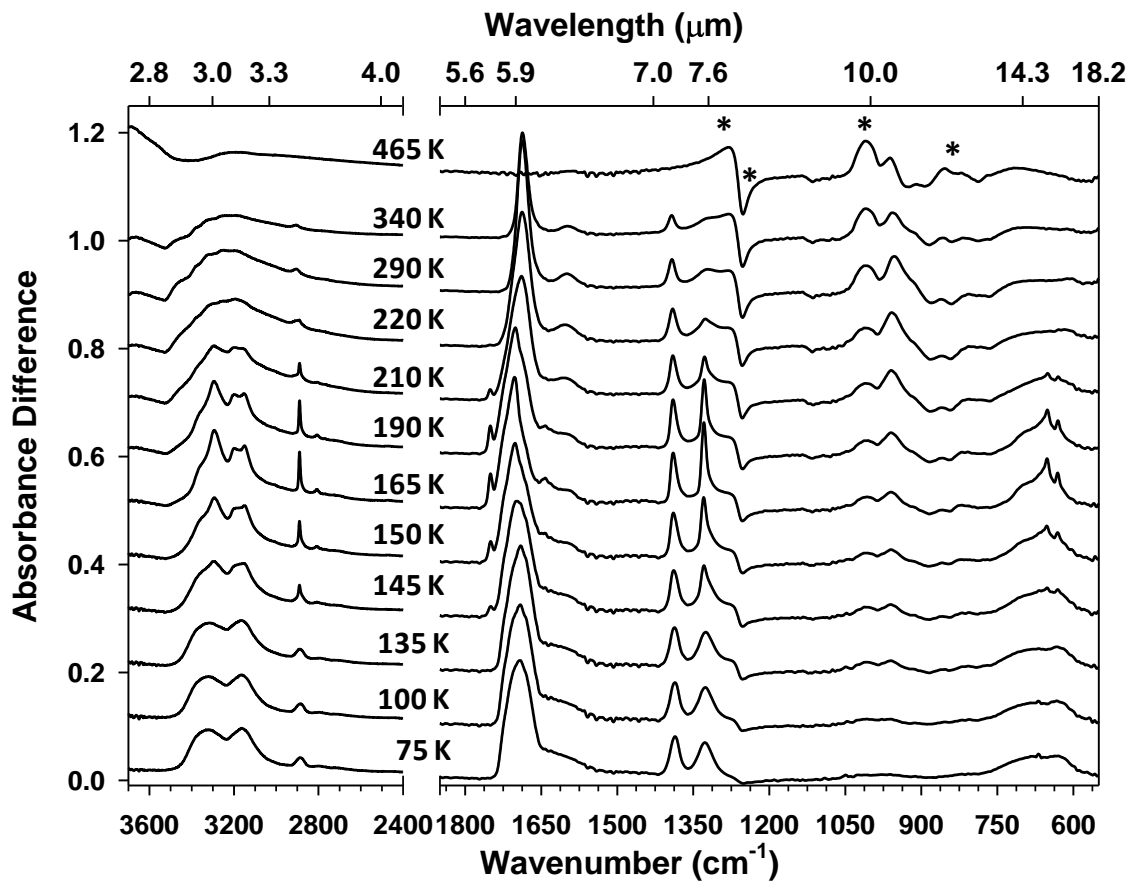


**Figure 3.1:** Infrared spectra during warm-up after deposition of 1100 L of HCONH<sub>2</sub> at 70 K. Changes in peaks with \* are due to temperature effects only.

### 3.3.1.2 IR Spectra of DCONH<sub>2</sub> Ice From 70 K to 465 K

IR features of DCONH<sub>2</sub> taken at 70 K are shown in Figure 3.2, and most of the vibrations occur at about the same frequencies as for HCONH<sub>2</sub>. Two exceptions that confirm isotope replacement include the C-D stretching mode, now visible at 2178 cm<sup>-1</sup>, that replaces the C-H stretch previously found at 2885 cm<sup>-1</sup>, and a decrease in intensity seen for the C-H bending mode at 1385 cm<sup>-1</sup>. The absolute intensity of the C-H bending mode for HCONH<sub>2</sub> at 75 K was 0.082, whereas for DCONH<sub>2</sub> the absolute intensity of this band has decreased to 0.023. These changes in the IR vibrations of DCONH<sub>2</sub> compared with HCONH<sub>2</sub> confirm isotopic substitution at the C-H position.

Upon warm-up to 165 K (Figures 3.2 and 3.4B), the main IR vibrational changes are similar to HCONH<sub>2</sub> mentioned above, further confirming the original assignments. For this isotope, the C-D stretch at 2178 cm<sup>-1</sup> becomes two sharp peaks at 2181 and 2160 cm<sup>-1</sup>. In addition, the splitting of the C=O stretch is confirmed by the appearance of now one sharp peak at 1738 cm<sup>-1</sup> representing C=O stretch (with D attached) and a much weaker peak at 1759 cm<sup>-1</sup> representing C=O stretch (with H attached). The weaker peak is likely due to H-D isotopic exchange upon warm-up. This small amount of exchange is further confirmed by the small presence of C-H stretches at 2894, 2889, and 2842 cm<sup>-1</sup>. A similar blue shift (frequency increase) is seen for the main C=O stretch, from 1687 cm<sup>-1</sup> at 70 K to 1692 cm<sup>-1</sup> at 165 K. However, for DCONH<sub>2</sub> two weak peaks arise that were not seen in HCONH<sub>2</sub>. These include a peak at 1172 cm<sup>-1</sup> that are tentatively identified as a C-N stretch (+ NHD rock – NCO bending mode) [128] and a peak at 992 cm<sup>-1</sup> (C-D wagging mode [134]) that is on the shoulder of the SiO<sub>2</sub> vibration at 1011 cm<sup>-1</sup>.

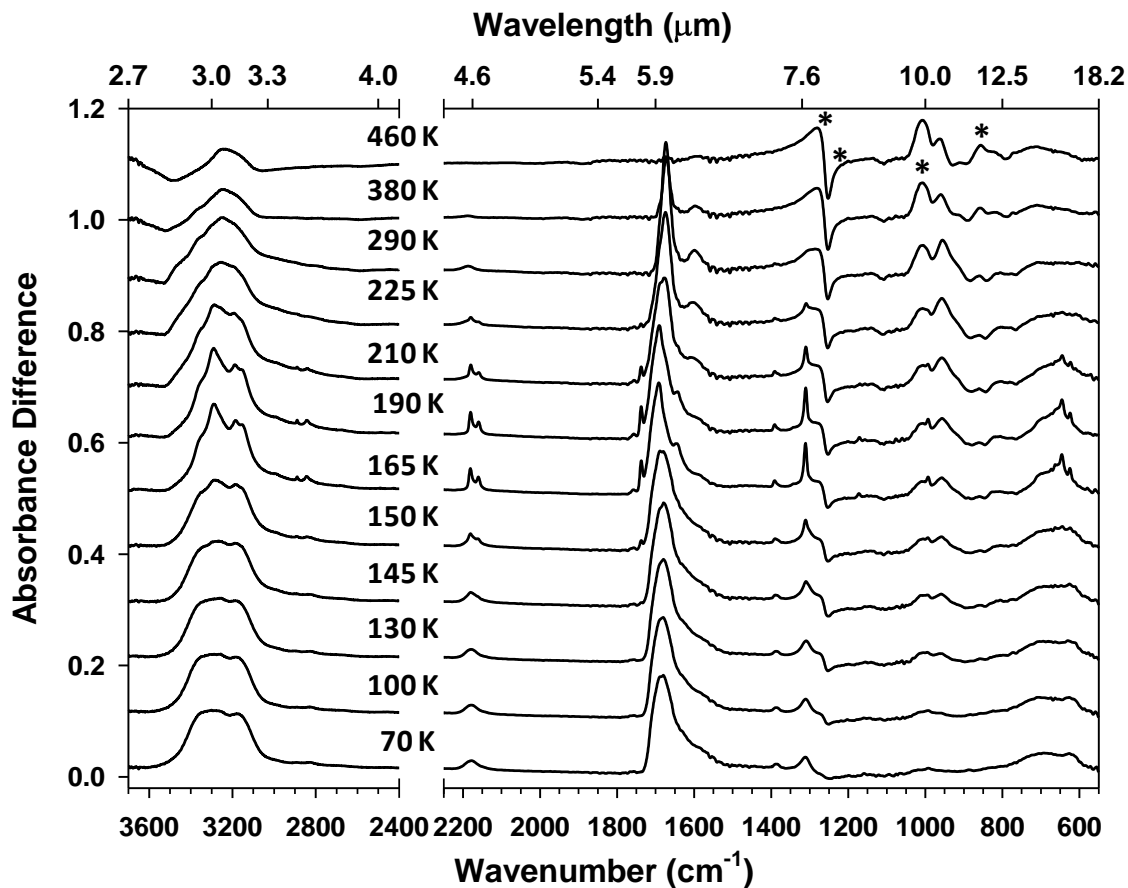


**Figure 3.2:** Infrared spectra during warm-up after deposition of 1100 L of  $\text{DCONH}_2$  at 70 K. Changes in peaks with \* are due to temperature effects only.

### 3.3.1.3 IR Spectra of $\text{HCOND}_2$ Ice From 70 K to 465 K

IR features of  $\text{HCOND}_2$  taken at 70 K are shown in Figure 3.3. Isotopic replacement is confirmed by the significant decrease in the  $\text{NH}_2$  stretching modes, which had an absolute intensity of  $\sim 0.096$  for  $\text{HCONH}_2$  and now only has an absolute intensity of  $\sim 0.039$ . In addition, new strong peaks representing the  $\text{ND}_2$  stretches are found at 2507 and 2352  $\text{cm}^{-1}$ . Finally, the broad weak bands previously found at 682 and 630  $\text{cm}^{-1}$  representing the  $\text{NH}_2$  wagging and torsion modes in  $\text{HCONH}_2$  are now almost non-existent due to the isotopic substitution in  $\text{HCOND}_2$ . Not only do the changes

confirm isotopic replacement in the N-H position, but also confirm the assignments given to our spectra of HCONH<sub>2</sub> ice.

Upon warm-up to 165 K (Figures 3.3 and 3.4A), similar changes occur compared to the two previous isotopes discussed. For this ice, sharpening of the ND<sub>2</sub> stretches occur giving bands at 2485, 2437, 2390, 2357, and 2340 cm<sup>-1</sup>. Compared to the sharpening seen in the NH<sub>2</sub> stretches for the previous two ices, here we see several additional bands. The bands at 2390, 2357, and 2340 cm<sup>-1</sup> overlap with background CO<sub>2</sub>; thus, influence from CO<sub>2</sub> may contribute. However, the sharpness of the band at 2340 cm<sup>-1</sup> is difficult to explain as simply CO<sub>2</sub>; thus it must at least be partially due to the ND<sub>2</sub> stretching modes. A weak peak at 2281 cm<sup>-1</sup> is tentatively assigned [128] to ND<sub>2</sub> bending because there is no additional or shifted ND<sub>2</sub> bending vibration seen near the weak NH<sub>2</sub> bending mode at 1646 cm<sup>-1</sup>, which is only weakly visible due to isotopic exchanging. In addition, due to minor N-D to N-H isotopic exchange, weak peaks at 3277 and 3229 cm<sup>-1</sup> represent the NH<sub>2</sub> stretching modes. Another weak band at 2689 cm<sup>-1</sup> is visible, and we tentatively assign this as a C-H stretch. In this ice, we again see the new C=O stretch (with H attached to carbon, 1733 cm<sup>-1</sup>), but we do not see the deuterated companion peak (C=O with D attached) as seen in the DCONH<sub>2</sub> ice. Again, the main C=O stretch blue shifts from 1665 cm<sup>-1</sup> at 70 K to 1674 cm<sup>-1</sup> at 165 K. Since this peak shifts comparably in all three experiments, its frequency appears very sensitive to differences that occur in the formamide ice geometry (discussed further in Sections 3.3.1.6 and 3.3.2.1). A weak peak at 942 cm<sup>-1</sup> is assigned to the ND<sub>2</sub> rocking mode (-CN stretch), and it overlaps with the SiO<sub>2</sub> vibration at 958 cm<sup>-1</sup>. Finally, both the NH<sub>2</sub> wagging and torsion modes are much weaker and are now shifted to 634 and 569 cm<sup>-1</sup>, respectively, compared to the other

isotopes at 165 K. The shifting is evidence for assignment to ND<sub>2</sub> wagging and torsion modes at these frequencies. Therefore, this further confirms the assignments of these features in all the formamide isotopes.

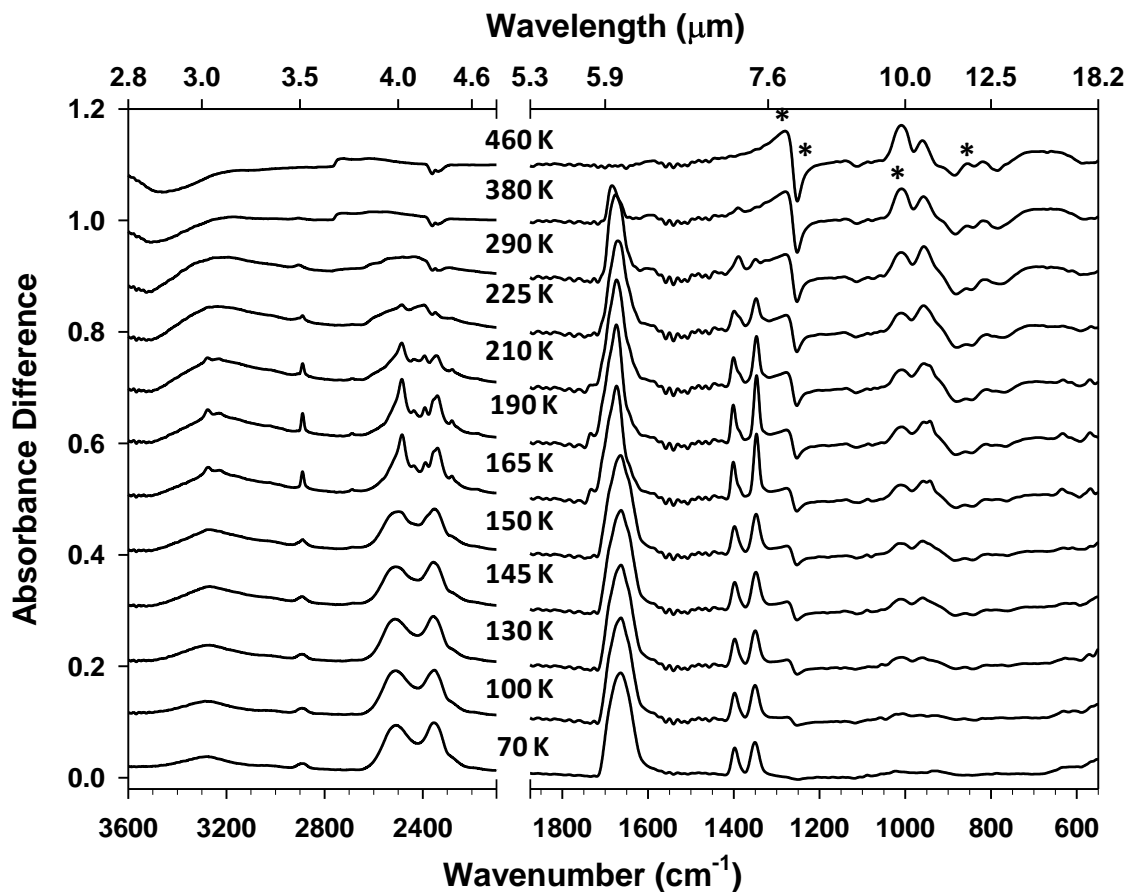


**Figure 3.3:** Infrared spectra during warm-up after deposition of 1100 L of HCOND<sub>2</sub> at 70 K. Changes in peaks with \* are due to temperature effects only.

#### 3.3.1.4 Comparison of IR Spectra of Formamide Ices Warmed to 165 K

It is immediately apparent from Figures 3.1-3.3 that all three isotopes have major changes occurring in their IR features starting at ~145 K, with the changes most evident near 165-190 K in all three isotopes. Figure 3.4 presents a direct comparison of the mid-IR spectra taken of the three formamide ices upon warm-up to 165 K, where the sharpest features are apparent. Table 3.1 also gives a corresponding list of the band positions for the IR spectra taken at 165 K. These changes include sharpening of the respective formamide vibrations already present, as well as appearance of a few new distinct features. The sharpened IR features seen at 165 K begin to reduce from their intensities notably at ~210 K, when some of the formamide begins to desorb (seen also in TPD below, Section 3.3.1.7). The IR features above 210 K, although broad, are not identical to those seen at 70 K for any of the three ices.

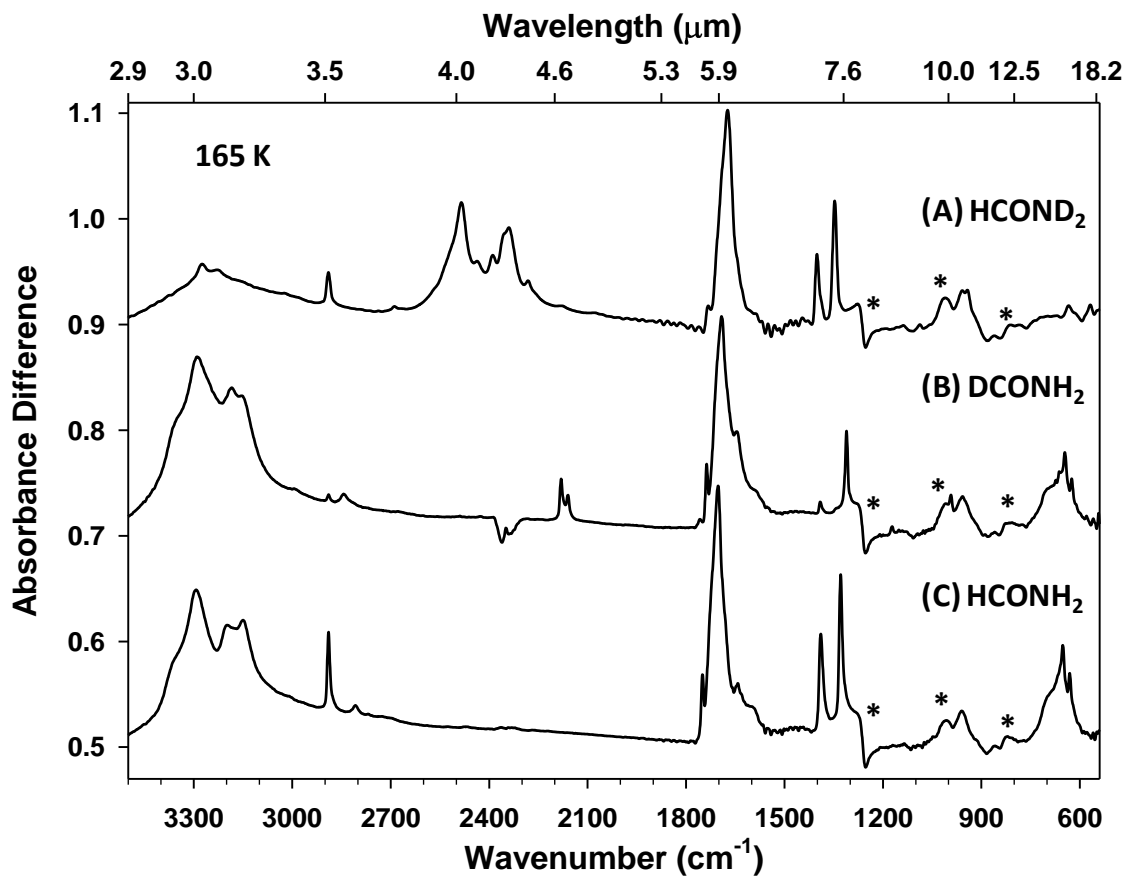


**Figure 3.4:** Comparison of infrared spectra at 165 K during warm-up after deposition at 70 K of 1100 L of (A) HCOND<sub>2</sub>, (B) DCONH<sub>2</sub>, (C) HCONH<sub>2</sub>. Changes in peaks with \* are due to temperature effects only.

**Table 3.1:** Infrared vibrational frequencies for formamide isotopes (1100 L dosed at 70 K) after warm-up to 165 K. Corresponding spectra are shown in Figure 3.4.

Assignment @ 165 K	HCONH <sub>2</sub>	DCONH <sub>2</sub>	HCOND <sub>2</sub>
NH <sub>2</sub> asym stretch	3292	3290	3277
NH <sub>2</sub> sym stretches	3199, 3150	3185, 3153	3229
CH stretches	2890, 2808	2894 (w), 2889, 2842	2890,2689 (vw)
ND <sub>2</sub> asym stretches			2485, 2437
ND <sub>2</sub> sym stretches			2390, 2357, 2340
ND <sub>2</sub> bend			2281
CD stretches	-	2181, 2160	
C=O stretch	1750	1759 (w), 1738	1733
C=O stretch	1703	1692	1674
NH <sub>2</sub> bend	1643	1645	1646 (vw)
CH bend ( – C=O stretch)	1390	1392 (w)	1401, 1390 (sh)
CN stretch ( + NH <sub>2</sub> [or ND <sub>2</sub> ] rock – NCO bend)	1329	1311	1347, 1350 (sh)
CN stretch ( + NHD rock – NCO bend)	-	1172 (?)	-
Si-O-Si phonon modes [135]	1007	1011 (w)	1086 (w), 1010
CD wagging	-	992	-
Si-OH stretching	960	957	958
ND <sub>2</sub> rock ( – CN stretch)			942
NH <sub>2</sub> wagging ( + NH <sub>2</sub> torsion)	652	646	634 (for ND <sub>2</sub> )
NH <sub>2</sub> torsion ( – NH <sub>2</sub> wagging)	631	625	569 (for ND <sub>2</sub> )

w=weak; vw=very weak; sh=shoulder on main peak

### 3.3.1.5 Experiments to Rule Out Temperature Effects on IR Bands

A brief mention of temperature effects on IR vibrations is warranted. Temperature effects are defined here as thermal influences only on the IR band transitions, not due to changes in the structure of the molecule itself. One example of temperature effects is sharpening of IR bands upon lowering the temperature [37], but these effects are reversible if the temperature is changed. To distinguish between this effect and a true structural change in the ice, several experiments were examined. For example, annealing a formamide ice to 165 K, taking a spectrum, and then cooling to 70 K and subsequently taking another IR spectrum was performed. See Figure 3.5. After cool down to 70 K, the IR spectrum still held the same new and sharpened vibrational features seen at 165 K. Similar experiments were done for 210 K, 290 K, and 380 K annealing temperatures (not shown). Thus, the IR band changes with temperature have been found to be irreversible in this study. IR features seen upon warm-up were still observed upon cooling to 70 K for all the temperatures tested, confirming that a true structural modification of formamide ice occurs upon warm-up, with formamide locked into new configurations when cooled back to 70 K.

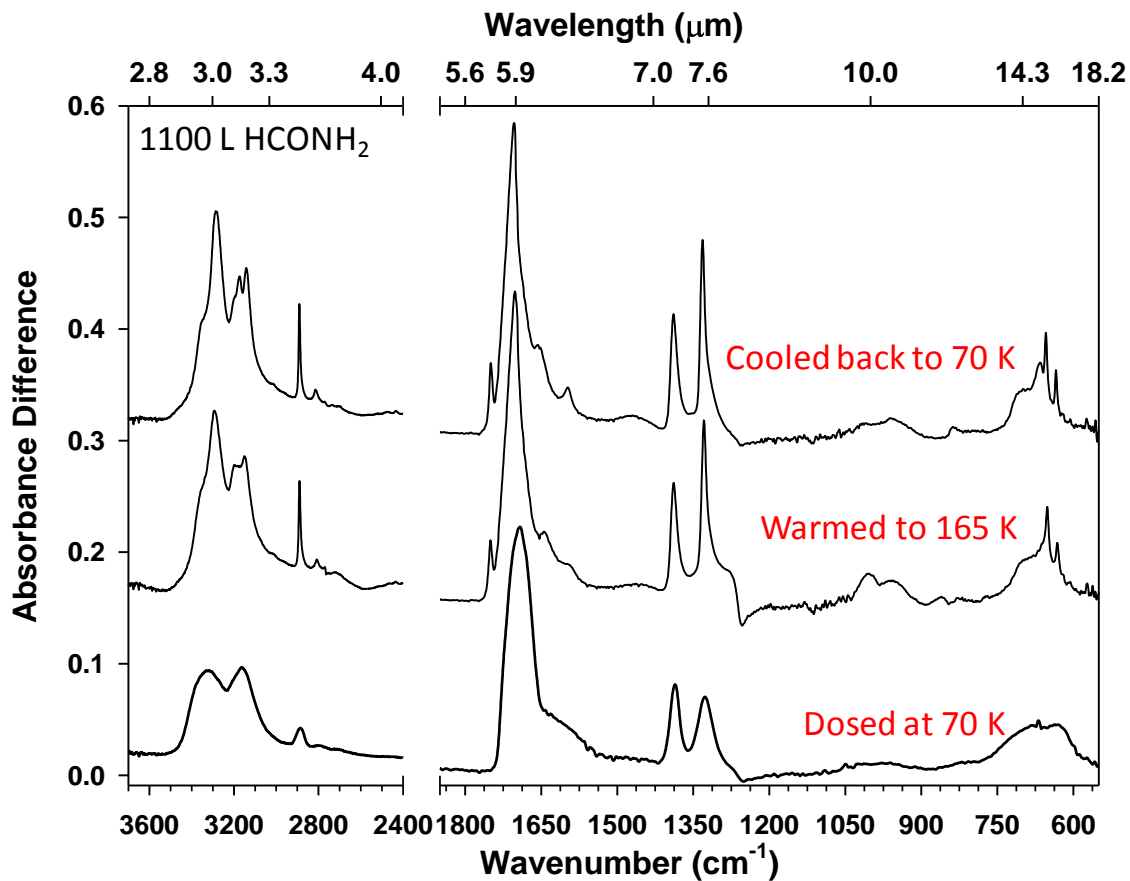


**Figure 3.5:** Comparison of infrared spectra of 1100 L HCONH<sub>2</sub> at 70 K after dosing (bottom), upon warm-up to 165 K (middle), and upon cooling back to 70 K (top). The middle and top spectra both show the sharpened features are irreversible.

### 3.3.1.6 Analysis of Main C=O Stretch of Formamide Upon Warm-up

Because of its intense spectral feature, the C=O bond of formamide is a good probe to highlight new molecular positions or local disturbances. See Figure 3.6A for the maximum peak position and Figure 3.6B for the absolute intensity of the main C=O stretch as a function of increasing temperature for the three formamide isotopes. As shown in Figure 3.6A, the peak position changes to higher frequencies from 70 K to 165 K and then red shifts back to lower frequencies starting at ~220 K. The only exception is the HCOND<sub>2</sub> ice where the peak position slightly blue shifts from 240 K up to 380 K. The influence of the nitrogen-deuterium bond (ND) on the C=O of formamide may account for this frequency increase at the higher temperatures. As shown in Figure 3.6B, the absolute intensity of the band starts to increase at ~150 K, also evidenced by the sharpened bands in the IR spectra (Figure 3.4). Also, the FWHM (full width at half maximum) of the main C=O stretching band is 58.7 at 70 K and 29.4 at 165 K, confirming the band's sharpening/narrowing upon warm-up to 165 K. Figure 3.6B shows another change in the intensity of the band starting at ~220 K for all three ices as desorption begins (see Section 3.3.1.7) until the intensities fall to near zero at ~460 K, indicating complete desorption. Also, the main C=O band appears to contain more than one feature (depending upon temperature), and might be a combination of bands at certain temperatures when ice environments overlap. See Section 3.3.2.1 for a complete discussion.

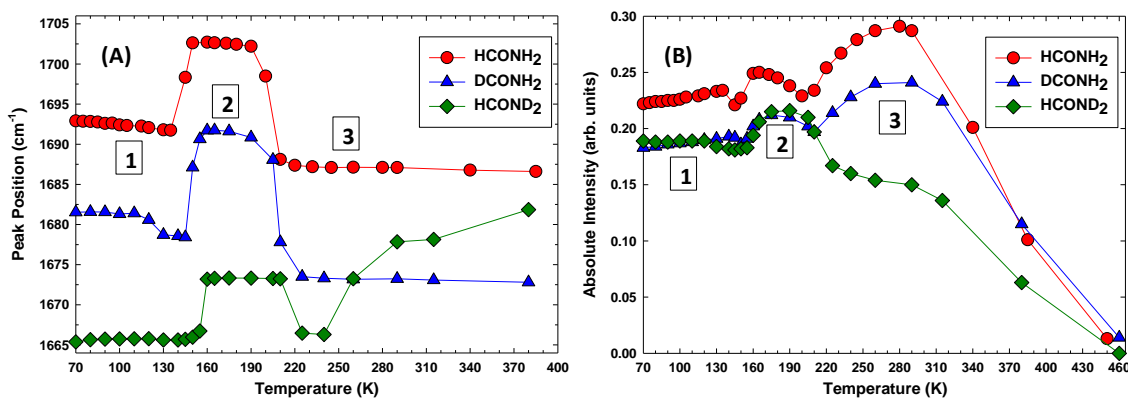


**Figure 3.6:** C=O stretch (A) infrared maximum peak position and (B) absolute intensity as a function of increasing temperature for three formamide isotopes. The changes indicate at least three distinct molecular rearrangements at: (1) 70-145 K, (2) 145-210 K, (3) 210-380 K (see Section 3.3.2.1 for discussion).

### 3.3.1.7 TPD of HCONH<sub>2</sub> on SiO<sub>2</sub> Nanopowder

TPD measurements of HCONH<sub>2</sub> (mass 45) after formamide adsorption on the SiO<sub>2</sub> nanopowder surface were performed to determine the activation energy of desorption from this grain analog as well as to confirm the desorption temperature determined from the IR spectra. See Figure 3.7 for the TPD of mass 45 after adsorption of formamide as a function of increasing coverage dosed at 70 K onto the SiO<sub>2</sub> substrate. A significant desorption signal is not seen until a dosage of 300 L. According to a prior TPD study of formamide on Ru(001) at 80 K, a multilayer peak is expected at 210 K followed by a monolayer peak at 225 K [132]. It is clear from Figure 3.7 that desorption from SiO<sub>2</sub> begins near 200 K, with peak maximum at ~228 K. Desorption is near completion by ~450 K, which is consistent with the IR spectra of HCONH<sub>2</sub> shown upon warm-up (Figures 3.1) in which no formamide peaks are observed at this temperature. The broad TPD peak indicates slow diffusion through the high-surface-area powder from 200-450 K.

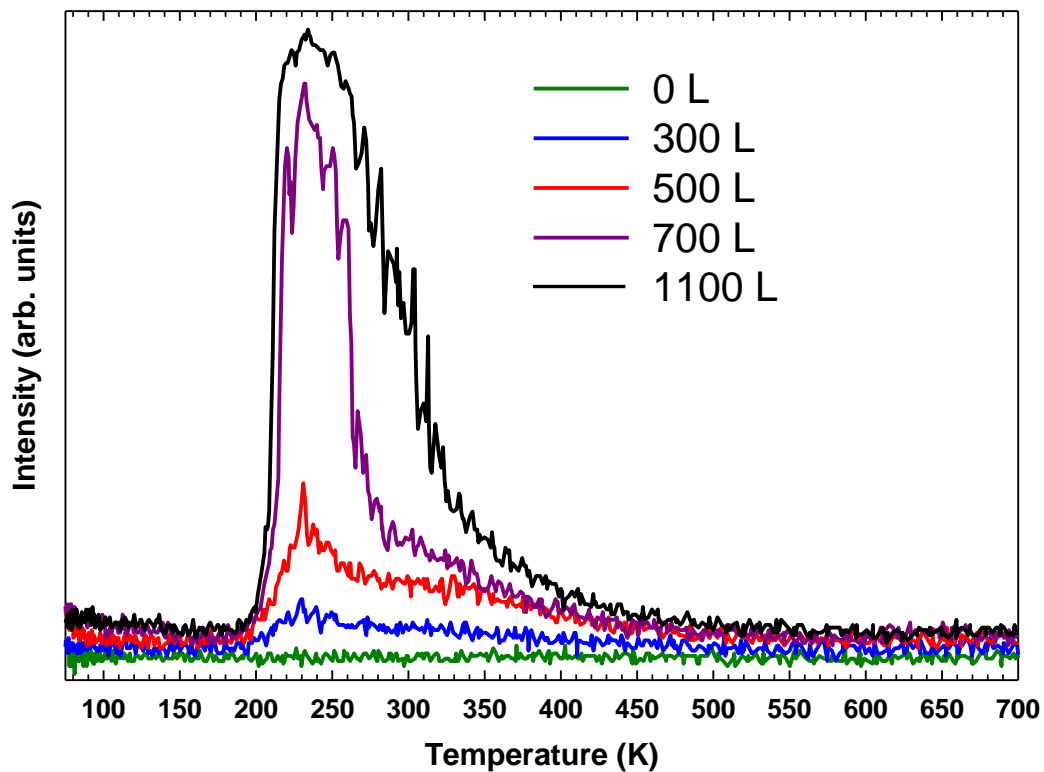


**Figure 3.7:** TPD of mass 45 (HCONH<sub>2</sub>) after adsorption of formamide on SiO<sub>2</sub> nanopowder at 70 K showing coverage dependence from 0 to 1100 L. Maximum peak desorption occurs at ~228-233 K; ramp rate = 0.5 K/s.

### 3.3.2 Discussion

#### 3.3.2.1 Molecular Rearrangement Upon Warm-up

We attribute changes in the maximum peak position and absolute intensity of the main C=O stretch upon warm-up to represent three new C=O stretches in three different geometrical ice environments, depending on the temperature. Thus, a trend emerges from Figure 3.6 as indicated by the C=O stretch showing that the condensed formamide ices go through at least three distinct molecular arrangements: 1) a phase that is likely porous amorphous between 70-145 K [136], 2) a phase previously referred in the literature as crystalline [131,134,136] between 145-210 K, and 3) a phase between 210-380 K when the disappearance of the bands of the condensed layer indicate that multilayer formamide diffuses from the free volume (pores) between the SiO<sub>2</sub> grains as desorption begins. We speculate that the porous amorphous formamide ice becomes crystalline formamide ice at ~145-160 K [134], based on the temperature at which the IR changes begin to occur (~145 K). A recent VUV spectroscopy study has reported that formamide undergoes an amorphous to crystalline phase change at ~160 K [136], which supports our results. They also suggested that above 200 K polymerization within the ice is possible [136]. However, we note that one prior study [135] of photon-stimulated desorption (PSD) of formamide on Si(100) at 96 K showed that (with NEXAFS spectroscopy) the CNO plane is tilted at an angle of ~42° away from the surface. They suggested that the formamide at 96 K was not amorphous under their single crystal conditions. The sharpened features seen in our spectra starting at ~145 K could be attributed to second-order effects produced by a large anharmonicity associated with the hydrogen bonds in the formamide ice network, as mentioned by Torrie and Brown [131]. A prior TPD study of formamide

on Ru(001) has reported that at high coverages, competing decomposition and desorption pathways occur at 225 K. The decomposition at 225 K could be due to a N-bonded NHCHO intermediate (with likely similar IR features), which eventually decomposes to CO, N and H at ~375 K [132]. This appears consistent with our IR results. We should note that at 290 K, most of the other formamide bands almost completely reduce in intensity while the C=O stretch does not significantly reduce until ~380 K (see Figure 3.6). This could be due to decomposition of formamide on the surface [132]. In addition, the previously mentioned HREELS study reports that formamide hydrogen-bonded multilayers undergo autocatalytic desorption at 223 K [137], which is consistent with the onset of the third pre-melting phase in our IR spectra and our TPD results (Section 3.3.1.7). A crystal structure analysis was performed by Ladell and Post at 223 K, and they reported a monoclinic structure containing four formamide molecules in a unit cell [138]. In addition, Itoh and Shimanouchi have accounted for low frequency band splitting as hydrogen bonding and intermolecular interactions within formamide ices at 208 K and 108 K, which could contribute to some of the features seen in our spectra, although their study was performed under ambient conditions [130]. Finally, several enol-keto tautomers and transition states have been calculated with DFT [139,140], but we observe no spectroscopic evidence for the O-H group. Thus, depending upon the temperature, several different formamide configurations within the hydrogen-bonded ice network are possible [130,137].

### 3.3.2.2 SiO<sub>2</sub> Changes Upon Warm-up

Several IR peaks (denoted by \* in Figures 3.1-3.4) are seen upon warm-up and are attributed to the molecular rearrangement of the SiO<sub>2</sub> substrate and/or temperature effects on the SiO<sub>2</sub> vibrations. The negative IR peak seen in all the isotopic experiments near 1253 cm<sup>-1</sup> that increases negatively with increasing temperature is reversible and is thus a temperature effect on the vibration. It corresponds to the LO (longitudinal) partner of the TO (transverse) phonon mode of the asymmetric motion of Si-O-Si bridges in which adjacent oxygen atoms execute the asymmetric motion in phase with each other [141]. In addition, the peak at 1007 cm<sup>-1</sup> is due to reversible temperature effects on the SiO<sub>2</sub> bands (Si-O-Si stretches at ~1050-1230 cm<sup>-1</sup>) [142]. This is confirmed by the disappearance of these bands when the SiO<sub>2</sub> was annealed to above 165 K (up to 505 K) and cooled back to 70 K. However, the peak at 960 cm<sup>-1</sup> attributed to the Si-O-H stretch [142] is due to a molecular rearrangement in the SiO<sub>2</sub> with increasing temperature, and is not reversible. This rearrangement likely involves the surface hydroxyls of the buried silicate surface. This SiO<sub>2</sub> structural change may or may not influence formamide ice, since the 960 cm<sup>-1</sup> peak growth begins early at ~130 K in all the ices, which is earlier than the formamide ice changes appear. An optical screening effect was mentioned previously by Yates et al. [45], in which the SiO<sub>2</sub> underlying substrate vibrations may be inhibited by an overlying ice until a sufficient temperature is reached. It has been ruled out here by verifying the warm-up behavior in control SiO<sub>2</sub> IR warm-up experiments performed without formamide, as well as with H<sub>2</sub>O dosed on the SiO<sub>2</sub> as a control to monitor the warm-up behavior with a different ice (not shown). All the same SiO<sub>2</sub> features were visible in both experiments upon warm-up.

### 3.3.2.3 Temperature Programmed Desorption Analysis

The Redhead peak maximum method [54,143], which assumes activation parameters that are independent of coverage, was used to extract the activation energy of desorption from the TPDs of formamide on SiO<sub>2</sub> (Figure 3.7), using the equation

$$E_{act} = RT_m \left[ \ln \left( \frac{\nu T_m}{b} \right) - 3.46 \right]$$

where  $R$  is the Boltzmann constant,  $\nu$  is the frequency factor typically employed ( $10^{13} \text{ s}^{-1}$ ) that introduces less than 1.5% error,  $T_m$  is the desorption peak maximum, and  $b$  is the heating rate (0.5 K/s). The mean values were calculated from several TPD experiments at different coverages.

The Redhead equation yields a mean  $E_{act}$  of 14.7 +/- 0.17 kcal/mol (0.64 +/- 0.007 eV) for  $T_m = 228 \text{ K} \pm 2.58$  for all experiments at doses of 25-1100 L at a sample temperature of 70 K. This activation energy may be partially due to an interaction between formamide and SiO<sub>2</sub> at the buried interface representing hydrogen bonding/strong physisorption between the hydroxyls of SiO<sub>2</sub> and formamide.

## 3.4 Lyman- $\alpha$ Processing of Pure Formamide Ices on SiO<sub>2</sub>

### 3.4.1 Results

#### 3.4.1.1 IR Spectra After Lyman- $\alpha$ Irradiation of HCONH<sub>2</sub> Ice on SiO<sub>2</sub> at 70 K

Figure 3.8 presents the IR difference spectra of 1100 L pure HCONH<sub>2</sub> ice at 70 K as a function of Lyman- $\alpha$  (121 nm) irradiation time (hr). The ice was irradiated for a total of ~72 hours, upon which the formamide peaks are seen to decrease with increasing irradiation, indicating that formamide is partially consumed as the ice is irradiated. A weak band at 2163 cm<sup>-1</sup> developed as the UV exposure time was increased. This band is assigned to a chemisorbed cyanate species (OCN<sup>-</sup>) [115]. In addition, a small peak at 2135 cm<sup>-1</sup> on the right shoulder of the OCN<sup>-</sup> band starts to develop at the same time and is assigned to CO [112,134]. No other peaks are observed as a result of the Lyman- $\alpha$  photolysis of formamide, unlike the ion irradiation study of pure formamide ice that additionally reports CO<sub>2</sub>, HNCO, N<sub>2</sub>O, and <sup>-</sup>CN and NH<sub>4</sub><sup>+</sup> [24]. The peak seen at 2343 cm<sup>-1</sup> represents gas-phase and solid CO<sub>2</sub> contamination, since it has been confirmed with control experiments. In addition, control experiments (not shown) were also performed of formamide ice for the same length of time (without irradiation) and showed no growth in products. This confirmed that the OCN<sup>-</sup> and CO peaks are in fact due to a photochemically-initiated process.

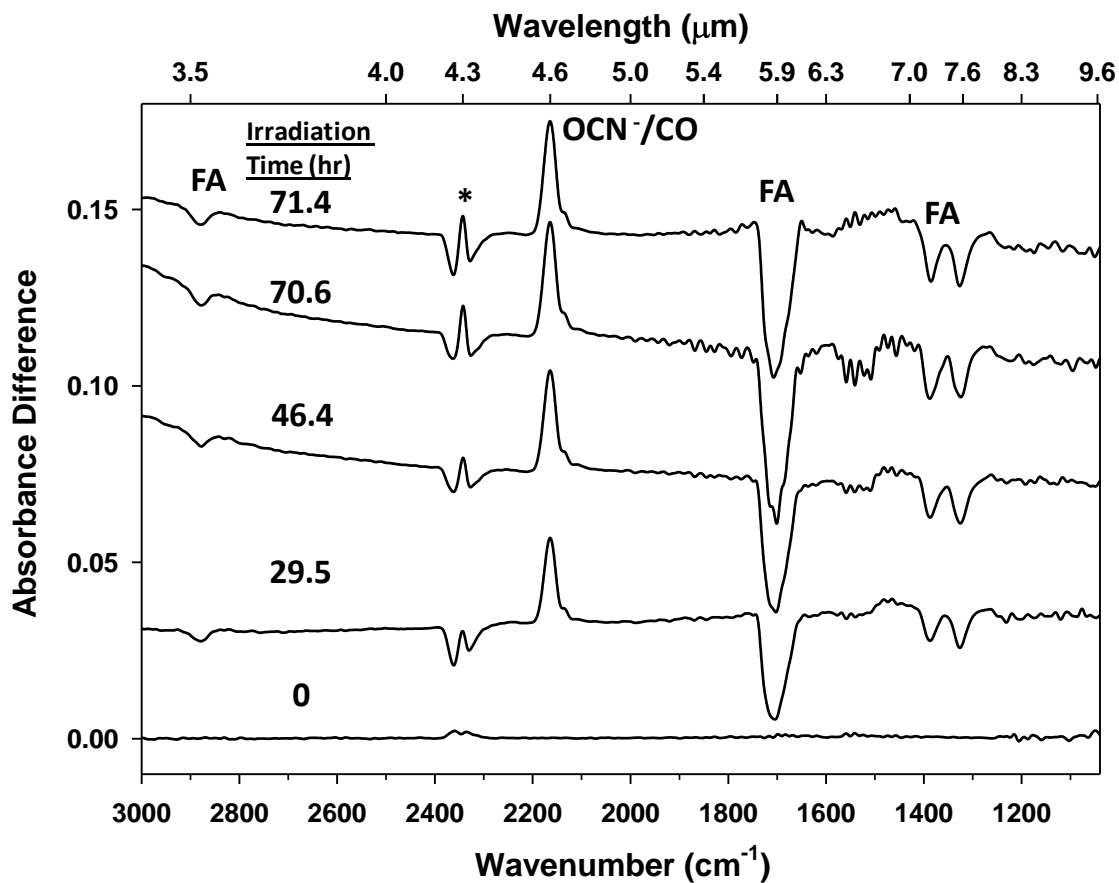


**Figure 3.8:** Infrared difference spectra of 1100 L HCONH<sub>2</sub> ice as a function of increasing Lyman- $\alpha$  irradiation time (hr) at 70 K. The formamide (FA) peaks decrease as a function of irradiation time, and the OCN<sup>-</sup> peak at 2165 cm<sup>-1</sup> increases with irradiation time. Peak with \* is due to CO<sub>2</sub> contamination.

### 3.4.1.2 Product Peak Growth Upon Irradiation

Figure 3.9 provides a close-up of the IR region where products are observed with increasing irradiation time. It is clear that  $\text{OCN}^-$  and CO both start forming as early as 1.8 hr into the experiment. However, after the initial large amount of product formation by 25.5 hr, the growth becomes slower. This is clear from Figure 3.10 which presents the integrated combined peak areas of the  $\text{OCN}^-$  and CO peaks as a function of VUV irradiation time. The inset shows a close-up of the initial 5.5 hr, in which the growth appears quite linear with time. After the initial 5.5 hr, the peak area grows substantially from  $\sim 0.25$  to  $\sim 0.55$  by  $\sim 22$  hr. Then the growth slows down and takes  $\sim 2$  days to achieve the same increase (0.3) that was observed in the first 5.5 hr of the reaction, indicating a plateau in product formation is almost reached. Thus, the majority of available formamide molecules are initially reacted to form the  $\text{OCN}^-/\text{CO}$  product within the first 24 hr, with a much slower rate of formation occurring at longer irradiation times. This is consistent with the formamide (FA) peak decrease seen in Figure 3.8 as a function of irradiation time, where there is not a significant additional decrease after the initial 29.5 hr. This means that even if formamide-containing ices were irradiated in star-forming regions for very long times ( $10^6$  yr, life-time of a molecular cloud [112]), formamide processing would likely reach a product formation plateau quickly. Also, the effects of water (possibly due to background deposition during the time of the experiment here) have been studied and are presented in Section 3.5.

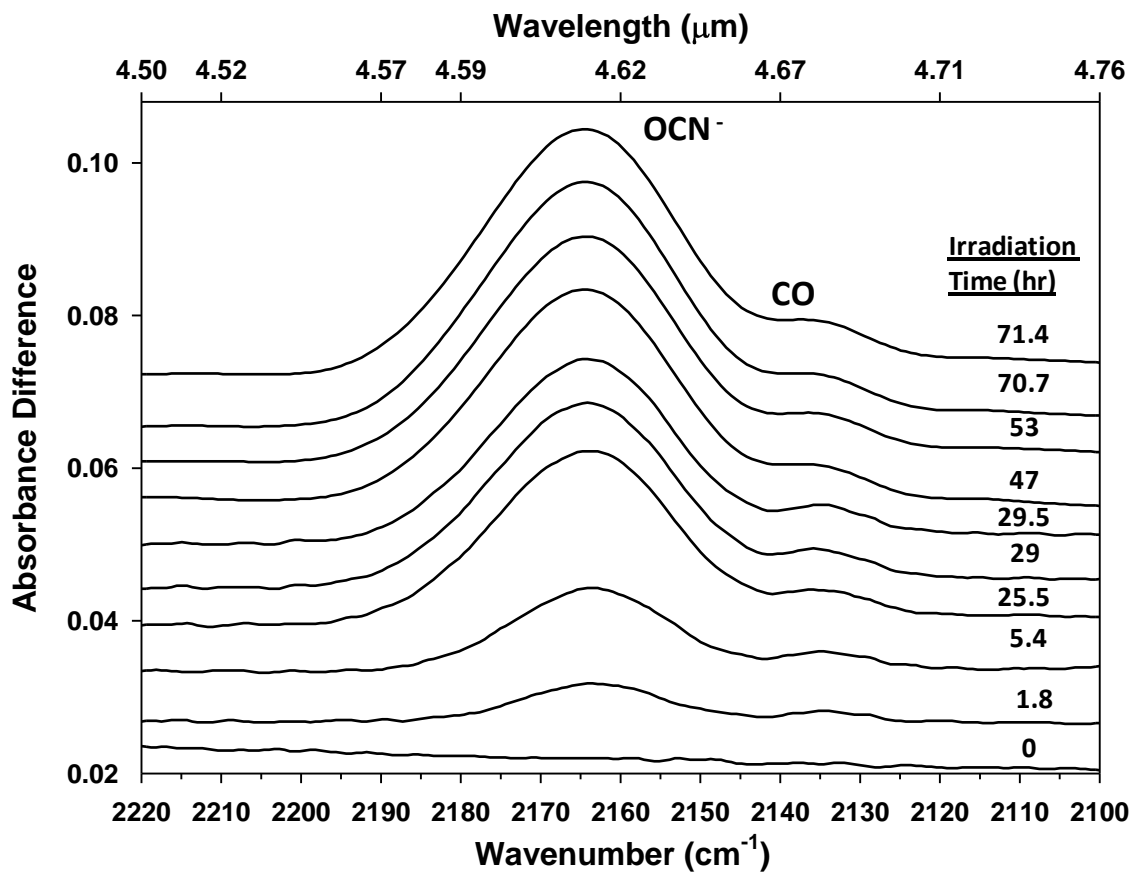


**Figure 3.9:** Infrared spectra of OCN<sup>-</sup>/CO growth as a function of increasing Lyman- $\alpha$  irradiation time (hr) for 1100 L HCONH<sub>2</sub> ice deposited and irradiated at 70 K.

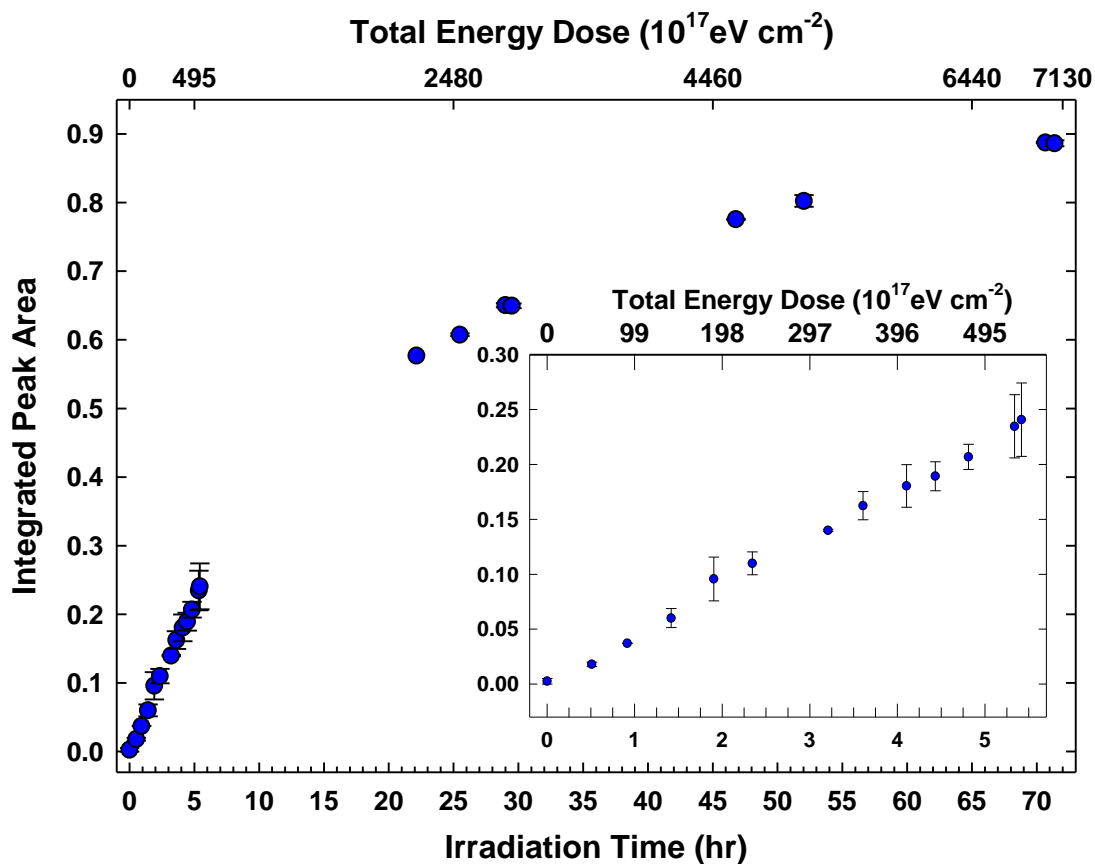


**Figure 3.10:** OCN<sup>-</sup>/CO combined product peak areas for Lyman- $\alpha$  irradiation of 1100 L HCONH<sub>2</sub> ice at 70 K as a function of irradiation time. Inset is close-up of the initial 5.5 hr of irradiation. Peak areas are calculated based on multiple experiments and after subtraction of initial spectrum (0 sec).

### 3.4.1.3 IR Spectra of Post-Irradiation Warm-up of 70 K Ice

Similar sharpening of the IR features at ~165-185 K occur with post-irradiation warm-up (see Figure 3.11A) as mentioned in non-irradiated ices (Section 3.3), indicating that irradiation does not adversely affect the molecular rearrangement that occurs in formamide ice purely due to warm-up. In addition, the OCN<sup>-</sup> and CO IR peaks begin disappearing at ~210 K (see Figure 3.11B) at the same time that formamide desorption begins (for TPD see Figure 3.7), indicating that the UV products stick within the formamide and may be trapped in the pores of the formamide ice itself or in the voids between the grains. This would not be expected of a volatile species, such as CO. Also, at 1600 cm<sup>-1</sup>, a small peak appears upon warm-up from 210-290 K that could be due to solid H<sub>2</sub>O forming on the sample. However, this is the only H<sub>2</sub>O peak seen and it remains unclear, if it is H<sub>2</sub>O, why it would not appear until such a high temperature. An alternative assignment could be a sharpened N-H stretch from formamide, which would be consistent with the other N-H stretches above 3000 cm<sup>-1</sup> upon warm-up. No other peaks grow in upon warm-up of the post-irradiated ice.

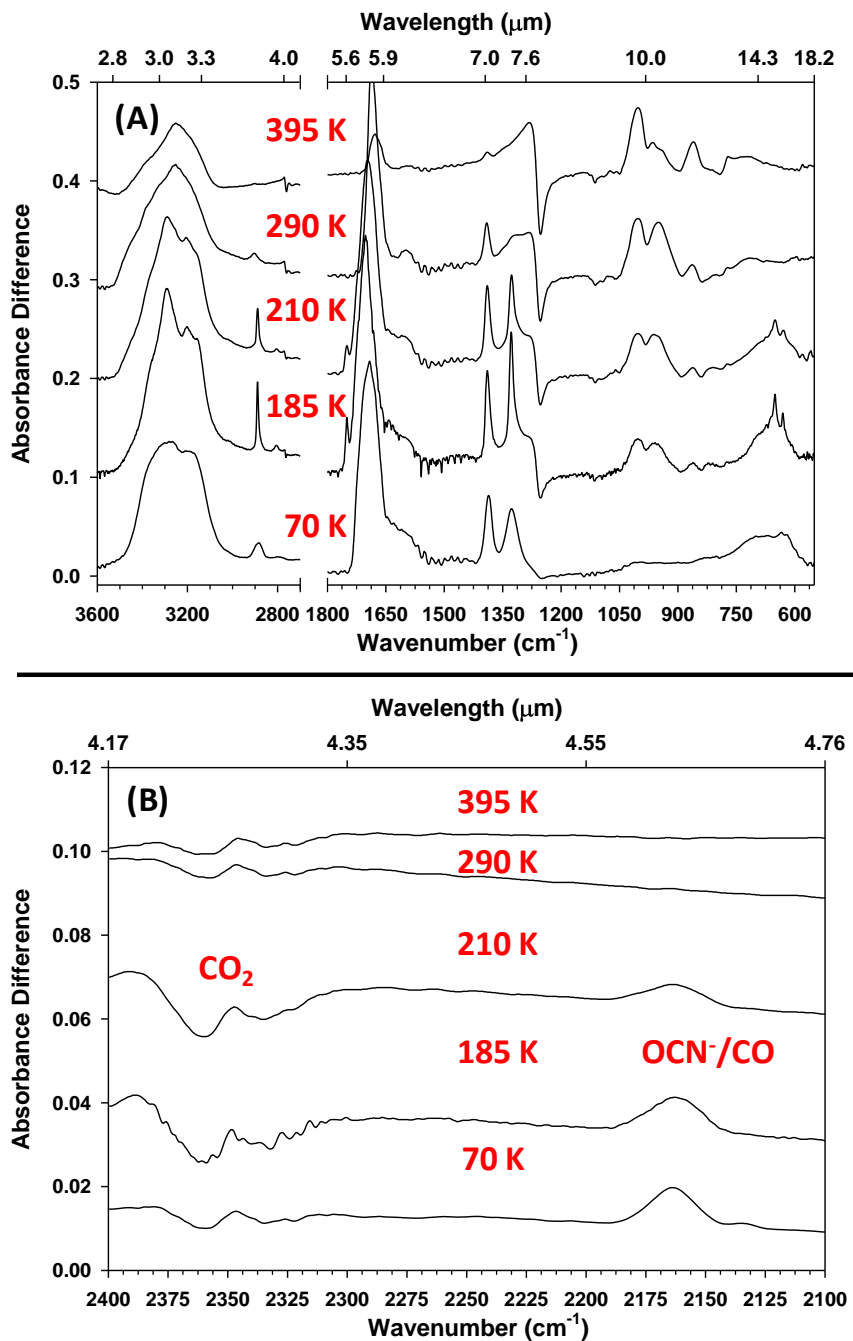


**Figure 3.11:** Infrared spectra of post-irradiation (5.5 hr) warm-up from 70 K to 395 K of 1100 L HCONH<sub>2</sub> ice. (A) displays the sharpening of features similar to non-irradiated samples and (B) displays a close-up of the OCN<sup>-</sup>, CO, and CO<sub>2</sub> region where significant desorption of products does not start until ~210 K with formamide itself.

### 3.4.1.4 IR Spectral and Product Yield Comparison of Irradiated 70 K Ice vs. 165 K Annealed Ice

Formamide ice dosed at 70 K, annealed to 165 K, and subsequently cooled to 70 K was also irradiated with Lyman- $\alpha$  photons to determine if the change in molecular arrangement upon warm-up to 165 K would change the Lyman- $\alpha$  product distribution and yields. Additional new products were not observed with irradiation of the 165 K annealed crystalline ice. However,  $\text{OCN}^-$  and CO were again observed. Figure 3.12 depicts the region of the IR spectra showing the  $\text{OCN}^-$  and CO peaks as a function of irradiation time (hr) for 70 K ice (A) compared to the 165 K annealed ice (B). The y-axis scales are consistent for both plots to show the height difference in the  $\text{OCN}^-$  peak for the two experiments. To make sure this difference was not simply within error, multiple identical experiments were performed.

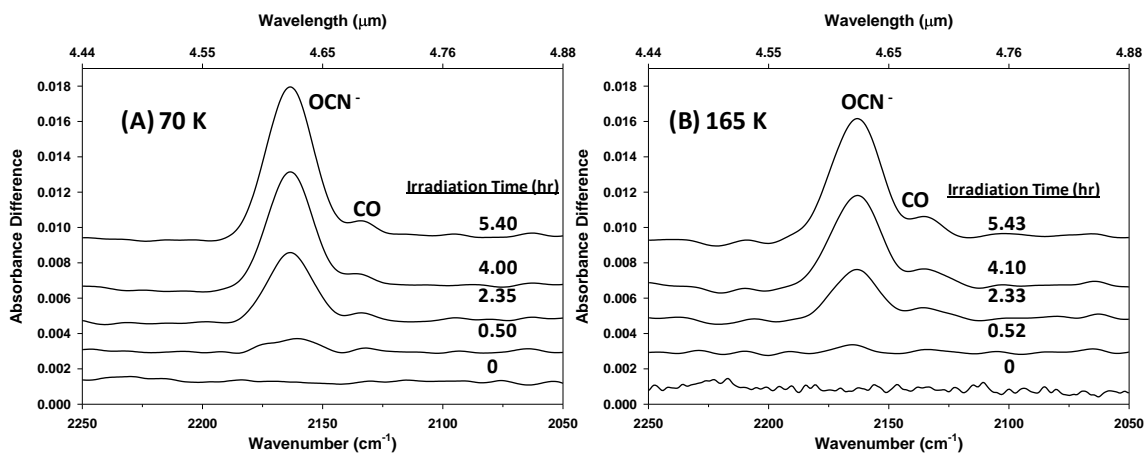


**Figure 3.12:**  $\text{OCN}^-/\text{CO}$  combined peak growth comparison during Lyman- $\alpha$  irradiation of 1100 L  $\text{HCONH}_2$  ice at (A) 70 K and (B) after annealing to 165 K. After annealing the ice to 165 K, a ~25% decrease in  $\text{OCN}^-$  and CO abundance is observed compared to the 70 K ice.

See Figure 3.13 for a plot of the OCN<sup>-</sup>/CO combined integrated peak areas as a function of irradiation time/total energy dose. Consistently, the 165 K annealed ice experiments produced less combined OCN<sup>-</sup>/CO with Lyman- $\alpha$  irradiation. After the same 5.4 hr irradiation time, ~25% less OCN<sup>-</sup>/CO was formed in the 165 K ices compared to the 70 K ices. It is postulated that the molecular rearrangement that the ice undergoes when annealed to 165 K partially inhibits the formation of the VUV products. In a porous amorphous formamide ice at 70 K, the surface area of exposed molecules is expected to be higher, allowing more VUV processing to occur than in a compacted polycrystalline 165 K annealed ice. As discussed, formamide desorption does not begin until ~220 K, so some thermal removal of formamide did not cause the lack of product growth for the 165 K annealed ice.

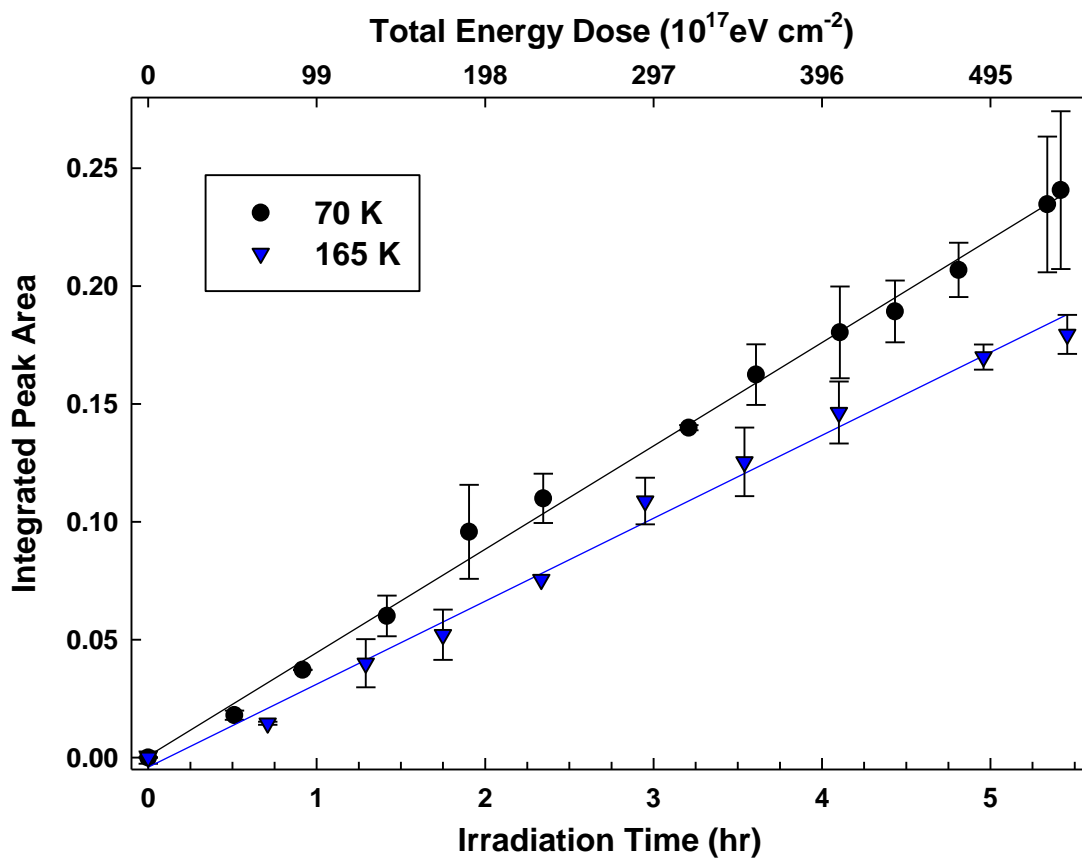


**Figure 3.13:** Combined OCN<sup>-</sup>/CO product peak areas as a function of Lyman- $\alpha$  irradiation time for 1100 L HCONH<sub>2</sub> ices irradiated at 70 K (black) compared to ices annealed to 165 K then cooled to 70 K prior to irradiation (blue). Peak areas are calculated based on multiple experiments and after subtraction of initial spectrum (0 sec). An increased amount of OCN<sup>-</sup> and CO is produced at 70 K compared to the ices that underwent prior annealing to 165 K. A linear regression fit has been applied to each data set.

#### 3.4.1.5 H<sub>2</sub> TPD of Post-Irradiation Warm-up of 70 K Ice and 165 K Annealed Ice

The TPD of mass 2 (H<sub>2</sub>) is shown in Figure 3.14 below for un-irradiated formamide ice (black) compared to formamide ice irradiated for 72 hr (blue) at 70 K (left pane) and upon annealing to 165 K (right pane). The non-irradiated 70 K ice showed no desorption of H<sub>2</sub> from 90-140 K even if the ice is allowed to sit on the sample for 72 hr. However, after UV exposure a new peak arises at ~90-140 K. When the ice was annealed to 165 K prior to irradiation, again H<sub>2</sub> desorption appears at 90-140 K after irradiation. However, again, no such peak is seen for annealed ice that is not irradiated. The single peak starting at ~90 K is also less broad than in the 70 K ice. Integration of these peaks indicates that 54% less H<sub>2</sub> product is formed in the 165 K annealed ice. See Section 3.4.2.2 for discussion.

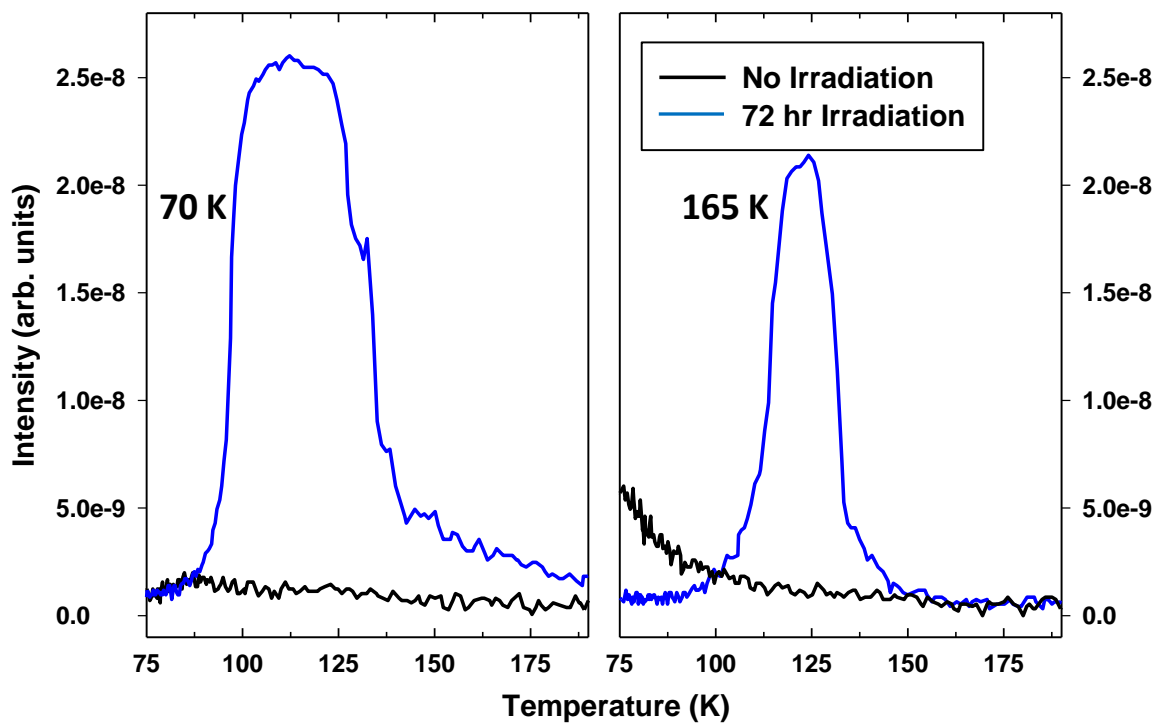


**Figure 3.14:** TPD spectra of mass 2 ( $\text{H}_2$ ) after adsorption of 1100 L  $\text{HCONH}_2$  on  $\text{SiO}_2$  nanopowder at 70 K and after annealing to 165 K for both no irradiation (black) and after 72 hours of Lyman- $\alpha$  irradiation (blue). A peak is clearly observed after irradiation (blue) at  $\sim 90$ -150 K indicating  $\text{H}_2$  is formed in the ice upon irradiation. Ramp rate = 0.5 K/s.

### 3.4.2 Discussion

#### 3.4.2.1 Column Densities of Products After 72 hr Lyman- $\alpha$ Irradiation

The intrinsic IR band strengths ( $A$ ) of  $\text{OCN}^-$  and CO have been determined previously [144,145]. For  $\text{OCN}^-$  at  $2164\text{ cm}^{-1}$ ,  $A = 1.3 \times 10^{-16}\text{ cm mol}^{-1}$ , and for CO at  $2135\text{ cm}^{-1}$ ,  $A = 1.1 \times 10^{-17}\text{ cm mol}^{-1}$ . From these band strength values and the integrated areas of our products after 72 hr of Lyman- $\alpha$  photolysis at 70 K, we can estimate the column densities ( $N$ ) of both  $\text{OCN}^-$  and CO in our pure formamide ice based on the following formula where  $\int \tau(\nu) d\nu$  is the optical depth or area under the peak.

$$N = \frac{\int \tau(\nu) d\nu}{A}$$

To obtain the individual areas of the  $\text{OCN}^-$  and CO peaks, they were fit using a Gaussian function. From this formula, the column density ( $N$ ) of  $\text{OCN}^-$  after 72 hr of irradiation was calculated to be  $1.1 \times 10^{16}\text{ cm}^{-2}$ , and the column density ( $N$ ) of CO after 72 hr of irradiation was calculated to be  $1.27 \times 10^{16}\text{ cm}^{-2}$ . This indicates that the formation yield of CO produced in our ice is essentially the same as the yield of  $\text{OCN}^-$ . In addition, formamide ice at 70 K before irradiation has a calculated density of  $2.11 \times 10^{17}\text{ cm}^{-2}$  (for the  $1388\text{ cm}^{-1}$  band), based on  $A = 0.68 \times 10^{-17}\text{ cm mol}^{-1}$  as reported by Brucato et al. [24]. After, 72 hr of irradiation, formamide's calculated column density is  $1.5 \times 10^{17}\text{ cm}^{-2}$ , indicating a ~29% loss (or consumption) of formamide upon 72 hr of photolysis. Of note, the decrease in formamide's band strength amounts to  $6.1 \times 10^{16}\text{ cm}^{-2}$ , whereas the total  $\text{OCN}^-$  and CO produced adds up to  $2.37 \times 10^{16}\text{ cm}^{-2}$ . This discrepancy could be due to inaccuracies of chosen band strengths or an indication

that other processes are occurring (e.g.,  $\text{NH}_3$  formation and sublimation) that are not easily observed (see Section 3.4.2.3.5).

#### 3.4.2.2 Post-Irradiation Temperature Programmed Desorption Analysis

The post-irradiation TPD of mass 45 was not changed compared to the TPD (at 1100 L) shown in Figure 3.7 of non-irradiated formamide. From post-irradiation TPD of mass 45 (not shown), it was difficult to quantitatively determine how much formamide was transformed to products, how much re-formed to formamide, and how much of original ice simply desorbed. In addition, mass 42 (OCN) and mass 43 (HNCO) post-irradiation TPD were monitored (not shown). These have very weak TPD signals that upon post-irradiation did not change enough to be detectable.

However, from the post-irradiation TPD of mass 2 ( $\text{H}_2$ ) shown in Figure 3.14, it was apparent that Lyman- $\alpha$  photolysis induced some dissociations since a peak is observed from 90-140 K after irradiation. One possibility is that after ionization by the photon, electron-hole recombination occurs from trapped electrons and holes producing an excited state that can then decompose to yield  $\text{H}_2$ . The new TPD peak for mass 2 arising at  $\sim 90$  K after irradiation indicates that  $\text{H} + \text{H}$  recombines to form  $\text{H}_2$ , either in the ice, upon warm-up of the ice, or within the mass spectrometer.

The post-irradiation TPD of mass 2 ( $\text{H}_2$ ) of formamide ice that was annealed to 165 K (Figure 3.14) prior to irradiation indicates that less formamide may be available to undergo dissociation upon Lyman- $\alpha$  irradiation in the annealed ice. Electrons and holes travel further in crystalline ices and have less trapping probability. Possibly, only the formamide that did not diffuse in the deeper pores during the annealing will fragment into  $\text{H}_2$  (or other fragments). Thus, these post-irradiation TPD experiments help confirm our

postulation of a molecular rearrangement at 165 K as well as relative product formation during VUV irradiation (H, H<sub>2</sub>, OCN<sup>-</sup>, CO) for our 70 K and 165 K annealed formamide ices.

### 3.4.2.3 Product Formation From Lyman- $\alpha$ Irradiation of Pure Formamide Ices

#### *3.4.2.3.1 SiO<sub>2</sub> Substrate Effects on Product Formation*

Due to the shallow penetration depth of Lyman- $\alpha$  photons (typically 100-150 nm [146]) compared to the estimated maximum thickness of our ice (~877 nm) as well as formamide's high absorption at low wavelengths [147], we assume that the UV photons do not penetrate to the substrate in our experiments. Thus, we are assuming that the primary OCN<sup>-</sup> and CO product formation occurs independently of the SiO<sub>2</sub> substrate, although influence of the substrate cannot completely be ruled out since the lack of HCN and NH<sub>3</sub> bands in our photolysis experiments are consistent with the ion irradiation study of olivines (MgFeSiO<sub>4</sub>), which demonstrated clear surface effects [116]. In addition, ices grow non-uniformly as thick clusters on a substrate so there could be very thin regions where the photons can penetrate to the SiO<sub>2</sub>.

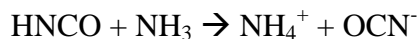
Rajappan et al. reported Lyman- $\alpha$  irradiation experiments on a very similar bare SiO<sub>2</sub> nanopowder grain stimulant and found a negligible loss in the Si-OH groups [33]. Our IR spectra suggested almost no changes in the SiO<sub>2</sub> features as a function of increasing irradiation. We do however note that the SiO<sub>2</sub> surface could limit the yield of our products due to its scattering ability for Lyman- $\alpha$  radiation [148].

Regarding the production of H<sub>2</sub> in the post-irradiation TPD, prior reports have demonstrated that H + H recombination reactions are favored on similar

surfaces [149,150], so we cannot rule out the influence of our SiO<sub>2</sub> surface on the production of H<sub>2</sub> in the non-uniform ice during irradiation.

#### 3.4.2.3.2 OCN<sup>-</sup> Assignment and Proposed Formation Mechanism

Several works have identified the peak near 2165 cm<sup>-1</sup> in lab-based studies, starting from either formamide or small molecules such as CO or CO<sub>2</sub> and NH<sub>3</sub> [24,32,62,112,115,116,151,152]. This band has also been identified in interstellar spectra and assigned to OCN<sup>-</sup> based on isotopic lab-based experiments [36]. However, Pendleton et al. [153] has suggested several alternatives to the OCN<sup>-</sup> ion assignment for the 4.62 μm band (2165 cm<sup>-1</sup>), including isonitriles and silanes (-SiH<sub>3</sub> or -SiH<sub>4</sub>). The study by Pendleton et al. mentions that several other bands have been searched for to substantiate the assignment as OCN<sup>-</sup> but none have yet been found. However, they suggest that other candidates have poor, weak or unknown feasibility (incomplete lab data) compared to OCN<sup>-</sup>, which has good feasibility since many NH<sub>3</sub>-containing reactions (UV, ion) produce the band. Several reports have followed suit with this assignment, as do we. One reason is the well-known acid-base reaction of NH<sub>3</sub>-containing ices leading to OCN<sup>-</sup>, as given below.



The formation mechanism in ice leading to this negative ion (OCN<sup>-</sup>) from non-NH<sub>3</sub> containing ices, if the assignment is correct, has not been fully deduced. Theule et al. [154] have discussed a thermal reaction from HNCO and H<sub>2</sub>O leading to OCN<sup>-</sup> but also mention that this reaction alone does not account for the abundances found in astronomical IR sources. Thus, another reaction must also contribute. One possibility is the reaction of HCN with H<sub>2</sub>O. Gerakines et al. [115] showed that energetic processing

of HCN + H<sub>2</sub>O-dominated ices (even without NH<sub>3</sub>) quickly converts to the species assigned as OCN<sup>-</sup>. Thus, if formamide is just a carrier for HCN + H<sub>2</sub>O, as previously suggested [22], then OCN<sup>-</sup> would be an expected product and could be an explanation for the OCN<sup>-</sup> seen upon Lyman- $\alpha$  photolysis of our formamide ice. Additionally, Duvernay et al. reported 240 nm UV irradiation of formamide producing quick formation of formimidic acid (H-N=C(H)-OH) isomers, which are so transient that they are not visible with IR in our ices. These isomers can decay via a unimolecular channel to form •HC=NH and •OH radicals that can break apart to form HCN + H<sub>2</sub>O and then further lead to OCN<sup>-</sup> [115]. This pathway is an example that NH<sub>3</sub> is not a necessary starting ingredient for OCN<sup>-</sup> in astrophysical ices, although it may be an intermediate. Of note, Gerakines et al. [115] observe HNCO at 2268 cm<sup>-1</sup>, a possible product of HCN + H<sub>2</sub>O that further leads to OCN<sup>-</sup> as described above. The lack of HNCO in our ice could just mean it reacts quickly.

The primary mechanisms we suggest leading to OCN<sup>-</sup> are direct ionization followed by ion-electron recombination, direct photodissociation leading to removal of H or H<sub>2</sub>, and dissociative electron attachment. It is possible that ionization, electron-hole recombinations, and secondary electron attachment mechanisms are all possible from a 10 eV photon. An ionized formamide molecule (cation) could be produced upon irradiation with 10.2 eV photons, since the energy provided is slightly above the ionization potential (IP), and dissociative transitions can be excited. Indeed, calculations [155] suggest that formamide has an ionization energy of 10.1 eV which could be lowered in ice leading to H<sub>2</sub>N-CH(=O)•<sup>+</sup>. The ionized formamide cation could then serve as the counter ion to OCN<sup>-</sup> [133]. Another possibility is that the photon abstracts one H

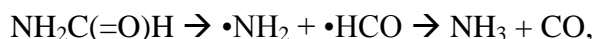
(leading to H<sub>2</sub> in the TPD), giving H<sub>2</sub>NCO<sup>+</sup> cation that can be the counter ion to OCN<sup>-</sup>. Ionization tends to have a high cross section in the condensed phase compared to photoabsorption because the wavefunction overlaps neighbors so the highly excited states above the continuum become delocalized, allowing facile autoionization and a large amount of excited state proton transfer reactions [122,123,156]. Ionization itself could then be followed by ion-electron and neutral-electron recombination reactions leading to OCN<sup>-</sup>.

Finally, gas-phase dissociative electron attachment (DEA) measurements have indicated that the dominant DEA channels of formamide are CN<sup>-</sup> and OCN<sup>-</sup>, formed through intensive resonances at 2.0 eV and 6.7 eV, respectively [157]. Thus, a counter ion to OCN<sup>-</sup> may not be needed if DEA is invoked by a 10 eV photon. However, Gerakines et al. [31] suggest that “secondary electrons produced by photolysis do not have enough energy to form stable negative ions” as an explanation for the lack of formate ion (HCOO<sup>-</sup>) produced in their UV experiment. A recent paper calculated the DEA resonances and suggested that H-C and N-H bond dissociation was not favored for TNIs in the gas phase [158]. Our results in the condensed phase suggest H dissociation is dominant, but it is unclear if DEA is invoked. For DEA to be invoked, we would need at least 2-4 eV electrons to be produced from a 10 eV Lyman- $\alpha$  photon, which might only occur if the SiO<sub>2</sub> substrate is involved. Also, charge trapping can occur in the condensed phase, and DEA can have larger cross sections and shifted energies, compared to the gas phase. All of these possibilities can change the photophysics of the mechanism. However, the exact mechanism of OCN<sup>-</sup> formation (and lack of HNCO) from Lyman- $\alpha$  irradiation remains unclear. We note that 1 keV electron irradiation of the formamide ice also

produced OCN<sup>-</sup>, which could also result from a DEA pathway. This data is presented in Section 3.6.

#### 3.4.2.3.3 CO Formation

The presence of CO in our irradiated formamide ice has also been observed in similar studies [24,32]. Ferus et al. [117] and Nguyen et al. [61] have both reported that the following decarboxylation reaction occurs in the ground state.



which is considered the most effective photodissociation channel in the gas phase. The n- $\pi^*$  transition occurs in the VUV region [117], and the excited formamide can then decompose to the two radicals and further to CO and NH<sub>3</sub>.

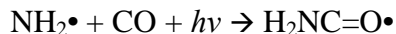
Chen et al. [32] suggested that CO could be formed without NH<sub>3</sub> via the following pathway if CO<sub>2</sub> is present initially:

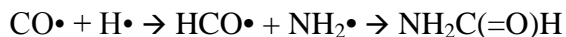


This could be a likely reaction in our ice since we do not see evidence for NH<sub>3</sub> (see Section 3.4.2.3.5) and since CO<sub>2</sub> is produced very early in the reaction as evidenced in the IR spectra.

#### 3.4.2.3.4 Reformation of Formamide

Formamide can easily reform from between two radicals, and this was reported recently by Jones et al. [112]. In addition, the H<sub>2</sub>NC=O<sup>•</sup> radical (or H<sub>2</sub>NC=O<sup>+</sup> ion) was proposed by Zhang et al. [159] and only requires 15 kJ mol<sup>-1</sup> (0.16 eV) to form. See the reactions below.





In addition, Pendleton et al. [153] points out the possibility of grain surface chemistry from HNCO and NH<sub>3</sub>, possibly leading back to formamide. Prior studies have also commented on the possibility of H<sub>2</sub>NCO<sup>+</sup> cation as an interstellar species [133]. We report photochemical abstraction of hydrogen from formamide and thus, suggest that formamide could be a source of this cation in interstellar regions. These reformation processes could also account for the minimal loss (~29%) of formamide with ~72 hr Lyman- $\alpha$  photolysis.

#### 3.4.2.3.5 *Lack of NH<sub>2</sub>, NH<sub>3</sub>, NH<sub>4</sub><sup>+</sup>, HCN, and H<sub>2</sub>O*

Upon Lyman- $\alpha$  irradiation of formamide, we see no evidence (either with IR or TPD) for NH<sub>2</sub>, NH<sub>3</sub>, NH<sub>4</sub><sup>+</sup>, HCN, and H<sub>2</sub>O. While the non-detection of these expected products could simply be due to not enough produced in our ice with Lyman- $\alpha$  for IR detection, other possibilities are that these are transient and reactive species or that the condensed-phase chemistry precludes pathways leading to them. We also performed 1 keV electron irradiation and did not observe these species with this radiation source either (see Section 3.6). The major products (OCN<sup>-</sup>, CO, H, H<sub>2</sub>) we observe do suggest that the condensed-phase reaction pathways are very different from those seen in gas-phase studies [61].

First, the lack of a band at 1100 cm<sup>-1</sup> indicates no NH<sub>3</sub> is formed [146], which is in contrast to proposed reactions given above leading to CO and NH<sub>3</sub>. NH<sub>3</sub> is a volatile species and could sublime at 70 K, if produced. Also, it is possible that radical intermediates instead further breakup [32], leaving CO in high abundance in our ice, as

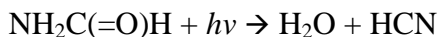
shown below.  $\text{NH}_2\bullet$  would then have overlapping IR spectral features with formamide, making it difficult to identify.



Then, even if a small amount of  $\text{NH}_3$  does re-form from the  $\text{NH}_2\bullet$  and  $\text{H}\bullet$  produced, it likely quickly photo-dissociates to  $\text{N}_2$  and  $\text{H}_2$  as described by Leoffler and Baragiola [146].  $\text{N}_2$  desorption is possible since a large mass 28 signal is observed with our QMS (also could be CO) during and after Lyman- $\alpha$  photolysis of formamide. The  $\text{H}_2$  is also confirmed in our TPD experiments.

$\text{NH}_4^+$  is not present in our ices as evidenced by the lack of a peak [24] at  $\sim 1478 \text{ cm}^{-1}$  for  $\text{NH}_4^+$  or a peak [36] at  $2217 \text{ cm}^{-1}$  for the  $\text{NH}_4^+\text{OCN}^-$  complex after irradiation. To further determine if  $\text{NH}_4^+$  would be visible in our ices, we estimate the integrated area of the band at  $1479 \text{ cm}^{-1}$  by assuming that the column density of our  $\text{OCN}^-$  after irradiation is equal to the column density of  $\text{NH}_4^+$  if both were produced in equal amounts from the acid-base reaction. Using the band strength of  $A = 4.4 \times 10^{-17} \text{ cm mol}^{-1}$  for  $\text{NH}_4^+$  as adopted from Schutte et al. [160], we would expect an integrated area of 0.484 for  $\text{NH}_4^+$ , which if present in our ices would be visible with IR. To compare, the fitted area of CO at  $2135 \text{ cm}^{-1}$  was 0.14, which is seen in our ice spectra. We further note that if  $\text{NH}_4^+$  were present, it could be observed at least up to 300 K [160].

HCN and  $\text{CN}^-$  peaks ( $2100$  and  $2080 \text{ cm}^{-1}$ ) also do not appear upon Lyman- $\alpha$  irradiation, so we have no evidence that the below reaction occurs, although it is considered a dominant pathway from formamide in the gas-phase [117].



However, the lack of HCN is consistent with a prior matrix isolation study of formamide 193-nm photolysis [118] and a theoretical study of the photo-dissociation of formamide [161], indicating that HCN and H<sub>2</sub>O, if produced, are very reactive.

### **3.5 Lyman- $\alpha$ Processing of Water:Formamide Mixed Ices on SiO<sub>2</sub>**

#### **3.5.1 Results**

##### 3.5.1.1 IR Spectra After Lyman- $\alpha$ Irradiation of Mixed H<sub>2</sub>O:HCONH<sub>2</sub> Ices on SiO<sub>2</sub> at 70 K

Over the time of the irradiation experiments (72 hr), a background water dose (at a chamber pressure of  $\sim 2 \times 10^{-9}$  Torr after dosing formamide) of about 518 L could deposit as an uppermost layer on the pure formamide ice. Significant water bands did not grow in the IR spectrum (Figure 3.8); however, a band at 1600 cm<sup>-1</sup> (possibly H<sub>2</sub>O) did appear upon warm-up (at  $\sim 210$  K) both with and without prior irradiation (Figures 3.1 and 3.11A). Because of the possible background H<sub>2</sub>O dose in the pure formamide irradiation experiments with time and because H<sub>2</sub>O dominates interstellar ices, the direct effects of water on the product formation have been studied by irradiating pre-dosed mixed H<sub>2</sub>O:HCONH<sub>2</sub> ices (0.75:1 and 2:1 mixtures). Shown in Figure 3.15 below are the infrared spectra of the OCN<sup>-</sup> and CO peaks produced with Lyman- $\alpha$  irradiation of a 1100 L H<sub>2</sub>O:550 L HCONH<sub>2</sub> (2:1) mixed ice. The OCN<sup>-</sup> and CO were again the main products seen upon irradiation. However, their yields in a H<sub>2</sub>O:HCONH<sub>2</sub> mixture are different compared to pure HCONH<sub>2</sub> ice and are discussed in Section 3.5.2.1 below.

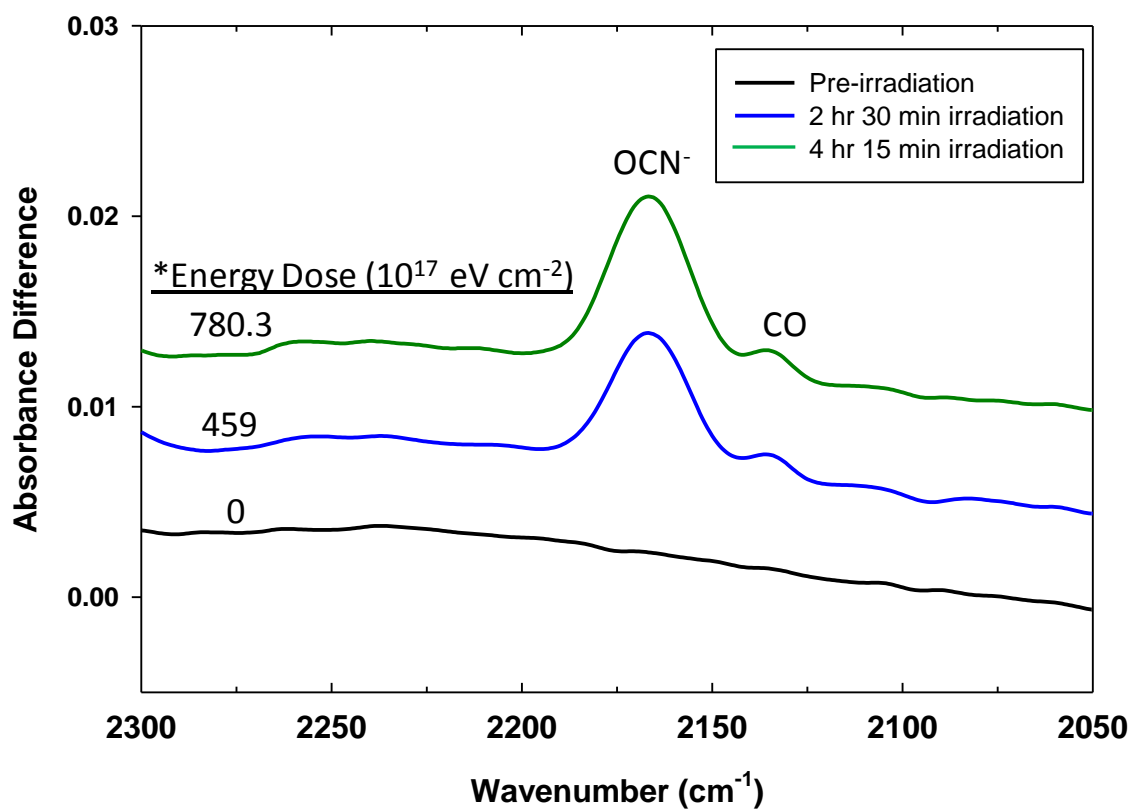


**Figure 3.15:** Infrared spectra of OCN<sup>-</sup> and CO production upon Lyman- $\alpha$  irradiation of a 2:1 mixture of H<sub>2</sub>O:HCONH<sub>2</sub> at 70 K, showing that the same products are produced with a mixed water ice as with pure formamide. Comparison to pure HCONH<sub>2</sub> ice is discussed in Section 3.5.2.1.

## 3.5.2 Discussion

### 3.5.2.1 Column Density Comparisons Between Pure and Mixed H<sub>2</sub>O:HCONH<sub>2</sub> Ices After Lyman- $\alpha$ Irradiation

Table 3.2 below compares calculated column densities ( $N$ ) of pure HCONH<sub>2</sub> to the mixed H<sub>2</sub>O:HCONH<sub>2</sub> ices for the 1388 cm<sup>-1</sup> band of formamide, the OCN<sup>-</sup> band, and the CO band before and after 3 hr irradiation. All reported  $N$ s have been normalized by multiplying the original  $N$  by a ratio (obtained by dividing the initial pure HCONH<sub>2</sub>  $N$  by the mixed-water ice  $N$ ). Also note the  $A$ , or band strength, used may be a source of error since they were not determined in mixed-water ices. As expected, the 1388 cm<sup>-1</sup> band decreased after 3 hr Lyman- $\alpha$  irradiation, compared to before irradiation, regardless of the presence of water. The OCN<sup>-</sup> band column density increases with increased water concentration, from  $1.62 \times 10^{15}$  to  $3.18 \times 10^{15}$  molecules/cm<sup>2</sup>. Finally, the CO band is also increased after irradiation when water is present in the ice (from  $2.73 \times 10^{15}$  to  $5.39 \times 10^{15}$  molecules/cm<sup>2</sup>). The formation yield of CO produced is slightly more than the yield of OCN<sup>-</sup> when water is present. The results suggest that OCN<sup>-</sup> and CO yields relate mechanistically to the presence of H<sub>2</sub>O, and CO production may even be catalyzed by water's presence if formamide is ionized by the irradiation [162]. Indeed, calculations have suggested that the barrier for the formamide to dissociate goes down by nearly a factor of two when two waters couple to a formamide molecule [163], which is in agreement with the 2:1 mixed ice results shown here. It has also been mentioned that one decomposition channel from pure HCONH<sub>2</sub> is to H<sub>2</sub>O + HCN [61], which then can further lead to OCN<sup>-</sup> [115]. If some background water is dosed during the pure HCONH<sub>2</sub> irradiation experiments, it could increase the production rate of OCN<sup>-</sup> and CO, although it

is difficult to tell by how much since there will always be some background dosing even at  $10^{-9}$  to  $10^{-10}$  Torr. It can also be inferred that interstellar regions (that contain water-formamide icy grains) could show an increased amount of  $\text{OCN}^-$ . However, a more detailed study involving different water:formamide concentrations (and accurately determined band strengths) would be beneficial to further understand the effects of water on formamide photochemistry.

**Table 3.2:** Normalized column densities<sup>a</sup> ( $N$ ) of  $1388\text{ cm}^{-1}$  formamide,  $\text{OCN}^-$ , and CO bands upon  $\sim 3$  hr irradiation of pure  $\text{HCONH}_2$  ice compared to 0.75:1 and 2:1  $\text{H}_2\text{O}:\text{HCONH}_2$  mixed ices.

Ice Composition	$1388\text{ cm}^{-1}$ band <sup>b</sup> of $\text{HCONH}_2$ before irradiation	$1388\text{ cm}^{-1}$ band <sup>b</sup> of $\text{HCONH}_2$ after Lyman- $\alpha$ irradiation	$2163\text{ cm}^{-1}$ band <sup>c</sup> of $\text{OCN}^-$ after Lyman- $\alpha$ irradiation	$2135\text{ cm}^{-1}$ band <sup>d</sup> of CO after Lyman- $\alpha$ irradiation
Pure $\text{HCONH}_2$	$2.11 \times 10^{17}$	$1.85 \times 10^{17}$	$1.62 \times 10^{15}$	$2.73 \times 10^{15}$
<sup>e</sup> 0.75:1 $\text{H}_2\text{O}:\text{HCONH}_2$	$2.11 \times 10^{17}$	$2.0 \times 10^{17}$	$2.44 \times 10^{15}$	$2.75 \times 10^{15}$
<sup>f</sup> 2:1 $\text{H}_2\text{O}:\text{HCONH}_2$	$2.11 \times 10^{17}$	$1.96 \times 10^{17}$	$3.18 \times 10^{15}$	$5.39 \times 10^{15}$

<sup>a</sup>Column densities in units of molecules/ $\text{cm}^2$

<sup>b</sup>Calculated using band strength,  $A = 0.68 \times 10^{-17}$  cm/molecules as reported by Brucato et al. [24]

<sup>c</sup>Calculated using band strength,  $A = 1.3 \times 10^{-16}$  cm/molecules as reported by Raunier et al. [144]

<sup>d</sup>Calculated using band strength,  $A = 1.1 \times 10^{-17}$  cm/molecules as reported by Gerakines et al. [145]

<sup>e</sup>Normalized by multiplying original ( $N$ )s by 1.51

<sup>f</sup>Normalized by multiplying original ( $N$ )s by 1.48

## 3.6 Electron Irradiation of Pure Formamide and Water:Formamide Mixed Ices on SiO<sub>2</sub>

### 3.6.1 Results

#### 3.6.1.1 IR Spectral Comparison After 1 keV Electron Irradiation of Pure HCONH<sub>2</sub> and Mixed H<sub>2</sub>O:HCONH<sub>2</sub> Ices on SiO<sub>2</sub> at 70 K

The 1 keV electron irradiation of pure HCONH<sub>2</sub> and H<sub>2</sub>O:HCONH<sub>2</sub> mixed ice was performed to compare with Lyman- $\alpha$  irradiation. Figure 3.16 below shows the two product bands of interest: OCN<sup>-</sup> and CO. These are the only two products again observed in the IR spectra. The infrared spectra after electron irradiation have been normalized to the initial concentrations of formamide in each ice prior to irradiation. Electrons do not appear to form CO (black and blue spectra), and this is consistent with the lack of area for this peak which leads to a lack of column density for CO after electron irradiation (see Table 3.6), even with the presence of water. However, OCN<sup>-</sup> is produced after electron irradiation, similar to photon irradiation. In the water mixture, the OCN<sup>-</sup> band is slightly blue shifted compared to the irradiated pure formamide. The OCN<sup>-</sup> band also has a slightly higher intensity after electron irradiation, compared to Lyman- $\alpha$  irradiation. For a quantitative comparison using the normalized column densities and comparison with water, see Section 3.6.2.1 below.

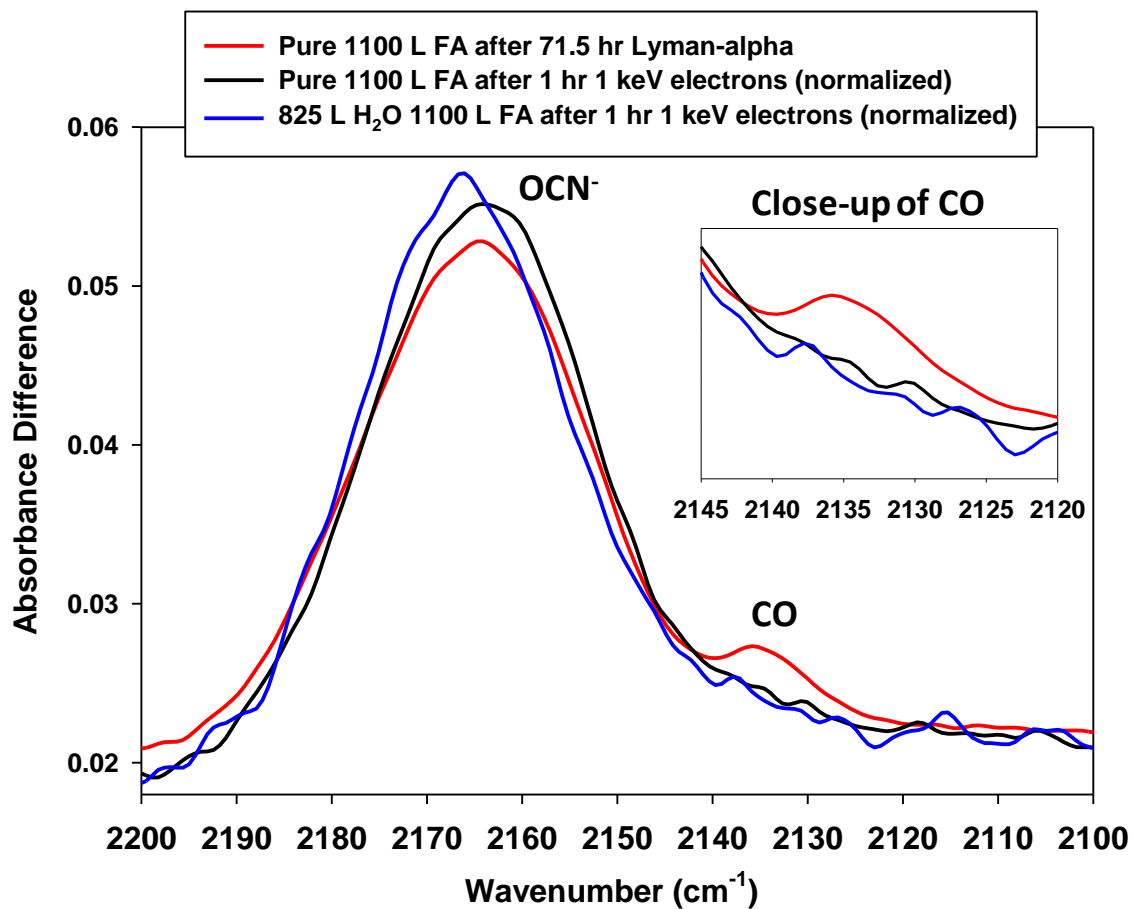


**Figure 3.16:** Infrared spectral comparison of OCN<sup>-</sup> and CO bands for pure HCONH<sub>2</sub> (FA) after 71.5 hr Lyman- $\alpha$  irradiation (red), pure HCONH<sub>2</sub> after 1 hr of 1 keV electron irradiation (black), and 0.75:1 H<sub>2</sub>O:HCONH<sub>2</sub> after 1 hr of 1 keV electron irradiation (blue). The two electron irradiation spectra have been normalized to the initial formamide concentrations in each ice by multiplying the spectra by 1.99 (black) and 3.51 (blue). Inset is close-up of the CO band.

### 3.6.2 Discussion

#### 3.6.2.1 Column Density Comparisons Between Electron Irradiation and Lyman- $\alpha$ Irradiation of Pure and Mixed H<sub>2</sub>O:HCONH<sub>2</sub> Ices on SiO<sub>2</sub> at 70 K

As described in Section 3.6.1.1, pure HCONH<sub>2</sub> and mixed H<sub>2</sub>O:HCONH<sub>2</sub> ices were irradiated with 1 keV electrons to compare the products with Lyman- $\alpha$  photon irradiation. Table 3.3 below provides the calculated irradiation doses on an eV/formamide molecule basis for the total times of the experiments. The eV/molecule doses are found to be comparable to those received in interstellar regions [28].

**Table 3.3:** Comparison of Lyman- $\alpha$  and electron irradiation total energy doses on an eV/formamide molecule basis for pure HCONH<sub>2</sub> and 0.75:1 H<sub>2</sub>O:HCONH<sub>2</sub> mixed ice. See text for explanation of calculation.

Ice Composition	3 hr Lyman- $\alpha$	71.5 hr Lyman- $\alpha$	1 hr 1 keV electrons
Pure HCONH <sub>2</sub>	$2.48 \times 10^3$	$5.90 \times 10^4$	$5.26 \times 10^2$
0.75:1 H <sub>2</sub> O:HCONH <sub>2</sub>	$5.1 \times 10^3$	$1.21 \times 10^5$	$1.3 \times 10^4$

The doses ( $D_{irr}$ ) shown in Table 3.3 were calculated using the formula [29]

$$D_{irr} = \frac{[\langle E_{irr} \rangle \phi_{abs} t]}{N_o}$$

where  $\langle E_{irr} \rangle$  is the average energy in units of eV/photon or eV/electron,  $\phi_{abs}$  is equal to the absorbed photon flux in photons cm<sup>-2</sup> s<sup>-1</sup> ( $\sim 2.7 \times 10^{14}$ ) assuming all photons are absorbed or the electron current density in electrons cm<sup>-2</sup> s<sup>-1</sup> ( $\sim 10^{14}$ ),  $t$  is equal to time of irradiation (s), and  $N_o$  is the column density of formamide at time = 0 in units of molecules/cm<sup>2</sup>. Because the concentrations of formamide at time = 0 for different experiments can be different, the H<sub>2</sub>O:HCONH<sub>2</sub> mixtures give different energy doses

compared to pure HCONH<sub>2</sub> experiments. An average  $N_o$  was obtained for each based on two different bands of formamide (1388 cm<sup>-1</sup> and 1325 cm<sup>-1</sup>) and their respective band strengths ( $A = 0.68 \times 10^{-17}$  cm mol<sup>-1</sup> and  $A = 0.85 \times 10^{-17}$  cm mol<sup>-1</sup>) [24]. This is a potential source of error because these are reported for pure ices, and the  $A$  could change in a mixed ice. That  $N_o$  for each experiment was then divided by 2, since only one side of the sample was irradiated and then multiplied by a ratio (the penetration depth of the electrons or photons divided by the total thickness of the ice) to provide the corrected  $N_o$  based on the depth of the ice irradiated. The estimated penetration depths were 56 nm for 1 keV [164], and ~100 nm for Lyman- $\alpha$  [146]. The penetration depths of electrons in the pure HCONH<sub>2</sub> ice and the H<sub>2</sub>O:HCONH<sub>2</sub> ice were both estimated to be ~56 nm, based on calculations from CASINO “Monte Carlo Simulation of electron trajectory in solid” software [164]. In addition, for the electron experiments where the sample was rastered about 12 times over the sample per 1 hr, based on the irradiation spot size of ~1.5 mm diameter and the sample size of 3.75 cm<sup>2</sup>, it was determined that each spot was irradiated for 17.3 s, which gives  $t$  in the above equation for the electron experiments. The resulting doses are shown in Table 3.3 and are in units of eV/molecule. These results show that for 71.5 hr Lyman- $\alpha$  irradiation the pure HCONH<sub>2</sub> ice receives 112 times (% increase) the energy dose in eV/molecule than for 1 hr of 1 keV electron irradiation. This makes sense since the e-gun is rastered over the entire sample and thus less total dose is received in the time of the experiment. In addition, the total doses in eV/molecule are higher for the mixed H<sub>2</sub>O:HCONH<sub>2</sub> ices. This is because the dilution of formamide means that fewer HCONH<sub>2</sub> molecules are available to the electrons and so the eV/formamide molecule total dose of radiation is higher.

The normalized calculated column densities ( $N$ ) for the  $1388\text{ cm}^{-1}$  formamide band are given below in Table 3.4. This band is expected to decrease in intensity ( $N$  should also decrease) upon irradiation, as shown previously. Indeed, it was shown that there was a decrease from  $2.11 \times 10^{17}$  to  $1.5 \times 10^{17}$  molecules/cm<sup>2</sup> upon 71.5 hr Lyman- $\alpha$  irradiation. After electron irradiation, the column density of the band is slightly larger as expected ( $1.66 \times 10^{17}\text{ cm}^{-2}$ ), considering the total energy dose difference (112x less) and less formamide is processed. Also, a comparison of the two electron irradiation experiments shows that even less formamide is lost with the H<sub>2</sub>O:HCONH<sub>2</sub> mixture than with electron irradiation of the pure HCONH<sub>2</sub> ice, although this would need to be confirmed with more data (and more accurate  $A$ s for mixed ices) in a future study. Formamide does not seem to desorb or transform into products as easily when electrons irradiate a mixed H<sub>2</sub>O:HCONH<sub>2</sub> ice.

**Table 3.4:** Comparison of normalized column densities<sup>x</sup> ( $N$ ) of  $1388\text{ cm}^{-1}$  formamide band<sup>y</sup> for pure HCONH<sub>2</sub> and 0.75:1 H<sub>2</sub>O:HCONH<sub>2</sub> mixed ice with Lyman- $\alpha$  irradiation compared to electron irradiation.

Ice Composition	Before Irradiation	After 3 hr Lyman- $\alpha$	After 71.5 hr Lyman- $\alpha$	After 1 hr 1 keV electrons
Pure HCONH <sub>2</sub>	$2.11 \times 10^{17}$	$1.85 \times 10^{17}$	$1.5 \times 10^{17}$	<sup>a</sup> $1.66 \times 10^{17}$
0.75:1 H <sub>2</sub> O:HCONH <sub>2</sub>	<sup>b</sup> $2.11 \times 10^{17}$	<sup>b</sup> $2.0 \times 10^{17}$	No experiment	<sup>c</sup> $2.0 \times 10^{17}$

<sup>x</sup>Column densities in units of molecules/cm<sup>2</sup>

<sup>y</sup>Calculated using band strength,  $A = 0.68 \times 10^{-17}$  cm/molecules as reported by Brucato et al. [24]

<sup>a</sup>Normalized by multiplying original ( $N$ ) by 1.99

<sup>b</sup>Normalized by multiplying original ( $N$ ) by 1.51

<sup>c</sup>Normalized by multiplying original ( $N$ ) by 3.51

The normalized column densities of the OCN<sup>-</sup> product band are provided in Table 3.5 below. When the column density after 71.5 hr Lyman- $\alpha$  irradiation for pure HCONH<sub>2</sub> ( $1.1 \times 10^{16}$  molecules/cm<sup>2</sup>) is compared to the column density after electron irradiation ( $1.29 \times 10^{16}$  molecules/cm<sup>2</sup>), it is clear that even though 112x less eV/formamide molecule dose occurs in the electron experiment, the OCN<sup>-</sup> formation is as efficient, and even slightly more so, than with photons. This may suggest a dissociative electron attachment (DEA) mechanism as discussed previously. Even more interesting, electron irradiation of the H<sub>2</sub>O:HCONH<sub>2</sub> mixed ice, produces even more OCN<sup>-</sup> ( $1.38 \times 10^{16}$  molecules/cm<sup>2</sup>) than either photon or electron irradiation of the pure HCONH<sub>2</sub>.

**Table 3.5:** Comparison of normalized column densities<sup>x</sup> ( $N$ ) of 2163 cm<sup>-1</sup> OCN<sup>-</sup> band<sup>y</sup> for pure HCONH<sub>2</sub> and 0.75:1 H<sub>2</sub>O:HCONH<sub>2</sub> mixed ice with Lyman- $\alpha$  irradiation compared to electron irradiation.

Ice Composition	After 3 hr Lyman- $\alpha$	After 71.5 hr Lyman- $\alpha$	After 1 hr 1 keV electrons
Pure HCONH <sub>2</sub>	$1.62 \times 10^{15}$	$1.1 \times 10^{16}$	<sup>a</sup> $1.29 \times 10^{16}$
0.75:1 H <sub>2</sub> O:HCONH <sub>2</sub>	<sup>b</sup> $2.44 \times 10^{15}$	No experiment	<sup>c</sup> $1.38 \times 10^{16}$

<sup>x</sup>Column densities in units of molecules/cm<sup>2</sup>

<sup>y</sup>Calculated using band strength,  $A = 1.3 \times 10^{-16}$  cm/molecules as reported by Raunier et al. [144]

<sup>a</sup>Normalized by multiplying original ( $N$ ) by 1.99

<sup>b</sup>Normalized by multiplying original ( $N$ ) by 1.51

<sup>c</sup>Normalized by multiplying original ( $N$ ) by 3.51

Finally, Table 3.6 below gives the column density of the CO band after Lyman- $\alpha$  irradiation; however, there were no CO peaks observed (no area of CO) with electron irradiation in either the pure HCONH<sub>2</sub> or H<sub>2</sub>O:HCONH<sub>2</sub> mixed ice. This is consistent

with Figure 3.16 given in Section 3.6.1.1, and suggests a different mechanistic pathway is followed upon electron irradiation that does not involve decarboxylation.

**Table 3.6:** Comparison of normalized column densities<sup>x</sup> ( $N$ ) of 2135  $\text{cm}^{-1}$  CO band<sup>y</sup> for pure  $\text{HCONH}_2$  and 0.75:1  $\text{H}_2\text{O}:\text{HCONH}_2$  mixed ice with Lyman- $\alpha$  irradiation compared to electron irradiation.

Ice Composition	After 3 hr Lyman- $\alpha$	After 71.5 hr Lyman- $\alpha$	After 1 hr 1 keV electrons
Pure $\text{HCONH}_2$	$2.73 \times 10^{15}$	$1.27 \times 10^{16}$	-
0.75:1 $\text{H}_2\text{O}:\text{HCONH}_2$	<sup>a</sup> $2.75 \times 10^{15}$	No experiment	-

<sup>x</sup>Column densities in units of molecules/ $\text{cm}^2$

<sup>y</sup>Calculated using band strength,  $A = 1.1 \times 10^{-17}$  cm/molecules as reported by Gerakines et al. [145]

<sup>a</sup>Normalized by multiplying original ( $N$ ) by 1.51

Overall, these results indicate that with electron irradiation there is slightly more  $\text{OCN}^-$  produced and no CO produced, compared to Lyman- $\alpha$  irradiation. If water is mixed in the ice and electron irradiated, the yield of  $\text{OCN}^-$  is further increased while there is no change in CO production. Thus, both with electron and Lyman- $\alpha$  irradiation, water increases the  $\text{OCN}^-$  formation. Further studies should involve varying the concentrations of water to formamide, more accurately determining band strengths in mixed water-formamide ices, and several repetitions of the different experiments to more accurately determine the column densities for comparison.

### 3.7 Conclusions

The adsorption and subsequent warm-up of formamide ices on high-surface-area SiO<sub>2</sub> nanopowder has been observed with transmission FT-IR and TPD from 70 to 460 K. In addition, Lyman- $\alpha$  and electron irradiation of HCONH<sub>2</sub> and H<sub>2</sub>O:HCONH<sub>2</sub> mixed ices was investigated. From this work, the following conclusions are made.

1. A first phase ice layer (likely porous) is formed upon adsorption of pure formamide on the substrate at 70 K.
2. A re-organization (crystallization) in the ice occurs upon warming to  $\sim$ 145 K.
3. Formamide begins desorption from the SiO<sub>2</sub> surface near 220 K with slow diffusion preventing complete desorption until  $\sim$ 460 K. The mean binding energy has been calculated to be  $14.7 \pm 0.17$  kcal/mol ( $0.64 \pm 0.007$  eV).
4. Upon photolysis of pure HCONH<sub>2</sub> 70 K and 165 K annealed ices, OCN<sup>-</sup> and CO are detected with IR spectroscopy. The yields of OCN<sup>-</sup> and CO largely depends upon the molecular arrangement of the formamide ice, with a definite decrease ( $\sim$ 25%) in combined integrated peak area seen for ice annealed to 165 K prior to irradiation. Because desorption does not begin until  $\sim$ 220 K, this decrease is correlated with the specific ice geometry formed upon warm-up to 165 K.
5. Formamide also partially dissociates and is consumed during Lyman- $\alpha$  irradiation producing free H<sub>2</sub> that is likely trapped in the ice during irradiation. This dissociation could be assisted by the SiO<sub>2</sub> surface. TPD also indicates that some re-forming of formamide may occur in the ice during irradiation.

6. Ice that has been annealed to 165 K prior to irradiation shows less H<sub>2</sub> formation, consistent with the lower OCN<sup>-</sup> and CO products relative to unannealed samples.
7. Formamide ice that is mixed with water and irradiated with Lyman- $\alpha$  shows an increased yield in both OCN<sup>-</sup> and CO, possibly indicating a catalytic effect. Electron irradiation, even though a much lower total energy dose, produces an increased yield of OCN<sup>-</sup> from pure formamide suggesting a DEA pathway may be invoked. However, no CO is produced with electron irradiation. When water is mixed with formamide and electron irradiated, the OCN<sup>-</sup> further increases while CO does not. This suggests that decarboxylation does not occur as readily with electron irradiation. These interesting results warrant further studies.

In summary, the slow production of OCN<sup>-</sup> and CO with Lyman- $\alpha$  photolysis and electron irradiation and the lack of other larger products supports a recent theoretical report [165] on the stability of formamide's peptide bond. Formamide's stability may be why it has been detected in energetically processed interstellar regions even in small abundances. In addition, the main products seen here suggest very different condensed-phase dissociation channels from those reported for gas-phase dissociation [61,158,166]. However, we have shown here that formation of ions/products from formamide is not negligible upon Lyman- $\alpha$  photolysis [122] or electron irradiation. Condensed-phase photochemical calculations of formamide would be very beneficial to compare with previous gas-phase studies and to further elucidate the reactions of formamide ice in the interstellar medium.

## CHAPTER IV

### THERMAL AND RADIATION STUDIES OF PURE AND MIXED ICES RELEVANT TO TITAN'S CHEMISTRY

#### 4.1 Introduction

Titan is the largest moon of Saturn that has been considered by some as a present-day prebiotic planetary body [27] that could give us clues about Earth's molecular evolution. The observation of organic-rich rivers and lakes on Titan by the Cassini-Huygens mission has generated much interest about possible prebiotic reactions occurring at the surface and in the atmosphere. Titan is the only other known world to carry liquids on the surface [26]. The atmosphere consists mostly of N<sub>2</sub> (~95-98%), CH<sub>4</sub> (~1.8-5%), H<sub>2</sub> (0.1-0.2%), CO (0.005%) [26], but trace amounts of other organics are present [10,167]. Titan is unique in the solar system because it has active weather patterns similar to Earth, albeit it has a methanological cycle (methane-based) unlike Earth's hydrological cycle (water-based) [26]. In addition, the pressures on Titan are 0.07-1,125 Torr, compared to Earth's ~760 Torr [26]. Titan's surface temperature is a chilly ~94 K, which means that surface chemistry must come from energy sources such as cosmic rays, impacts, cryovolcanism, meteorology, or acetylene cyclization to benzene [25]. However, temperatures can reach as high as 175 K in the upper atmosphere, and exogenous and endogenous energy sources can initiate reactions of organics in the atmosphere that then rain down onto the surface for possible further processing by, for

example, cryovolcanism [26]. See Figure 4.1 below for the sources of energy deposition in Titan's atmosphere and on its surface, adapted from Krasnopolsky [3]. Thus, the organic chemistry of the atmosphere and surface of Titan can be quite complex due to the different irradiation sources and organics present.

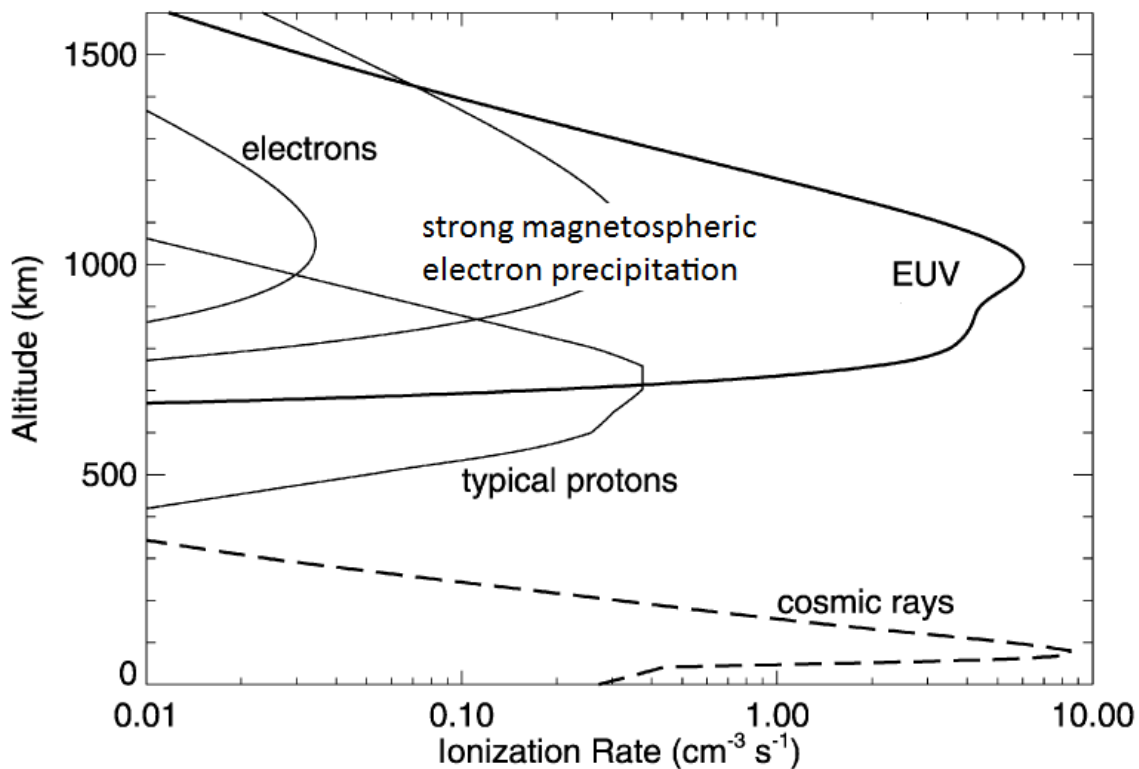


**Figure 4.1:** Deposition of energy affecting Titan's chemistry (EUV, electrons, ions, etc.) as a function of altitude. Adapted from Krasnopolsky [3] with permission (Copyright 2009) from Elsevier.

The main sources of cosmic rays and x-rays in the atmosphere of Titan are the Saturnian magnetosphere as well as the solar wind [25]. Secondary low-energy electrons from cosmic rays are known to be present at low altitudes and in the near surface regions. At altitudes of 1200 km, the electron flux has been estimated to be  $10^2$ - $10^5$   $\text{cm}^{-2}\text{s}^{-1}$   $\text{eV}^{-1}$  with energies in the range of 0.1-1 keV [168], and at lower altitudes appreciable electron densities were measured by the Huygens Probe [169]. Solar extreme-ultraviolet and Lyman- $\alpha$  radiation also penetrate into Titan's haze down to about 700 km where cold organic-laden aerosol clouds exist [25]. Thus, exploring the reactions of mixed hydrocarbon ices with electron and photon irradiation can help unravel complicated organic mechanisms, and this may be crucial to determining Titan's role as a prebiotic chemical system in the outer solar system. Few laboratory-based studies have performed such irradiation experiments at low enough temperatures to mimic Titan's chemical environment [26].

Acetonitrile ( $\text{CH}_3\text{CN}$ ) has been detected in the upper atmosphere and stratosphere of Titan by the international 30 meter radio telescope in the Spanish Sierra Nevada (operated by IRAM) and on the surface in dark terrain regions by Cassini's Visual and Infrared Mapping Spectrometer (VIMS) [10]. Acetonitrile is of interest chemically because of the potentially reactive nitrile or cyano- group.  $\text{CH}_4$  and  $\text{HCN}$  have been shown to form from UV and proton irradiation of  $\text{CH}_3\text{CN}$  by Hudson and Moore [170]. Both  $\text{CH}_4$  and  $\text{HCN}$  are known to be active molecules in prebiotic Miller-Urey spark discharge-type experiments [126]. In addition,  $\text{CH}_3\text{CN}$ 's electron-induced reactions have been explored in condensed films resulting in radical chain reactions and recombination products when mixed with ethane [171]. Thus,  $\text{CH}_3\text{CN}$ 's chemistry with other organics

relevant to Titan is of interest.

Acetylene ( $C_2H_2$ ) is an interesting starting molecule that could lead to larger polymerization [172]. It has been proposed to be generated in a  $CH_4/N_2$  atmosphere, which is consistent with Titan's atmosphere [172].  $C_2H_2$  has been detected in the atmosphere of Titan by the Composite Infrared Spectrometer (CIRS) and the Ion and Neutral Mass Spectrometer (INMS) aboard the Cassini spacecraft [10], but it is mostly absent from the surface probably because of atmospheric processing by cosmic rays [25]. It could undergo polymerization to PAHs (polyaromatic hydrocarbons) and polyynes (diacetylene, etc.) during freeze-melt cycles of the atmospheric aerosols [172]. For example, Zhou, Zheng, and Kaiser et al. have shown that benzene forms from pure  $C_2H_2$  ices under high energy electron bombardment [167], and this acetylene cyclization to benzene is thought to be a major source of energy for surface chemistry on Titan, as mentioned above [25].

Although the chemistry of the pure organics themselves may not be prebiotic in nature, when different organics are irradiated together, the chemistry can become quite interesting. For example, the reactions of mixed or layered  $CH_3CN/C_2H_2$  ices upon irradiation could form cyanoacetylene ( $C_3HN$ ), which could explain its presence in Titan's atmosphere [10]. Cyanoacetylene is of interest because it is one of the molecules that has been produced in spark discharge Miller-Urey type-experiments from  $CH_4$  and  $N_2$  [7]. Also, if cyanate ( $OCN^-$ ) is added to cyanoacetylene, cytosine can be formed which is one of the main nucleobases of DNA [7]. In addition, since  $C_3HN$  and  $CH_3CN$  along with benzene have been found in near-IR spectra of Titan's surface, but  $C_2H_2$  is mostly absent from the surface, laboratory-based studies of the reactions between  $CH_3CN$

and C<sub>2</sub>H<sub>2</sub> could help our understanding of the possible consumption of C<sub>2</sub>H<sub>2</sub> (and possibly H<sub>2</sub>) on the surface. Thus, the main goals of this work include: 1) the electron irradiation of pure C<sub>2</sub>H<sub>2</sub> and pure CH<sub>3</sub>CN to determine their decomposition products, and 2) the electron irradiation of mixed C<sub>2</sub>H<sub>2</sub>:CH<sub>3</sub>CN to look for product formation. H<sub>2</sub>O and CO<sub>2</sub> are also added to the pure or mixed ices for some TPD experiments since these are also found in trace amounts in Titan's atmosphere and surface [10]. Lyman- $\alpha$  irradiation experiments are performed for comparison, as well as thermal studies to simulate reactions upon heating in the atmosphere or due to cryovolcanism on the surface. Reactions on a SiO<sub>2</sub> surface are undertaken to simulate interactions with catalytic mineral particulate surfaces resulting from meteorite impact on Titan's surface.

## 4.2 Experimental Details

The custom-built UHV experimental chamber shown in Figure 2.1 and described in Chapters 2 and 3 was again used for this study. Briefly, the chamber is coupled to two radiation sources, a Lyman- $\alpha$  lamp (10.2 eV) and a pulsed e-gun (5-1000 eV). The e-gun has a typical current density of  $10^{14}$  electrons cm<sup>-2</sup> s<sup>-1</sup> and a beam spot size of ~1.5 mm. It can be rastered over the sample area of 3.75 cm<sup>2</sup> in ~5 min. The photon flux of the Lyman- $\alpha$  lamp is  $\sim 2.7 \times 10^{14}$  photons s<sup>-1</sup> cm<sup>-2</sup>. The sample is rotatable and can be faced normal to either radiation source. The UHV ( $1 \times 10^{-10}$  Torr) chamber is equipped with a quadrupole mass spectrometer (QMS) for performing TPD measurements using a linear temperature ramp controlled by a custom Labview program. The UHV chamber is also coupled to transmission FT-IR spectroscopy for *in-situ* measurements before and after irradiation. This was described in detail in Chapters 2 and 3.

For some experiments, the sample substrate was an inert vapor-deposited gold on a small tantalum 0.01 inch sheet. This substrate was prepared in a separate vacuum chamber that was evacuated to ( $1 \times 10^{-6}$  Torr). An adhesion layer of 40 nm of titanium was evaporated first at a rate of  $3 \text{ \AA s}^{-1}$ . Then, 300 nm of gold was deposited on the adhesion layer at a rate of  $3 \text{ \AA s}^{-1}$ . This gold inert substrate (on tantalum) was then spot-welded to the tantalum strips of the sample holder. This substrate was used for the *layered* pure and mixed ice post-irradiation TPD experiments. Layering of the ices and irradiation between them was performed to counteract the shallow penetration depth of low-energy electrons ( $<60 \text{ nm}$ ) [151] by potentially increasing the number density of products. Additional experiments on  $\text{SiO}_2$  nanopowder were also performed using the sample mount depicted in Figure 2.2 of Chapter 2. The sample preparation for  $\text{SiO}_2$  nanopowder was described in Chapter 3. Because of the high transmission of the  $\text{SiO}_2$  surface on the transparent tungsten mesh, clean transmission IR measurements could be obtained of the ices vapor-deposited on the powder. TPD and post-irradiation TPD could also be performed on the ice-covered  $\text{SiO}_2$  samples. The organics adsorbed on the cold inert gold substrate could be heated and cooled from  $\sim 40\text{-}800 \text{ K}$ . However, the temperature range for the  $\text{SiO}_2$  substrate was from  $\sim 70\text{-}800 \text{ K}$ .

Anhydrous acetonitrile ( $\text{CH}_3\text{CN}$ ) was purchased from Sigma-Aldrich (99.8%), and  $\text{D}_2$ -acetylene ( $\text{C}_2\text{D}_2$ ) gas was purchased from Cambridge Isotope Laboratories, Inc (99%). The  $\text{C}_2\text{D}_2$  was chosen to distinguish deuterium loss from hydrogen loss (from  $\text{CH}_3\text{CN}$ ) in the mixed ices.  $\text{CH}_3\text{CN}$  and  $\text{C}_2\text{D}_2$  pure ices and  $\text{CH}_3\text{CN}/\text{C}_2\text{D}_2$  layered or mixed ices were deposited on the substrate. Co-dosing was achieved by using separate precision leak valves and measuring the pressure of each gas

during dosing. For example, for a 0.75:1 mixture of CH<sub>3</sub>CN:C<sub>2</sub>D<sub>2</sub>, 825 L of CH<sub>3</sub>CN was deposited by opening the leak valve for that vapor to achieve a pressure of  $7.5 \times 10^{-7}$  Torr in the chamber (0.75 L/s). The second leak valve was then opened to the C<sub>2</sub>D<sub>2</sub> vapor so that a pressure of  $1 \times 10^{-6}$  Torr was achieved in the chamber (1 L/s) and 1100 L of C<sub>2</sub>D<sub>2</sub> was dosed. Once the appropriate time of dosing (18 min + 20 s) had elapsed to achieve those coverages, both leak valves were closed simultaneously. There is a certain amount of dosing error (<5%) that can occur with this method using ion gauges to measure the pressure. Based on the density of acetylene ice (1 g/cm<sup>3</sup>) and CH<sub>3</sub>CN ice (0.8 g/cm<sup>3</sup>), the maximum thickness of C<sub>2</sub>D<sub>2</sub> is estimated to be ~512 nm while CH<sub>3</sub>CN is ~702 nm, giving a total thickness of ~1214 nm for a 1:0.75 C<sub>2</sub>D<sub>2</sub>:CH<sub>3</sub>CN mixed ice. For a 1:0.75 C<sub>2</sub>D<sub>2</sub>:CH<sub>3</sub>CN mixed ice, the “Monte Carlo Simulation of electron trajectory in solid” (CASINO) [164] program was used to determine the electron penetration depths for the electron irradiation experiments. For 1 keV electrons, maximum penetration depth is ~51 nm, and for 400 eV electrons, depth is ~12 nm. Distilled H<sub>2</sub>O and CO<sub>2</sub> gas (purchased from Matheson Tri-Gas, 99%) were also used in some mixed ice TPD experiments.

The experiments were performed as follows. Pure and mixed ices were dosed and irradiated with low-energy electrons (70-1000 eV) or Lyman- $\alpha$  irradiation (10.2 eV). IR spectra were obtained before irradiation. Irradiation with electrons was performed in some cases between dosed layers since the penetration depth of low-energy electrons is shallow [151] and to facilitate build-up of products. After irradiation, reaction products were studied by obtaining post-irradiation TPD and post-irradiation IR. In some cases, IR spectra were recorded upon warm-up of the ices. For TPD, linear ramp rates of

0.05-1 K/s were employed. Some experiments did not involve irradiation, and the ices were simply dosed and TPD was performed.

### 4.3 Results

#### 4.3.1 TPD of H<sub>2</sub> From Electron Irradiation of Pure Acetonitrile (CH<sub>3</sub>CN) on Au

The desorption temperature of CH<sub>3</sub>CN starts at ~120 K and ends by 160 K with a maximum desorption at ~140 K, and its fragments due to electron ionization in the QMS would normally desorb in the same temperature range. Without irradiation, there is no H<sub>2</sub> desorption with CH<sub>3</sub>CN. However, electron-irradiation between 4 pure 1 L CH<sub>3</sub>CN ice layers (10 min of 100 eV between each) produces H<sub>2</sub> (mass 2), as shown by the TPD of m/z 2 in Figure 4.2 below. H<sub>2</sub> begins desorbing almost immediately (45 K) upon heating and continues until 120 K. Larger molecular weight products were not observed in this desorption experiment.

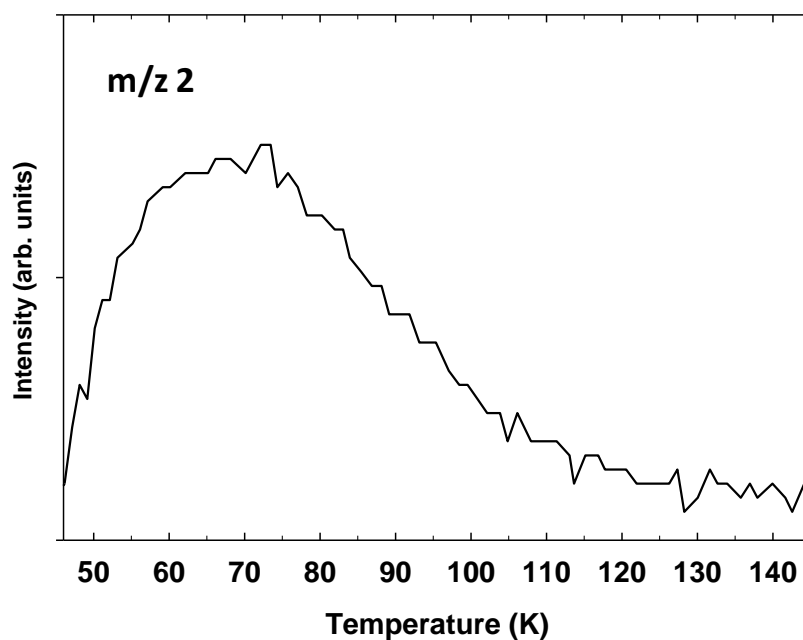


**Figure 4.2:** Post-irradiation TPD of  $m/z$  2 ( $H_2$ ) for layered  $CH_3CN$  ice (1 L x 4) after deposition at 40 K and then 100 eV electron irradiation for 10 minutes. The background TPD of  $m/z$  2 from  $CH_3CN$  (non-irradiated) has been subtracted out. Ramp rate = 0.05 K/s.

### 4.3.2 TPD of CH<sub>4</sub>, HCN, CH<sub>3</sub>CN From Electron Irradiation of Pure CH<sub>3</sub>CN on Au

Using higher electron energies, desorption of other products from CH<sub>3</sub>CN is observed. See Figure 4.3. With 400 eV irradiation of 2 L pure CH<sub>3</sub>CN, desorption of *m/z* 16 (CH<sub>4</sub>) is observed. In addition, production of *m/z* 27 (HCN or C<sub>2</sub>H<sub>3</sub>) is seen near 128 K, which is near the desorption temperature of HCN ice [173]. A fragment of ethane (C<sub>2</sub>H<sub>3</sub>) is an alternative possibility for the assignment of *m/z* 27. Although *m/z* 27 could be a small cracking fragment of CH<sub>3</sub>CN upon electron ionization in the mass spectrometer, it would be expected to appear in coincidence with desorption of CH<sub>3</sub>CN itself. In Figure 4.3, a comparison of the new TPD peaks are shown with parent *m/z* 41 (CH<sub>3</sub>CN), whose desorption maximum temperature is ~147 K.

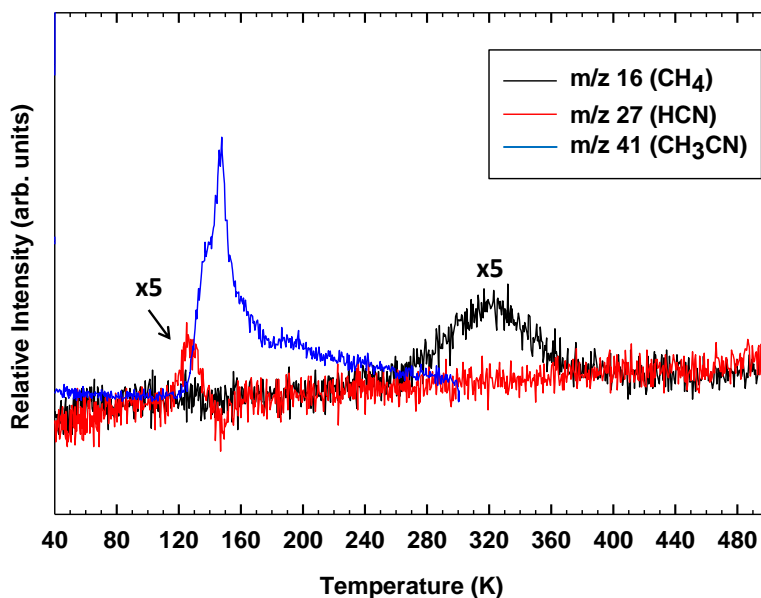


**Figure 4.3:** Post-irradiation TPD of *m/z* 16 (black), 27 (red), and 41 (blue) after deposition of 2 L CH<sub>3</sub>CN at 40 K and then 400 eV electron irradiation for 17 minutes. Ramp rate = 0.5 K/s.

### 4.3.3 TPD of m/z 2 and 4 From Electron Irradiation of Pure Acetylene ( $C_2D_2$ ) on Au

With 200 eV electron irradiation of pure  $C_2D_2$  (layered),  $D_2$  (m/z 4) and D (m/z 2) are produced as shown in Figure 4.4. Normal desorption of  $C_2D_2$  occurs at 90 K. However, m/z 2 desorbs after irradiation beginning almost immediately upon warm-up at ~45 K and continues until 90 K (Figure 4.4(A)). This is assigned as D, since the isotopic purity of the  $C_2D_2$  is 99+%. However, some isotopic exchange with background hydrogen could still occur producing  $H_2$  for m/z 2. As shown in Figure 4.4(B), m/z 4 ( $D_2$ ) does not begin desorption until 60-70 K and continues until 120 K. Larger products are not observed in the post-irradiation TPD from  $C_2D_2$ .

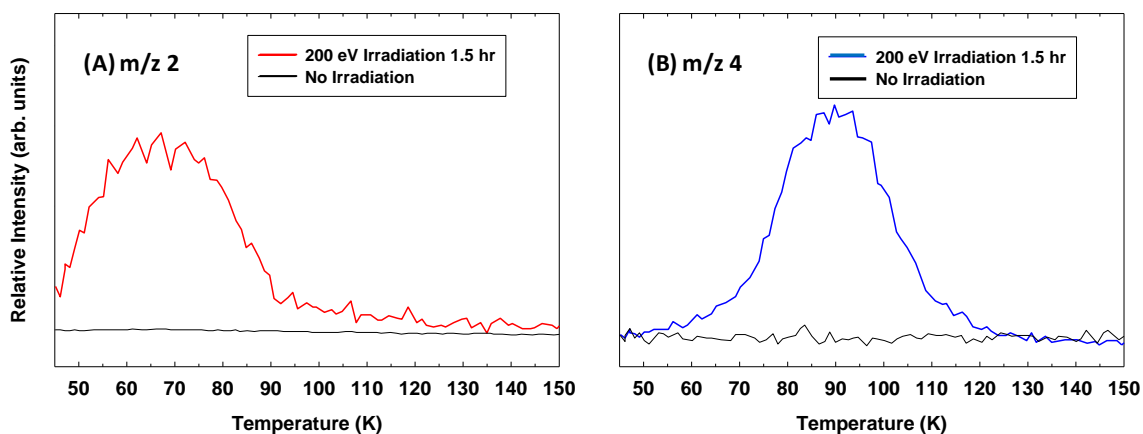


**Figure 4.4:** TPD of m/z 2 (A) and m/z 4 (B) after total deposition of 110 L  $C_2D_2$  (layered) at 40 K. TPD after no irradiation shown in black. TPD after 200 eV irradiation of the layers for a total of 1.5 hr shown in red (m/z 2) and blue (m/z 4). Ramp rate = 0.05 K/s.

#### 4.3.4 TPD From Electron Irradiation of Mixed Layered Ices ( $C_2D_2/CH_3CN$ ) on Au

Layered mixed ices ( $C_2D_2/CH_3CN$ ) were then irradiated and studied using post-irradiation TPD. For clarity, Figure 4.5 below gives a schematic representation of the ice layers deposited and irradiated. A control experiment contained the same layered ice but with no irradiation between layers. A total of 120 L  $C_2D_2$  and 120 L  $CH_3CN$  was deposited for each experiment.

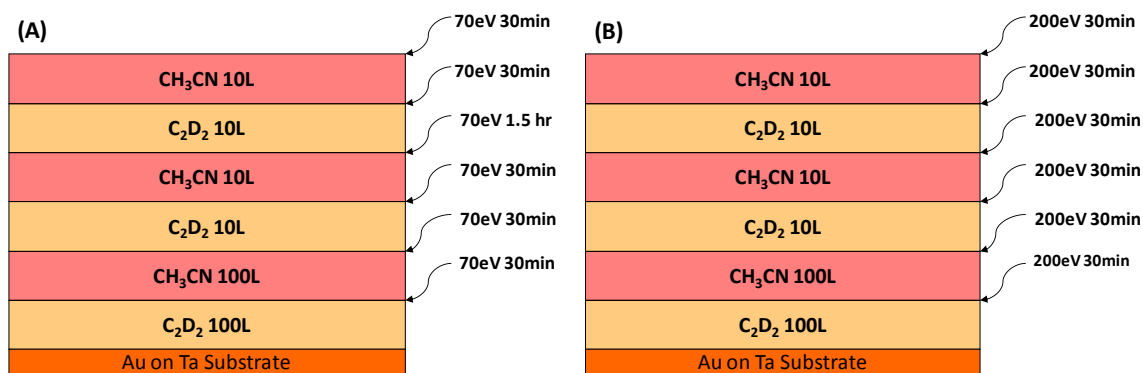


**Figure 4.5:** Schematic representation of the ice layers for the mixed ices as deposited and irradiated with electrons between each layer. (A) displays the 70 eV experiment and (B) displays the 200 eV experiment.

The post-irradiation 3D TPD for the above described experiments are shown in Figure 4.6(B,C) compared to the control with no irradiation (A). Figures 4.6(A-C) show TPD spectra plotted in 3D over the mass range (0-50  $m/z$ ). No new peaks for larger masses are observed. Mixed ices irradiated with 200 eV electrons again show  $D_2$  is produced, similar to pure  $C_2D_2$ . However, upon 70 eV irradiation,  $D_2$  is not observed in the TPD. See Figure 4.7 for single TPD of  $m/z$  4 for these experiments. Because TPD may not be the best method to observe larger products because they may not desorb easily, post-irradiation IR was also observed (Section 4.3.5).

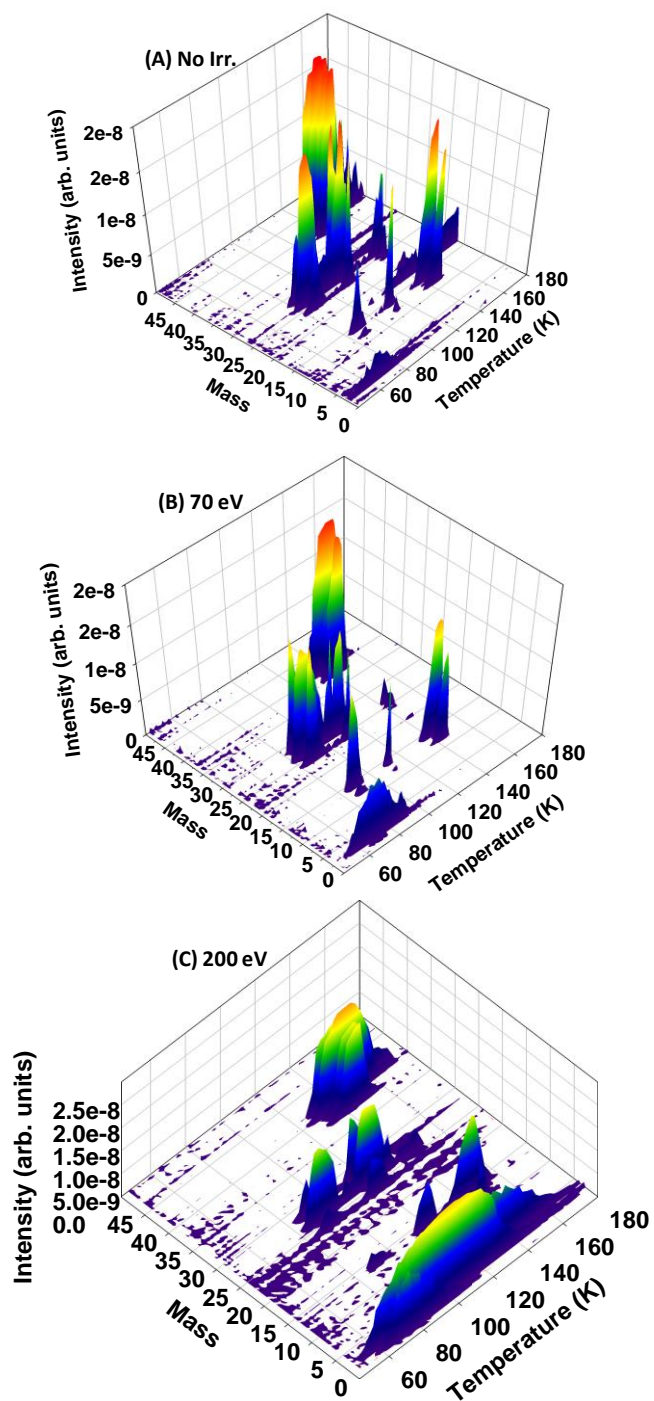


**Figure 4.6:** Post-irradiation 3D TPD for (A) no irradiation, (B) 70 eV irradiation, and (C) 200 eV irradiation after deposition of 120 L  $C_2D_2$  and 120 L  $CH_3CN$  (layered) at 40 K. Ramp rate = 0.05 K/s.

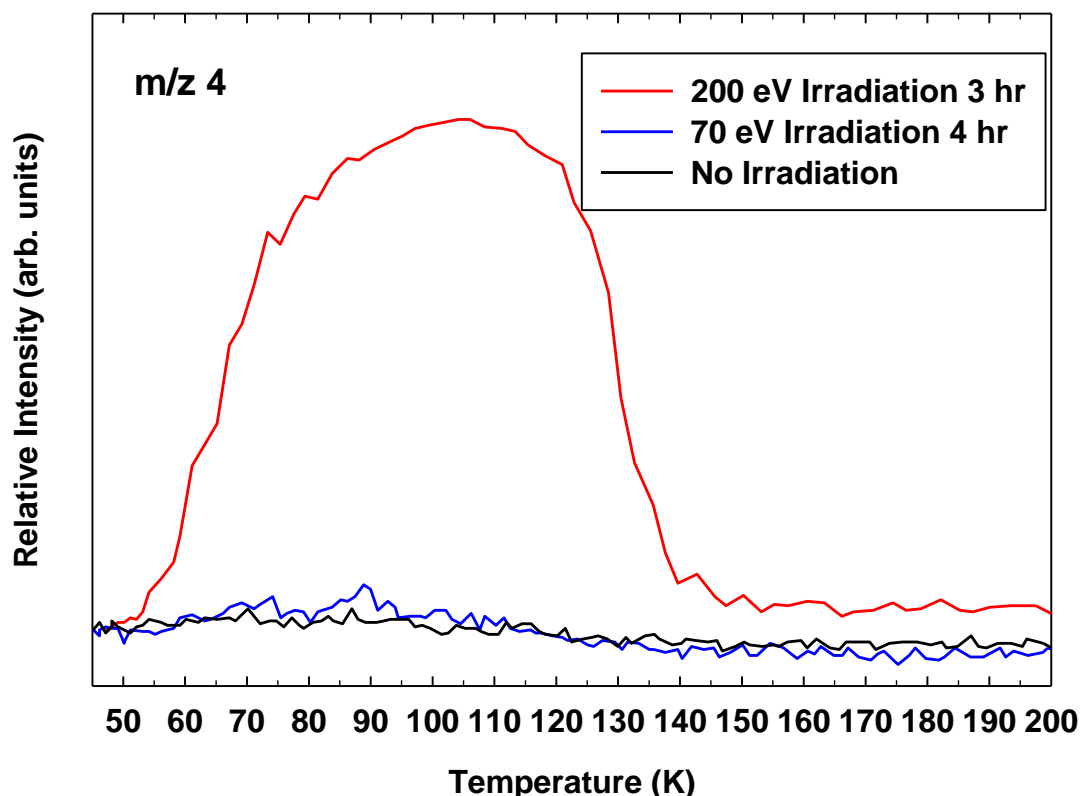


**Figure 4.7:** Single TPD comparison of  $m/z$  4 for  $D_2$  for no irradiation (black), 70 eV electrons (blue), and 200 eV electrons (red) after deposition of 120 L  $C_2D_2$  and 120 L  $CH_3CN$  (layered) at 40 K. Ramp rate = 0.05 K/s.

### 4.3.5 Infrared Spectra of Irradiated Mixtures on $SiO_2$

#### 4.3.5.1 IR After 400 eV Electron Irradiation of $C_2D_2/CH_3CN$

Figure 4.8 shows the IR spectra of a 1:0.75 mixture (1100 L  $C_2D_2$ :825 L  $CH_3CN$ ) (black). The three main  $CH_3CN$  peaks shown include the C-H asymmetric stretch at  $3001\text{ cm}^{-1}$ , the C-H symmetric stretch at  $2940\text{ cm}^{-1}$ , and the CN (triple-bonded) symmetric stretch at  $2251\text{ cm}^{-1}$  [174]. The main band for  $C_2D_2$  is the strong C-D stretch at  $2393\text{ cm}^{-1}$  shown in Figure 4.8 [175]. After 400 eV irradiation of the 1:0.75 ( $C_2D_2:CH_3CN$ ) mixed ice at 70 K, the IR difference spectra indicates that the

peaks of the starting species decrease with increasing irradiation time when subtracted from the original spectra. This subtraction method is described in Chapter 3 (Section 3.2). Desorption or decomposition of  $\text{CH}_3\text{CN}$  and  $\text{C}_2\text{D}_2$  occurs, but no new peaks (representing products) are seen which is consistent with the lack of large products seen in the post-irradiation TPD. From these results, it appears that  $\text{C}_2\text{D}_2$  mixed with  $\text{CH}_3\text{CN}$  is unreactive together after irradiation with low-energy electrons. Discussion can be found in Section 4.4.1.

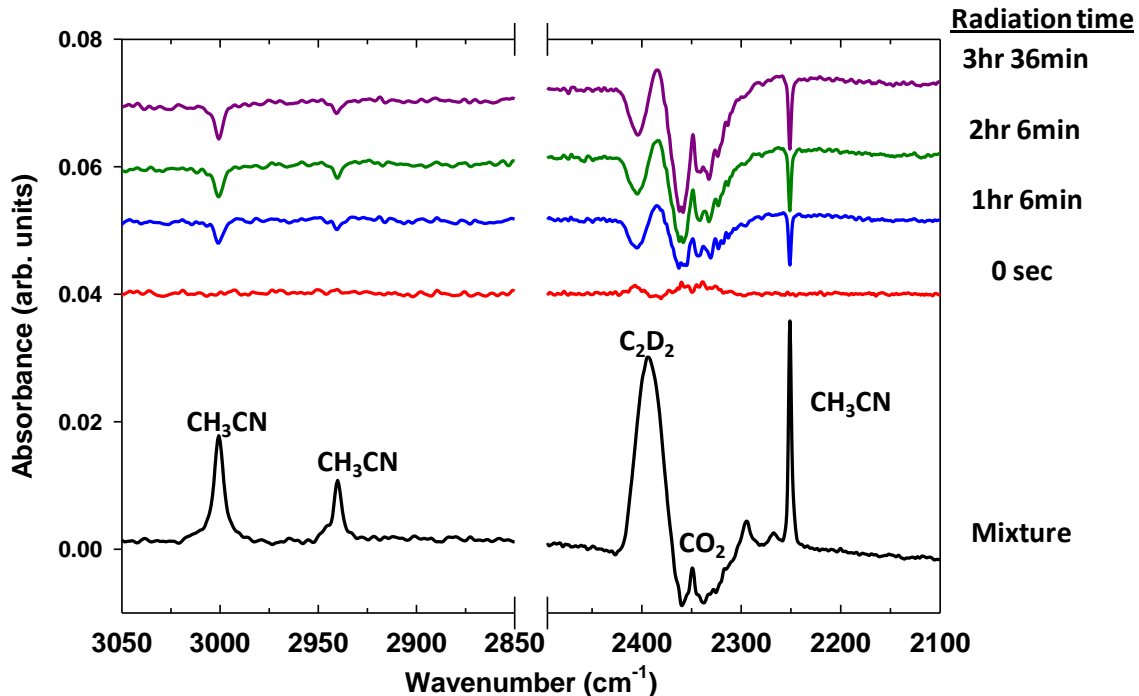


**Figure 4.8:** Infrared spectra of pre-irradiated 1:0.75 mixture (1100 L  $\text{C}_2\text{D}_2$ :825 L  $\text{CH}_3\text{CN}$ ) (black) compared to difference spectra (top four) taken as a function of 400 eV radiation time. The parent peaks of  $\text{CH}_3\text{CN}$  and  $\text{C}_2\text{D}_2$  decrease as a function of increasing radiation time.

#### 4.3.5.2 IR After 1 keV Electron Irradiation of C<sub>2</sub>D<sub>2</sub>/CH<sub>3</sub>CN

IR spectra of 1 keV electron irradiation of a 1:0.75 mixture (1100 L C<sub>2</sub>D<sub>2</sub>:825 L CH<sub>3</sub>CN) at 70 K is presented in Figure 4.9. The results were similar to the 400 eV irradiation. After 1 keV irradiation for 3 hrs, the IR spectra indicates that the parent species peaks decrease with increasing irradiation time when subtracted from the original spectra, but again no new peaks were observed which again is consistent with the lack of products seen with post-irradiation TPD. Note that CO<sub>2</sub> was a contaminant in the initial IR spectra before both electron irradiation experiments.

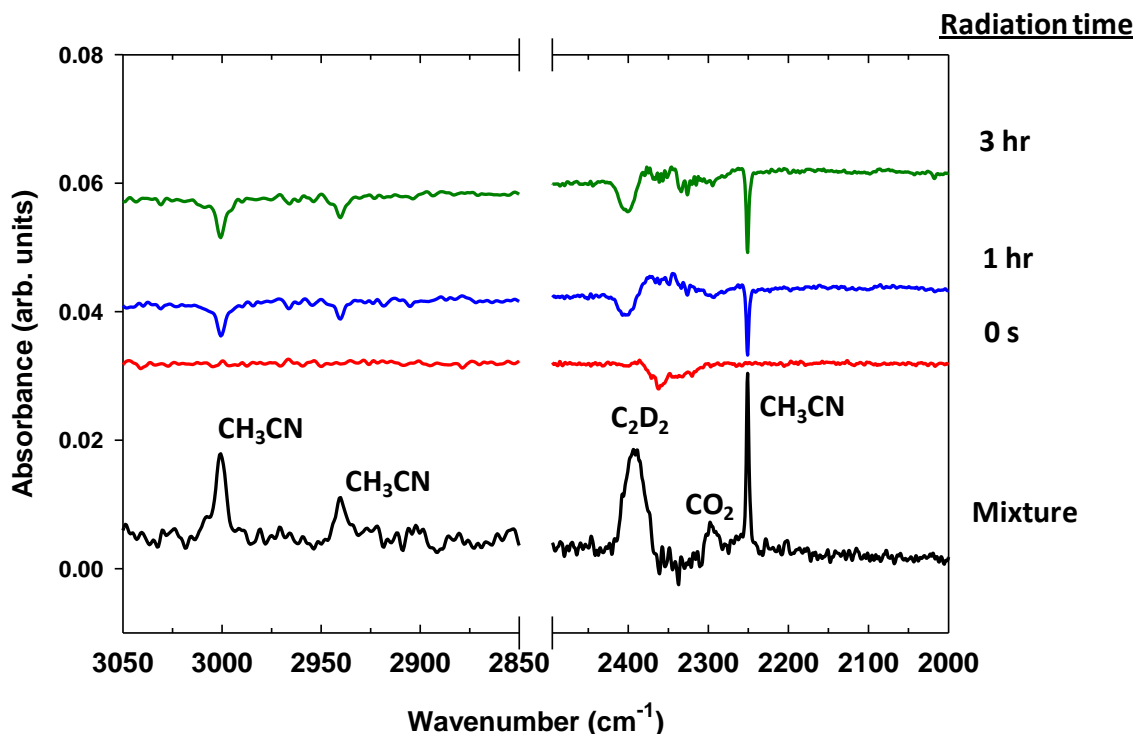


**Figure 4.9:** IR spectra of pre-irradiated 1:0.75 mixture (1100 L C<sub>2</sub>D<sub>2</sub>:825 L CH<sub>3</sub>CN) (black) compared to difference spectra (top three) taken as a function of 1 keV radiation time. The main peaks of CH<sub>3</sub>CN and C<sub>2</sub>D<sub>2</sub> decrease as a function of increasing radiation time.

#### 4.3.5.3 IR After Lyman- $\alpha$ Irradiation of C<sub>2</sub>D<sub>2</sub>/CH<sub>3</sub>CN

Infrared spectra after Lyman- $\alpha$  (10 eV) irradiation of a 1:0.75 mixture (1100 L C<sub>2</sub>D<sub>2</sub>:825 L CH<sub>3</sub>CN) also showed the photodesorption or photodecomposition of the parent ices. See Figure 4.10. Also, possibly two new unidentified peaks at 2175 and 2025 cm<sup>-1</sup> begin to grow after ~3 hr irradiation. The peak at 2025 cm<sup>-1</sup> could be <sup>-</sup>CN, a fragment of CH<sub>3</sub>CN, or due to H<sub>2</sub>C=C=NH, ketenimine, which forms from rearrangement of CH<sub>3</sub>CN [170]. However, these peaks did not further grow after 5.5 hr or 43 hr irradiation, which makes their validity unclear. In addition, the peaks are barely visible over the noise, which also makes it difficult to determine if they are real. See Section 4.4.1 for a complete discussion.

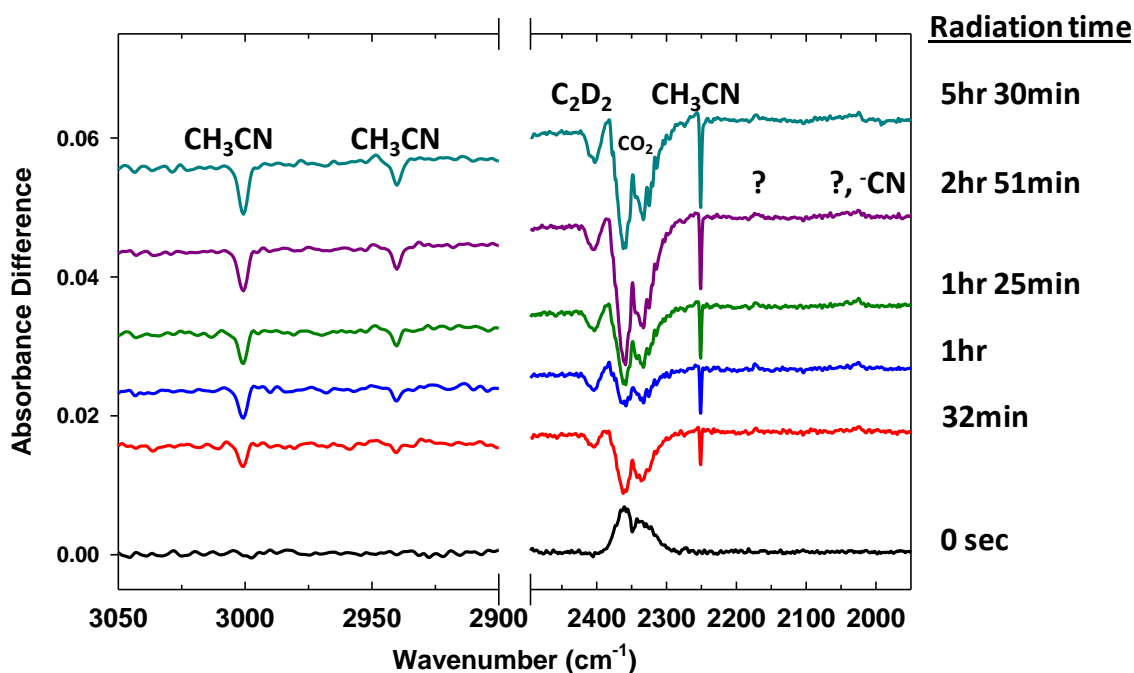


**Figure 4.10:** Infrared difference spectra of pre-irradiated 1:0.75 mixture (1100 L  $C_2D_2$ :825 L  $CH_3CN$ ) (black, 0 s) compared to difference spectra (top five) taken as a function of 10.2 eV Lyman- $\alpha$  radiation time. Negative peaks indicate loss of the parent species with irradiation.

#### 4.3.6 TPD of Acetylene Fragments From Mixed Ices on $SiO_2$

Upon taking background TPD measurements for the above-mentioned irradiation experiments, an interesting phenomena in the TPD of the mixed ices on  $SiO_2$  substrate was observed when compared to the pure  $C_2D_2$  TPD. Results are presented here and discussion is in Section 4.4.2. Figure 4.11 below gives the TPD of  $m/z$  24 after dosing a pure  $C_2D_2$  ice (black) compared to a mixed  $C_2D_2$ : $CH_3CN$  ice (red). The TPD of  $m/z$  24 is shown because it is a typical cracking fragment of  $C_2D_2$  (CC, triple-bonded). The parent mass ( $m/z$  28) of  $C_2D_2$  is not shown due to the contribution from background  $N_2$  and CO in the chamber.

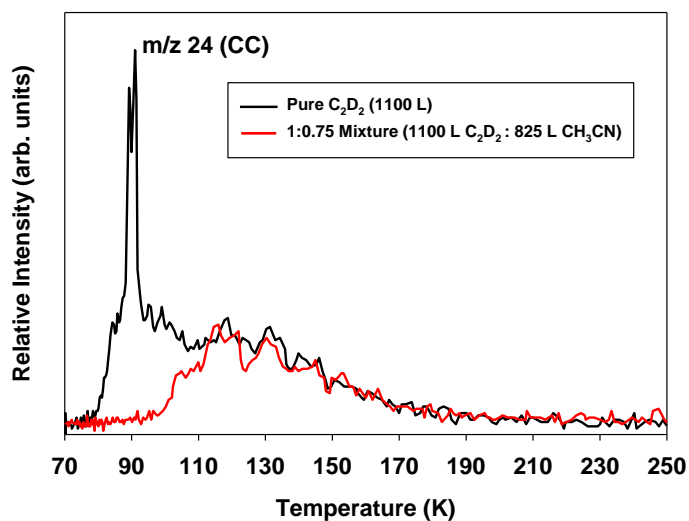


**Figure 4.11:** TPD for  $m/z$  24 (CC, triple-bonded) after dosing 1100 L pure  $C_2D_2$  (black) compared to 1:0.75 (1100 L  $C_2D_2$  : 825 L  $CH_3CN$ ) mixed ice (red). Ramp rates = 0.5 K/s.

For comparison, the TPD after dosing a mixture of  $C_2D_2:CO_2$  is compared with the pure  $C_2D_2$  in Figure 4.12. In addition, the TPD after dosing a mixture of  $C_2D_2:H_2O$  is compared with the pure  $C_2D_2$  in Figure 4.13. A sharp multilayer desorption peak is seen for the pure  $C_2D_2$  at  $\sim 90$  K. This peak is also seen in the  $C_2D_2:CO_2$  mixed ice, although weaker (Figure 4.12(blue)). This could be because  $CO_2$  also has a desorption temperature of about 80-90 K and carries  $C_2D_2$  with it upon warm-up, allowing  $C_2D_2$  to sublime. However, interestingly, for the mixed  $C_2D_2:CH_3CN$  ice, this 90 K multilayer desorption peak does not exist (Figure 4.11(red)). Also, in the  $C_2D_2:H_2O$  mixture, the 90 K is present but very weak (Figure 4.13(green)). For the  $C_2D_2:H_2O$  and  $C_2D_2:CH_3CN$  mixtures, a much broader peak from 110-170 K dominates.

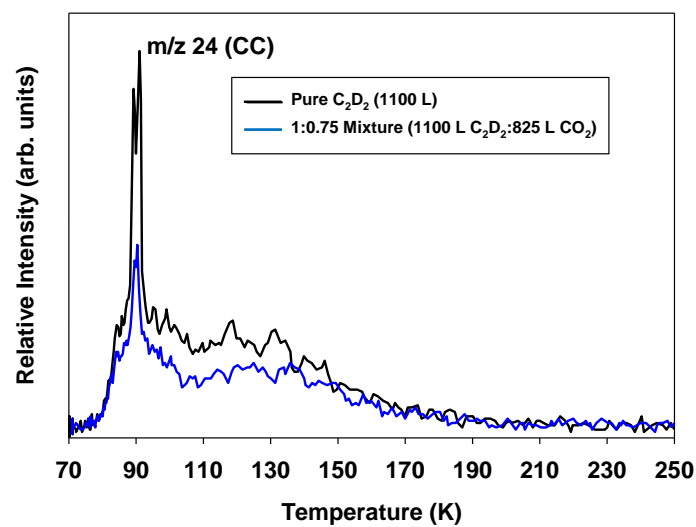


**Figure 4.12:** TPD for m/z 24 (CC, triple-bonded) after dosing 1100 L pure C<sub>2</sub>D<sub>2</sub> (black) compared to 1:0.75 (1100 L C<sub>2</sub>D<sub>2</sub> : 825 L CO<sub>2</sub>) mixed ice (blue). Ramp rates = 0.5 K/s.

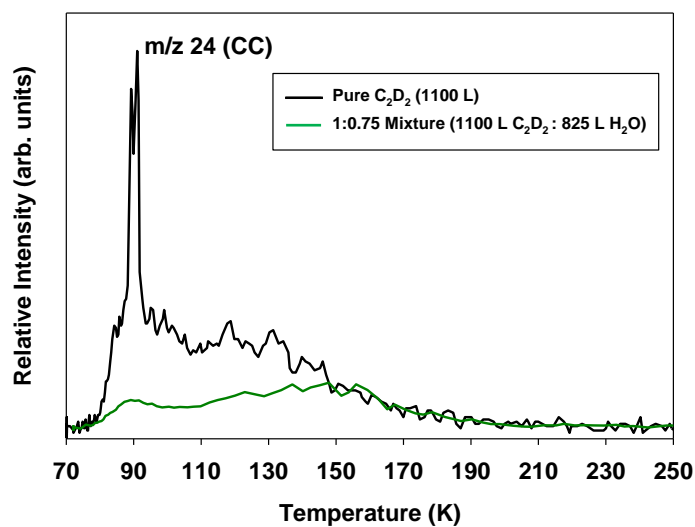


**Figure 4.13:** TPD for m/z 24 (CC, triple-bonded) after dosing 1100 L pure C<sub>2</sub>D<sub>2</sub> (black) compared to 1:0.75 (1100 L C<sub>2</sub>D<sub>2</sub> : 825 L H<sub>2</sub>O) mixed ice (green). Ramp rates = 0.5 K/s.

### 4.3.7 Coverage-dependent TPD of Acetylene on SiO<sub>2</sub>

Figure 4.14 shows the TPD of C<sub>2</sub>D<sub>2</sub> (m/z 24 for CC triple-bonded) from a SiO<sub>2</sub> nanopowder surface as a function of increasing coverage. These experiments were performed to determine the identification of the C<sub>2</sub>D<sub>2</sub> 90 K sharp peak as well as the broader 110-180 K peak seen in the mixed ices presented in Section 4.3.6. At high coverages, what is interpreted as a sharp multilayer peak ( $\alpha_1$ ) at ~90 K dominates. However, as coverage is decreased to 400 L (near monolayer coverage for this rough substrate), the  $\alpha_1$  peak at 90 K decreases, while the broader peak ( $\alpha_2$ ) (interpreted as monolayer peak) at higher temperature (110-180 K) grows. The  $\alpha_2$  peak is likely broad due to the influence of diffusion on the monolayer desorption of C<sub>2</sub>D<sub>2</sub> from SiO<sub>2</sub> nanopowder.

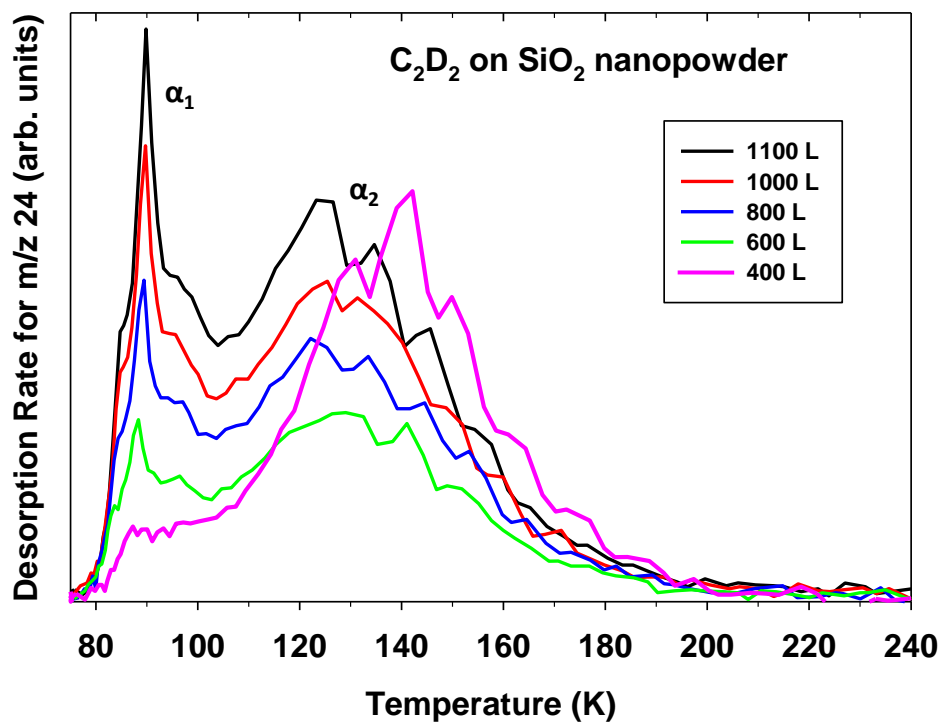


**Figure 4.14:** Coverage-dependent TPD of 400 to 1100 L C<sub>2</sub>D<sub>2</sub> (m/z 24 for CC triple-bonded) on SiO<sub>2</sub> nanopowder, showing two peaks representing multilayer ( $\alpha_1$ ) and monolayer ( $\alpha_2$ ) desorption. Ramp rate = 0.5 K/s.

## 4.4 Discussion

### 4.4.1 Irradiation of Pure and Mixed Ices

Low-energy electron processing of pure CH<sub>3</sub>CN on Au (Sections 4.3.1 and 4.3.2) produced H<sub>2</sub>, CH<sub>4</sub>, and HCN in post-irradiation TPD. Thus, in Titan's atmosphere or on its surface temperatures (below ~94 K), H<sub>2</sub> would be expected to be produced easily from electron-processed CH<sub>3</sub>CN ices. If produced, H<sub>2</sub> must further contribute to reactions on the surface [10], and it has actually been suggested to be consumed or gettered by methanogenic cycles or reactions involving microorganisms that *might* be present in the methane lakes [176]. H<sub>2</sub> abundances have been found by Cassini in the atmosphere [176] and could be the result of hydrogen abstraction of organic aerosols, tholins, or clouds by radiation processing. Also, the differences in desorption temperature from that of the parent mass (CH<sub>3</sub>CN) indicate that the degradation products (HCN, CH<sub>4</sub>) are produced in the ice from electron irradiation. HCN could be involved in tholin or polymer formation on the surface where temperatures are low, but because HCN desorbs above 120 K, it likely is not involved in tholin formation at atmospheric altitudes (mesosphere) where the temperature is higher. This data indicates that on Titan, possible cycling between CH<sub>3</sub>CN and HCN + CH<sub>4</sub> likely occurs, moderating the overall number densities of all three species in the atmosphere and at the surface.

Irradiation of C<sub>2</sub>D<sub>2</sub> (Section 4.3.3) induces fragmentation within the ice itself, producing the TPD of D<sub>2</sub> (m/z 4) that probably forms from two D atoms recombining in the ice with the additional energy provided by heating (TPD). This recombination could be initiated by thermal desorption, as evidenced by the desorption temperature of m/z 4 being slightly higher (begins at ~ 70 K). After irradiation and upon warm-up, any CCD•

that may be produced (although radicals are not directly observed) could be available to interact with other fragments to form larger polymers of  $C_2D_2$ , such as benzene or diacetylene, in the low-temperature ice. However, larger product formation was not confirmed with these experiments. The reason could be that high molecular weight molecules such as benzene are difficult to extract with TPD [52], and even more difficult if they are produced very inefficiently with the irradiation sources used. Another study that performed high electron energy irradiation of  $C_2H_2$  did show benzene in the IR spectra [167]. Interestingly, a non-irradiation TPD study of  $C_2D_2$  on Pd/W(211) showed negligible amounts of benzene production. The products they did see desorbed at high temperatures (350-400 K). The experiments performed here were monitored to 500 K, but desorption of benzene or other polymerization products were not observed above the noise.

Mixed ice layers of  $CH_3CN$  and  $C_2D_2$  appears relatively stable with 70 eV low-energy electron irradiation, while  $D_2$  is observed in the post-irradiation TPD after 200 eV irradiation (Section 4.3.4) of the layered ices.  $C_2D_2$  fragmentation is thus not quenched by the presence of  $CH_3CN$ . No larger products were observed from the mixed ices in post-irradiation TPD. The IR spectra of the mixed ices on  $SiO_2$  showed a definite decrease in both  $CH_3CN$  and  $C_2D_2$  after 400 eV and 1 keV electron irradiation, and this was also observed after Lyman- $\alpha$  irradiation. The destruction of  $C_2D_2$  could not be quantified since there are no reported IR band strengths for the bands of  $C_2D_2$  in the literature to date. Future irradiation experiments using  $C_2H_2$ , for which band strengths have been reported, would be beneficial. To quantitatively describe the destruction of  $CH_3CN$  with low-energy electrons compared to Lyman- $\alpha$  irradiation, taking into account

the relative penetration depths, see Tables 4.1 and 4.2 below. Table 4.1 reports the relative radiation doses on an eV/acetonitrile molecule basis, based on the equation [29]

$$D_{irr} = \frac{[\langle E_{irr} \rangle \phi_{abs} t]}{N_o}$$

previously described in detail in Chapter 3. Here the initial column density ( $N_o$ ) was for the 2252  $\text{cm}^{-1}$  band of  $\text{CH}_3\text{CN}$ , based on the reported band strength of  $A = 2.2 \times 10^{-18} \text{ cm mol}^{-1}$  [170]. Note that this  $A$  could be a source of error since it was not measured in a mixed ice. The original  $N_o$  for each experiment was then divided by 2, since only one side of the sample was irradiated and then multiplied by a ratio (the penetration depth of the electrons or photons divided by the total thickness of the ice) to provide the corrected  $N_o$  based on the depth of the ice irradiated. The estimated penetration depths were 12 nm for 400 eV, 51 nm for 1 keV, and 100 nm for Lyman- $\alpha$ . The  $t$  for electron irradiation was based on rastering the e-gun over the  $3.75 \text{ cm}^{-1}$  sample 42 times (for 400 eV, 3.5 hr experiment) or 36 times (for 1 keV, 3 hr experiment), producing 60 s or 52 s, respectively for each experiment, as the total time ( $t$ ) of irradiation of the rastered sample. This made the total eV/acetonitrile molecule doses much lower for the electron experiments compared to the Lyman- $\alpha$  experiment. Also note that the total eV/acetonitrile molecule dose is less for the 1 keV experiment (5069 eV/molecule) compared to the 400 eV experiment (7364 eV/molecule), since more acetonitrile molecules were sampled by 1 keV electrons due to the deeper penetration depth of the higher energy electrons. Note that these energy doses are in units of eV/acetonitrile molecule and do not account for dose received by acetylene.

**Table 4.1:** Comparison of Lyman- $\alpha$  and electron irradiation total energy doses on an eV/acetonitrile molecule basis for 1:0.75 C<sub>2</sub>D<sub>2</sub>:CH<sub>3</sub>CN mixed ice, based on the initial column density of CN stretch of CH<sub>3</sub>CN at 2252 cm<sup>-1</sup>. See text for explanation of calculation.

Ice Composition	3.5 hr 400 eV electrons	3 hr 1 keV electrons	5.5 hr Lyman- $\alpha$
1:0.75 (C <sub>2</sub> D <sub>2</sub> :CH <sub>3</sub> CN)	7.36 x 10 <sup>3</sup>	5.07 x 10 <sup>3</sup>	1.45 x 10 <sup>4</sup>

Next, the normalized column densities ( $N$ ) for the 2252 cm<sup>-1</sup> band of CH<sub>3</sub>CN before and after each irradiation experiment (400 eV electrons, 1 keV electrons, and Lyman- $\alpha$ ) were calculated and are reported in Table 4.2 below. All  $N$ s were normalized to the initial  $N$  of CH<sub>3</sub>CN before the Lyman- $\alpha$  experiment ( $9.17 \times 10^{16}$  molecules/cm<sup>2</sup>), to allow for direct comparison. From Table 4.2, it is apparent that for each experiment there was a loss in CH<sub>3</sub>CN after irradiation, regardless of electrons or photons. However, the trend from these three experiments appears to be with a higher eV/molecule dose, there is a higher survival yield of CH<sub>3</sub>CN. This unusual result deserves further energy-dependent studies. A recently published study [177] reported the desorption cross section (cm<sup>2</sup>) for 250, 300, 350, and 400 eV electron irradiation of pure CH<sub>3</sub>CN ice. They saw an increase in desorption cross section after 300 eV irradiation compared to higher irradiation energies, which they attributed to resonant electron scattering due to the C 1s core orbital occurring near ~280 eV [177]. This could explain the higher  $N$  after 400 eV electrons compared to the 1 keV experiment. This does not explain, however, the higher column density seen after Lyman- $\alpha$  irradiation, which could be caused by rearrangement or reformation of the CH<sub>3</sub>CN upon Lyman- $\alpha$  photolysis (or error due to used band strength). As a result, the parent bands of CH<sub>3</sub>CN may not show as much desorption upon

photolysis. Coincidentally, the above-mentioned study also did not see products upon low-energy electron irradiation of pure CH<sub>3</sub>CN [177].

**Table 4.2:** Normalized column densities<sup>a</sup> ( $N$ ) of 2252 cm<sup>-1</sup> band of CH<sub>3</sub>CN for 1:0.75 C<sub>2</sub>D<sub>2</sub>:CH<sub>3</sub>CN mixed ice before and after irradiation with 400 eV electrons, 1 keV electrons, and Lyman- $\alpha$  irradiation.

Experiments	<sup>b</sup> $N$ of 2252 cm <sup>-1</sup> band of CH <sub>3</sub> CN
Before 400 eV electrons	<sup>c</sup> 9.17 x 10 <sup>16</sup>
After 3.5 hr 400 eV electrons	<sup>c</sup> 6.35 x 10 <sup>16</sup>
Before 1 keV electrons	<sup>d</sup> 9.17 x 10 <sup>16</sup>
After 3 hr 1 keV electrons	<sup>d</sup> 4.47 x 10 <sup>16</sup>
Before Lyman- $\alpha$	9.17 x 10 <sup>16</sup>
After 5.5 hr Lyman- $\alpha$	7.12 x 10 <sup>16</sup>

<sup>a</sup>Column densities in units of molecules/cm<sup>2</sup>

<sup>b</sup>Calculated using band strength,  $A = 2.2 \times 10^{-18}$  cm/molecules as reported by Hudson and Moore. [170]

<sup>c</sup>Normalized by multiplying original ( $N$ )s by 1.37

<sup>d</sup>Normalized by multiplying original ( $N$ )s by 1.88

The growth of two weak IR peaks (2175 and 2025 cm<sup>-1</sup>) in the mixed ice with Lyman- $\alpha$  irradiation could represent <sup>-</sup>CN, a fragment of CH<sub>3</sub>CN, or H<sub>2</sub>C=C=NH (ketenimine) resulting from the rearrangement of CH<sub>3</sub>CN, possibly accounting for the low loss of CH<sub>3</sub>CN after Lyman- $\alpha$  irradiation. Another possibility for the peak at 2025 cm<sup>-1</sup> is a small amount of cyanoacetylene (HC<sub>3</sub>N) formation with the high dose of Lyman- $\alpha$  irradiation (see Table 4.1). The main CC (triple-bonded) stretch of HC<sub>3</sub>N would be expected at 2030 cm<sup>-1</sup>. However, this result is unclear from these experiments since the weak peak we see is hard to distinguish from the noise level, and HC<sub>3</sub>N was not observed in post-irradiation TPD or in IR spectra upon warm-up (not shown). Thus, if produced, the yield would be very low.

#### 4.4.2 Acetylene Trapping

As shown in Section 4.3.7, thick pure  $C_2D_2$  ice TPD experiments on  $SiO_2$  show that  $C_2D_2$  has a multilayer peak  $\sim 90$  K, confirmed by a lack of the 90 K peak in low coverage experiments (Figure 4.14). The 90 K peak disappears when  $C_2D_2$  is complexed or trapped within a  $CH_3CN$  ice matrix, regardless of mixing ratio (Figure 4.11). Co-adsorption of  $C_2D_2$  with  $H_2O$  also allowed significant trapping of the  $C_2D_2$  in the ice matrix until  $\sim 110$  K (Figure 4.13). However, a weak 90 K multilayer peak in the case of the water mixture was observed.  $CO_2:C_2D_2$  mixtures do not produce complexation or trapping, and the 90 K multilayer peak is still seen (Figure 4.12). It is known that below 45 K, solid  $C_2H_2$  is amorphous, while crystallization occurs starting at 50 K, before sublimation (or desorption) rapidly occurs near 85-90 K. However, the TPD data here shows that  $C_2H_2$  on  $SiO_2$  has a broad monolayer feature from 110-180 K ( $\alpha_2$ , Figure 4.14), indicating a monolayer interaction with the substrate. This monolayer interaction could play a role in the lack of the 90 K multilayer feature in  $CH_3CN$  and  $H_2O$  co-adsorbed ices possibly preventing  $C_2H_2$  multilayer crystalline formation. There have been no other studies to date on the ice interaction between  $C_2H_2$  and  $CH_3CN$ ; however, Silva and Devlin[178] reported on the interaction of  $C_2H_2$  with  $H_2O$ . They suggested a strong interaction in which a dimer forms ( $H_2O-C_2H_2$ ) with acetylene “acting as a proton donor to dangling-oxygen coordination sites on the ice surface,” with an estimated bond energy of  $\sim 4$  kcal/mol [178]. Since  $CH_3CN$  is also a polar molecule, it could behave in a similar way with  $C_2H_2$ , which warrants further study.

Interestingly, electron and Lyman- $\alpha$  post-irradiation TPD experiments showed that radiation processing does not change the trapping of acetylene that occurs when

mixed with acetonitrile or water (not shown). The acetylene trapping that occurs in  $C_2D_2:CH_3CN$  and  $C_2D_2:H_2O$  mixed ices indicates that mixed organics on the surface of Titan can have a different sublimation behavior than pure ices. This trapping suggests that acetylene could exist within some organic mixtures (negating radiation processing) on Titan's surface (~94 K).

#### 4.5 Conclusions

Investigations into the possible prebiotic pathways of acetylene and acetonitrile to simulate thermal and radiation chemistry on Titan have been presented. Molecular hydrogen/deuterium TPD yields in all ices are higher compared to experiments with no electron irradiation. Thus, electron irradiation dissociates the parent pure and mixed ices. In all experiments, hydrogen or deuterium desorbs from the ices ~60-140 K. In the case of  $CH_3CN$  ice, degradation to  $CH_4$  and  $HCN$  is the major pathway as evidenced by TPD. This is in agreement with a prior UV study by Hudson and Moore [170]. Irradiation of pure  $C_2D_2$  ice produces  $D_2$ . The organic radicals can then react to form small abundances of larger polymers such as diacetylene and benzene, but this is not confirmed with our experiments. For the mixed layered  $CH_3CN/C_2D_2$  ices, larger products are also not confirmed. However, the IR spectra after electron and Lyman- $\alpha$  irradiation of  $CH_3CN:C_2D_2$  mixed ices show that desorption of the parent species occurs. Surprisingly, the column density of  $CH_3CN$  after Lyman- $\alpha$  irradiation ( $7.12 \times 10^{16}$  molecule/cm<sup>2</sup>) shows less loss compared to electron irradiation ( $6.35 \times 10^{16}$  molecule/cm<sup>2</sup>). In addition, very weak peaks possibly representing  $\dot{C}N$ , ketenimine, or cyanoacetylene are observed after Lyman- $\alpha$  irradiation of the mixed ice, but these were unconfirmed in the TPD. From these results,  $HC_3N$  cannot be suggested as a product of  $C_2H_2 + CH_3CN$  on Titan. An

alternative reaction to be explored in the future would be HCN with  $C_2H_2$ . HCN, also present in Titan's atmosphere, would provide a more accessible cyano- group that fragmented  $C_2H_2$  could interact with to produce  $HC_3N$ . Finally, trapping of acetylene has been shown to be prevalent in acetonitrile or water-containing ices, which could have implications for acetylene's presence and sublimation within mixed ices on Titan's surface.

## CHAPTER V

### CONCLUDING REMARKS

One main objective of this thesis has been to yield new information regarding the reactions of formamide and other prebiotically-relevant molecules with surfaces and within ices. Indeed, this dissertation has investigated the adsorption, thermal behavior, and radiation (both photon and electron) processing of formamide in two related but distinct studies. With these works, this thesis serves to fill some of the gaps in the literature regarding formamide as it may have existed on early Earth and as it may behave in astrophysical environments. A separate, third investigation has studied acetylene and acetonitrile organic mixed ices to simulate possible prebiotic reactions that may occur on Titan in the outer solar system. Since only few studies [167,170,179] have reported the radiation chemistry of mixed ices under cold conditions relevant to Titan, this investigation adds valuable laboratory-based work for understanding Titan's chemistry. All projects herein have involved the use of transmission FT-IR spectroscopy and controlled TPD experiments under UHV conditions.

The first study explores thermal interactions of formamide with a clay mineral, kaolinite. Our collaborators have also calculated the theoretical harmonic infrared frequencies using M05-2X/6-31G(d), 6-31G(d,p), and 6-31+G(d,p) levels of density functional theory, and general agreement with experiment has been found for condensed formamide and the formamide-kaolinite surface complexes. The kaolinite OH IR band positions change as a function of temperature, which have been previously correlated

with surface reconstructions and changes in interlayer bond distances in the kaolinite. We found that formamide's interaction with the exposed and interlayer surfaces of kaolinite can be probed directly using the temperature dependence of the kaolinite–OH and formamide IR vibrational frequencies. Samples dosed directly with formamide show that the C=O stretching feature is broadened and shifts to lower frequency at low temperatures (67–90 K). The NH and CH stretches of formamide are also very weak at these temperatures. We interpret these features as manifestations of hydrogen bonding between the Al–OH octahedral kaolinite face (inner surface OH group) and formamide's carbonyl group. Intercalation and subsequent bonding may be facilitated by the increased O–H···O bond lengths between kaolinite lattices and increased availability of Al–OH sites in the low-temperature regime. At 100–110 K, the C=O feature sharpens and shifts to a higher frequency, while the NH and CH stretches become more distinct. Thus, with increasing temperature, formamide diffusion and formamide–formamide interactions become more dominant. TPD analysis gives a mean binding energy of  $11.7 \pm 0.24$  kcal/mol, which agrees well with the calculated values of adsorption energy and indicates strong physisorption. One significant finding of this work is the preferential binding of formamide to kaolinite's octahedral surface. This binding behavior could affect the catalytic reaction of formamide with kaolinite as it leads to nucleobases and other prebiotic species.

The second study explores formamide chemistry from an astrophysical stand-point as it may occur in interstellar ices. This is the first study of formamide's Lyman- $\alpha$  and electron processing. The adsorption, thermal rearrangement, Lyman- $\alpha$  (121 nm) and low-energy electron processing of formamide ( $\text{HCONH}_2$ ,  $\text{DCONH}_2$ ,

HCOND<sub>2</sub>) pure and mixed ices on high-surface-area SiO<sub>2</sub> nanoparticles have been investigated to mimic the possible interstellar reactions occurring on icy grains. Pure formamide ice seems to display at least three different phases over the 70-460 K temperature range studied: (1) a porous phase from ~70-145 K, (2) a compacted polycrystalline phase from ~145-210 K, and (3) a pre-melting phase from ~210-380 K before complete desorption occurs at ~460 K. The TPD peak maximum is at ~228 K, and a mean  $E_{\text{act}}$  of  $\sim 14.7 \pm 0.17$  kcal/mol ( $0.64 \pm 0.007$  eV) was obtained using Redhead analysis from the TPD. Lyman- $\alpha$  processing of pure HCONH<sub>2</sub> ice forms primarily OCN<sup>-</sup> and CO at 70 K. OCN<sup>-</sup> and CO are also produced in ice annealed to 165 K; however, the OCN<sup>-</sup>/CO combined products are ~25% less abundant. Photo-processing also produces H<sub>2</sub> that is released from the ice between ~90-140 K. A smaller H<sub>2</sub> TPD peak is seen for the irradiated formamide ice annealed to 165 K, indicating that ~54% less H<sub>2</sub> is produced in the crystalline ice. Warm-up experiments also indicate that OCN<sup>-</sup> and CO desorb together at ~220 K, indicating that volatile products can be trapped within the formamide ice. The SiO<sub>2</sub> substrate may affect the dissociation channels and enhance the H + H recombination in the ices during irradiation. The OCN<sup>-</sup> assignment and lack of other products such as NH<sub>3</sub>, NH<sub>4</sub><sup>+</sup> and HCN indicates very different chemistry for condensed phase compared to the gas-phase dissociation channels of formamide. The results also have implications for the specific production of OCN<sup>-</sup> in interstellar water-dominated ices where formamide is present. In addition, Lyman- $\alpha$  photolysis of HCONH<sub>2</sub>:H<sub>2</sub>O mixed ices interestingly suggests a catalytic role by the H<sub>2</sub>O in OCN<sup>-</sup> and CO production. Also, electron irradiation increases the yield of OCN<sup>-</sup> while CO decarboxylation is selectively prevented. A dissociative electron attachment (DEA) mechanism could be involved. The

IR spectral assignments and approximate column densities reported in this study can assist analysis of observational infrared data (e.g., *Infrared Space Observatory*, *Spitzer Space Telescope*, and the soon-to-be launched *James Webb Space Telescope*), and thus could be significant to the astrophysical community.

Finally, a related investigation that does not involve formamide has been presented. Titan is a fascinating satellite of Saturn in the outer solar system, especially since it may be a present-day system where organic-based prebiotic chemistry occurs. To understand the radiation and thermal chemistry that occurs there, laboratory-based simulations are warranted. Thus, a study of acetylene and acetonitrile trapping and condensed phase radiation chemistry has been investigated [180]. Results indicate that hydrogen yields are higher in all cases compared to experiments with no irradiation. However, in all experiments hydrogen desorbs very early on after production. Regardless of this, proton abstraction from these organics upon radiation processing is very prevalent and radical or ion chemistry with other reactive species on Titan could result. In the case of pure  $\text{CH}_3\text{CN}$  ice, degradation to  $\text{CH}_4$  and  $\text{HCN}$  is a major radiation damage pathway. In addition, the lack of radiation chemistry that is found to occur between acetylene and acetonitrile is interesting and leads to more questions about the formation of molecules such as cyanoacetylene. Finally, a major finding of this work is the ability of acetonitrile and water to trap acetylene in mixed ices.

Based on the knowledge obtained from this research, future studies might investigate the following areas. First, since there are additional gaps in the literature regarding binding characteristics and energies for adsorption of formamide on other mineral surfaces [11] (e.g.,  $\text{Fe}_3\text{P}$  minerals, pyrite, feldspars, micas, zircon, sulfides, iron

oxides, olivine, quartz, etc.), these TPD experiments would be beneficial to the prebiotic and surface science communities. In addition, since formamide is not the only molecule that could have been a precursor to biomolecules on early Earth, interactions between other simple molecules (e.g., HCN, NH<sub>3</sub>, CH<sub>4</sub>, N<sub>2</sub>, H<sub>2</sub>O etc.) and potentially catalytic minerals should be investigated. Surface science studies of *mixtures* of these simple molecules on catalytic mineral surfaces would also be extremely beneficial to the community. From there, UV and thermal-cycling experiments could be included. Second, formamide's astrophysical relevance appears to be growing, with its identification in several interstellar environments [9]. The results presented here indicate that future work should focus on formamide:water ice studies to further elucidate the mechanism. In addition, isotopic radiation studies could shed light on some of the pathways discussed herein. An additional opportunity for further work would be to understand the lack of the decarboxylation channel upon electron irradiation. Finally, future research simulating Titan chemistry should look to other molecules, such as HCN, as a possible precursor to cyanoacetylene. Although many avenues are available for further study, this thesis has aimed and successfully contributed to understanding the adsorption and thermal and radiation pathways of several systems relevant to prebiotic and astrophysical environments.

## REFERENCES

- [1] Dugal, P.-C.; Abdoul-Carime, H.; Sanche, L. *The Journal of Physical Chemistry B* **2000**, *104*, 5610-5617.
- [2] Arumainayagam, C. R.; Lee, H.-L.; Nelson, R. B.; Haines, D. R. *Surface Science Reports* **2010**, *65*, 1-44.
- [3] Krasnopolsky, V. A. *Icarus* **2009**, *201*, 226-256.
- [4] Danger, G.; Plasson, R.; Pascal, R. *Chemical Society Reviews* **2012**, *41*, 5416-5429.
- [5] Bean, H. D.; Anet, F. A. L.; Gould, I. R.; Hud, N. V. *Origins of Life and Evolution of the Biosphere* **2006**, *36*, 39-63.
- [6] Burton, A. S.; Stern, J. C.; Elsila, J. E.; Glavin, D. P.; Dworkin, J. P. *Chemical Society Reviews* **2012**, *41*, 5459-5472.
- [7] Robertson, M. P.; Miller, S. L. *Nature* **1995**, *375*, 772-774.
- [8] Saladino, R.; Crestini, C.; Pino, S.; Costanzo, G.; Di Mauro, E. *Physics of Life Reviews* **2012**, *9*, 84-104.
- [9] Halfen, D. T.; Ilyushin, V.; Ziurys, L. M. *Astrophysical Journal* **2011**, *743*, 12.
- [10] Clark, R. N.; Curchin, J. M.; Barnes, J. W.; Jaumann, R.; Soderblom, L.; Cruikshank, D. P.; Brown, R. H.; Rodriguez, S.; Lunine, J.; Stephan, K.; Hoefen, T. M.; Le Mouelic, S.; Sotin, C.; Baines, K. H.; Buratti, B. J.; Nicholson, P. D. *Journal of Geophysical Research-Planets* **2010**, *115*.
- [11] Hazen, R. M.; Papineau, D.; Leeker, W. B.; Downs, R. T.; Ferry, J. M.; McCoy, T. J.; Sverjensky, D. A.; Yang, H. X. *American Mineralogist* **2008**, *93*, 1693-1720.
- [12] Aquino, A. J. A.; Tunega, D.; Gerzabek, M. H.; Lischka, H. *Journal of Physical Chemistry B* **2004**, *108*, 10120-10130.
- [13] Saladino, R.; Crestini, C.; Costanzo, G.; Negri, R.; Di Mauro, E. *Bioorganic & Medicinal Chemistry* **2001**, *9*, 1249-1253.
- [14] Saladino, R.; Ciambecchini, U.; Crestini, C.; Costanzo, G.; Negri, R.; Di Mauro, E. *ChemBiochem* **2003**, *4*, 514-521.

- [15] Saladino, R.; Crestini, C.; Ciambecchini, U.; Ciciriello, F.; Costanzo, G.; Di Mauro, E. *Chembiochem* **2004**, *5*, 1558-1566.
- [16] Saladino, R.; Crestini, C.; Neri, V.; Brucato, J. R.; Colangeli, L.; Ciciriello, F.; Di Mauro, E.; Costanzo, G. *Chembiochem* **2005**, *6*, 1368-1374.
- [17] Saladino, R.; Neri, V.; Crestini, C.; Costanzo, G.; Graciotti, M.; Di Mauro, E. *Journal of Molecular Evolution* **2010**, *71*, 100-110.
- [18] Goulding, A. D.; Alexander, D. M.; Bauer, F. E.; Forman, W. R.; Hickox, R. C.; Jones, C.; Mullaney, J. R.; Trichas, M. *Astrophysical Journal* **2012**, *755*, 8.
- [19] Gibb, E. L.; Whittet, D. C. B.; Schutte, W. A.; Boogert, A. C. A.; Chiar, J. E.; Ehrenfreund, P.; Gerakines, P. A.; Keane, J. V.; Tielens, A.; van Dishoeck, E. F.; Kerkhof, O. *Astrophysical Journal* **2000**, *536*, 347-356.
- [20] Olofsson, J.; Juhasz, A.; Henning, T.; Mutschke, H.; Tamanai, A.; Moor, A.; Abraham, P. *Astronomy & Astrophysics* **2012**, *542*, A90.
- [21] Burke, D. J.; Brown, W. A. *Physical Chemistry Chemical Physics* **2010**, *12*, 5947-5969.
- [22] Barks, H. L.; Buckley, R.; Grieves, G. A.; Di Mauro, E.; Hud, N. V.; Orlando, T. M. *Chembiochem* **2010**, *11*, 1240-1243.
- [23] Schutte, W. A.; Allamandola, L. J.; Sandford, S. A. *Science* **1993**, *259*, 1143-1145.
- [24] Brucato, J. R.; Baratta, G. A.; Strazzulla, G. *Astronomy & Astrophysics* **2006**, *455*, 395-399.
- [25] Lunine, J. I.; Horst, S. M. *Rendiconti Lincei-Scienze Fisiche E Naturali* **2011**, *22*, 183-189.
- [26] Cable, M. L.; Horst, S. M.; Hodyss, R.; Beauchamp, P. M.; Smith, M. A.; Willis, P. A. *Chemical Reviews* **2012**, *112*, 1882-1909.
- [27] Raulin, F.; Brasse, C.; Poch, O.; Coll, P. *Chemical Society Reviews* **2012**, *41*, 5380-5393.
- [28] Moore, M. H.; Hudson, R. L. *IAU Colloquium* **2005**, *231*, 119-132.
- [29] Gerakines, P. A.; Moore, M. H.; Hudson, R. L. *Astronomy and Astrophysics* **2000**, *357*, 793-800.

- [30] Allamandola, L. J.; Bernstein, M. P.; Sandford, S. A.; Walker, R. L. *Space Science Reviews* **1999**, *90*, 219-232.
- [31] Gerakines, P. A.; Moore, M. H.; Hudson, R. L. *Journal of Geophysical Research-Planets* **2001**, *106*, 33381-33385.
- [32] Chen, Y. J.; Nuevo, M.; Hsieh, J. M.; Yih, T. S.; Sun, W. H.; Ip, W. H.; Fung, H. S.; Chiang, S. Y.; Lee, Y. Y.; Chen, J. M.; Wu, C. Y. R. *Astronomy & Astrophysics* **2007**, *464*, 253-257.
- [33] Rajappan, M.; Yuan, C.; Yates, J. T. *Journal of Chemical Physics* **2011**, *134*, 10.
- [34] Ciesla, F. J.; Sandford, S. A. *Science* **2012**, *336*, 452-454.
- [35] Shepperd, K. R. LOW-ENERGY ELECTRON INDUCED PROCESSES IN HYDROCARBON FILMS ADSORBED ON SILICON SURFACES, Georgia Institute of Technology, 2009.
- [36] Novozamsky, J. H.; Schutte, W. A.; Keane, J. V. *Astronomy & Astrophysics* **2001**, *379*, 588-591.
- [37] Harris, D. C. *Symmetry and spectroscopy : an introduction to vibrational and electronic spectroscopy*; Dover Publications: New York :, 1989.
- [38] Christian, G. D. *Analytical Chemistry*, 6th ed.; John Wiley & Sons, Inc.: USA, 2004.
- [39] Chabal, Y. J. *Surface Science Reports* **1988**, *8*, 211-357.
- [40] Andanson, J. M.; Baiker, A. *Chemical Society Reviews* **2010**, *39*, 4571-4584.
- [41] Mul, G.; Kapteijn, F.; Moulijn, J. A. *Carbon* **1999**, *37*, 401-410.
- [42] Trenary, M. *Annual Review of Physical Chemistry* **2000**, *51*, 381-403.
- [43] Abbott, H. L.; Uhl, A.; Baron, M.; Lei, Y.; Meyer, R. J.; Stacchiola, D. J.; Bondarchuk, O.; Shaikhutdinov, S.; Freund, H. J. *Journal of Catalysis* **2010**, *272*, 82-91.
- [44] Spoto, G.; Bordiga, S.; Zecchina, A.; Cocina, D.; Gribov, E. N.; Regli, L.; Groppo, E.; Lamberti, C. *Catalysis Today* **2006**, *113*, 65-80.
- [45] Zhuang, J.; Rusu, C. N.; Yates, J. T. *Journal of Physical Chemistry B* **1999**, *103*, 6957-6967.

- [46] Shenoy, S. S.; Whittet, D. C. B.; Ives, J. A.; Watson, D. M. *Astrophysical Journal Supplement Series* **2008**, *176*, 457-466.
- [47] Boogert, A. C. A.; Pontoppidan, K. M.; Knez, C.; Lahuis, F.; Kessler-Silacci, J.; van Dishoeck, E. F.; Blake, G. A.; Augereau, J. C.; Bisschop, S. E.; Bottinelli, S.; Brooke, T. Y.; Brown, J.; Crapsi, A.; Evans, N. J., II; Fraser, H. J.; Geers, V.; Huard, T. L.; Jorgensen, J. K.; Oberg, K. I.; Allen, L. E.; Harvey, P. M.; Koerner, D. W.; Mundy, L. G.; Padgett, D. L.; Sargent, A. I.; Stapelfeldt, K. R. *Astrophysical Journal* **2008**, *678*, 985-1004.
- [48] Pontoppidan, K. M.; Boogert, A. C. A.; Fraser, H. J.; van Dishoeck, E. F.; Blake, G. A.; Lahuis, F.; Oberg, K. I.; Evans, N. J., II; Salyk, C. *Astrophysical Journal* **2008**, *678*, 1005-1031.
- [49] Oberg, K. I.; Boogert, A. C. A.; Pontoppidan, K. M.; Blake, G. A.; Evans, N. J.; Lahuis, F.; van Dishoeck, E. F. *Astrophysical Journal* **2008**, *678*, 1032-1041.
- [50] NASA. The James Webb Space Telescope, <http://www.jwst.nasa.gov/>, **2012**.
- [51] Woodruff, D. P. *Modern techniques of surface science*, 2nd ed. ed.; Cambridge University Press: Cambridge, 1994.
- [52] Hanley, L.; Kornienko, O.; Ada, E. T.; Fuoco, E.; Trevor, J. L. *Journal of Mass Spectrometry* **1999**, *34*, 705-723.
- [53] Kautto, E.; Kuhalainen, J.; Manninen, M. *Physica Scripta*. **1997**, *55*, 628-633.
- [54] Redhead, P. A. *Vacuum* **1962**, *12*, 203-211.
- [55] de Jong, A. M.; Niemantsverdriet, J. M. *Surface Science* **1990**, *233*, 355-365.
- [56] Dawley, M. M.; Michalkova Scott, A.; Hill, F. C.; Leszczynski, J.; Orlando, T. M. *Journal of Physical Chemistry C* **2012**, *116*, 23981-23991.
- [57] Michalkova Scott, A.; Dawley, M. M.; Hill, F. C.; Orlando, T. M.; Leszczynski, J. *Journal of Physical Chemistry C* **2012**, *116*, 23992-24005.
- [58] Dawley, M. M.; Pirim, C.; Orlando, T. M. *Journal of Physical Chemistry A* **2013**, (to be submitted).
- [59] Dawley, M. M.; Pirim, C.; Orlando, T. M. *Journal of Physical Chemistry A* **2013**, (to be submitted).
- [60] Saladino, R.; Crestini, C.; Ciciriello, F.; Pino, S.; Costanzo, G.; Di Mauro, E. *Research in Microbiology* **2009**, *160*, 441-448.

- [61] Nguyen, V. S.; Abbott, H. L.; Dawley, M. M.; Orlando, T. M.; Leszczynski, J.; Nguyen, M. T. *Journal of Physical Chemistry A* **2010**, *115*, 841-851.
- [62] Raunier, S.; Chiavassa, T.; Duvernay, F.; Borget, F.; Aycard, J. P.; Dartois, E.; d'Hendecourt, L. *Astronomy & Astrophysics* **2004**, *416*, 165-169.
- [63] Saladino, R.; Crestini, C.; Costanzo, G.; DiMauro, E. On the prebiotic synthesis of nucleobases, nucleotides, oligonucleotides, Pre-RNA and Pre-DNA molecules. In *Prebiotic Chemistry: From Simple Amphiphiles to protocell Models*; Walde, P., Ed., 2005; Vol. 259; pp 29-68.
- [64] Saladino, R.; Crestini, C.; Ciciriello, F.; Costanzo, G.; Di Mauro, E. *Origins of Life and Evolution of the Biosphere* **2006**, *36*, 523-531.
- [65] Bear, F. E. *Chemistry of the soil*, 2nd ed.; Reinhold Pub. Corp.: New York, 1964.
- [66] Frost, R. L.; Kristof, J.; Horvath, E.; Klopogge, J. T. *Clay Minerals* **2000**, *35*, 443-454.
- [67] Frost, R. L.; Forsling, W.; Holmgren, A.; Klopogge, J. T.; Kristof, J. *Journal of Raman Spectroscopy* **1998**, *29*, 1065-1069.
- [68] Johnston, C. T.; Kogel, J. E.; Bish, D. L.; Kogure, T.; Murray, H. H. *Clays and Clay Minerals* **2008**, *56*, 470-485.
- [69] Frost, R. L.; Kristof, J.; Paroz, G. N.; Klopogge, J. T. *Journal of Physical Chemistry B* **1998**, *102*, 8519-8532.
- [70] Frost, R. L.; Kristof, J.; Paroz, G. N.; Klopogge, J. T. *Journal of Colloid and Interface Science* **1998**, *208*, 216-225.
- [71] Frost, R. L.; Tran, T. H.; Kristof, J. *Clay Minerals* **1997**, *32*, 587-596.
- [72] Thompson, J. G. *Clays and Clay Minerals* **1985**, *33*, 173-180.
- [73] Komori, Y.; Sugahara, Y.; Kuroda, K. *Journal of Materials Research* **1998**, *13*, 930-934.
- [74] Liu, Q. F.; Ding, S. L. *Acta Mineralogica Sinica* **1997**, *17*, 276-279.
- [75] Linjiang, W.; Daqing, W.; Peng, Y.; Zhiwei, C.; Zhong, C. *Chinese Science Bulletin* **2002**, *47*, 504-508.
- [76] Johnston, C. T.; Agnew, S. F.; Bish, D. L. *Clays and Clay Minerals* **1990**, *38*, 573-583.

- [77] Horvath, E.; Kristof, J.; Frost, R. L. *Applied Spectroscopy Reviews* **2010**, *45*, 130-147.
- [78] Bish, D. L.; Johnston, C. T. *Clays and Clay Minerals* **1993**, *41*, 297-304.
- [79] Frost, R. L.; Tran, T. H.; Rintoul, L.; Kristof, J. *Analyst* **1998**, *123*, 611-616.
- [80] Frost, R. L.; Lack, D. A.; Paroz, G. N.; Tran, T. H. T. *Clays and Clay Minerals* **1999**, *47*, 297-303.
- [81] Frost, R. L.; Kristof, J.; Horvath, E.; Klopogge, J. T. *Spectroch. Act. Part A-Mol. Biomol. Spectrosc.* **2000**, *56*, 1191-1204.
- [82] Wang, L. J.; Wu, D. Q.; Yuan, P.; Lin, Z. Y.; Diao, G. Y.; Peng, J. L. *Chemical Journal of Chinese Universities-Chinese* **2002**, *23*, 1948-1951.
- [83] Horvath, E.; Kristof, J.; Frost, R. L.; Jakab, E.; Mako, T.; Vagvolgyi, V. *Journal of Colloid and Interface Science* **2005**, *289*, 132-138.
- [84] Gabor, M.; Toth, M.; Kristof, J.; Komaromihiller, G. *Clays and Clay Minerals* **1995**, *43*, 223-228.
- [85] Zhao, Y.; Truhlar, D. G. *Theoretical Chemistry Accounts* **2008**, *120*, 215-241.
- [86] Zhao, Y.; Schultz, N. E.; Truhlar, D. G. *J. Chem. The. Comp.* **2006**, *2*, 364-382.
- [87] Zhao, Y.; Truhlar, D. G. The Minnesota Density Functionals and their Applications to Problems in Mineralogy and Geochemistry. In *Theoretical and Computational Methods in Mineral Physics: Geophysical Applications*; Wentzcovitch, R. S. L., Ed., 2010; Vol. 71; pp 19-37.
- [88] Rassolov, V. A.; Ratner, M. A.; Pople, J. A.; Redfern, P. C.; Curtiss, L. A. *Journal of Computational Chemistry* **2001**, *22*, 976-984.
- [89] Frisch, M. J.; Trucks, G. W.; Schlegel, H. B.; Scuseria, G. E.; Robb, M. A.; Cheeseman, J. R.; Scalmani, G.; Barone, V.; Mennucci, B.; Petersson, G. A.; Nakatsuji, H.; Caricato, M.; Li, X.; Hratchian, H. P.; Izmaylov, A. F.; Bloino, J.; Zheng, G.; Sonnenberg, J. L.; Hada, M.; Ehara, M.; Toyota, K.; Fukuda, R.; Hasegawa, J.; Ishida, M.; Nakajima, T.; Honda, Y.; Kitao, O.; Nakai, H.; Vreven, T.; Montgomery, J., J. A.; Peralta, J. E.; Ogliaro, F.; Bearpark, M.; Heyd, J. J.; Brothers, E.; Kudin, K. N.; Staroverov, V. N.; Kobayashi, R.; Normand, J.; Raghavachari, K.; Rendell, A.; Burant, J. C.; Iyengar, S. S.; Tomasi, J.; Cossi, M.; Rega, N.; Millam, N. J.; Klene, M.; Knox, J. E.; Cross, J. B.; Bakken, V.; Adamo, C.; Jaramillo, J.; Gomperts, R.; Stratmann, R. E.; Yazyev, O.; Austin, A. J.; Cammi, R.; Pomelli, C.; Ochterski, J. W.; Martin, R. L.; Morokuma, K.; Zakrzewski, V. G.; Voth, G. A.; Salvador, P.; Dannenberg, J. J.; Dapprich, S.;

- Daniels, A. D.; Farkas, Ö.; Foresman, J. B.; Ortiz, J. V.; Cioslowski, J.; Fox, D. J. Gaussian 09, Revision A.1; Gaussian, Inc.: Wallingford CT, 2009.
- [90] Merrick, J. P.; Moran, D.; Radom, L. *Journal of Physical Chemistry A* **2007**, *111*, 11683-11700.
- [91] El-Sayed, K.; Heiba, Z. K.; Abdel-Rahman, A. M. *Crystal Research and Technology* **1990**, *25*, 305-312.
- [92] Balan, E.; Delattre, S.; Guillaumet, M.; Salje, E. K. H. *American Mineralogist* **2010**, *95*, 1257-1266.
- [93] Suzuki, I. *Bulletin of the Chemical Society of Japan* **1960**, *33*, 1359-1365.
- [94] McNaughton, D.; Evans, C. J.; Lane, S.; Nielsen, C. J. *Journal of Molecular Spectroscopy* **1999**, *193*, 104-117.
- [95] Evans, J. C. *Journal of Chemical Physics* **1954**, *22*, 1228-1234.
- [96] King, S. T. *Journal of Physical Chemistry* **1971**, *75*, 405-410.
- [97] Brummel, C. L.; Shen, M. H.; Hewett, K. B.; Philips, L. A. *J. Opt. Soc. Amer. B - Opt. Phys.* **1994**, *11*, 176-183.
- [98] Rasanen, M. *Journal of Molecular Structure* **1983**, *101*, 275-286.
- [99] Fogarasi, G.; Balazs, A. *Theochem-J. Mol. Struct.* **1985**, *26*, 105-123.
- [100] Ricchiardi, G.; Damin, A.; Bordiga, S.; Lamberti, C.; Spano', G.; Rivetti, F.; Zecchina, A. *Journal of the American Chemical Society* **2001**, *123*, 11409-11419.
- [101] Kubicki, J. D.; Kwon, K. D.; Paul, K. W.; Sparks, D. L. *Euro. J. Soil Sci.* **2007**, *58*, 932-944.
- [102] Balan, E.; Saitta, A. M.; Mauri, F.; Calas, G. *American Mineralogist* **2001**, *86*, 1321-1330.
- [103] Campos, R. B.; Wypych, F.; Martins, H. P. *International Journal of Quantum Chemistry* **2011**, *111*, 2137-2148.
- [104] Olejnik, S.; Posner, A. M.; Quirk, J. P. *Clays and Clay Minerals* **1971**, *19*, 83-94.
- [105] Frost, R. L.; Kristof, J.; Horvath, E.; Klopogge, J. T. *Langmuir* **2001**, *17*, 3216-3222.

- [106] Frost, R. L.; Kristof, J.; Rintoul, L.; Kloprogge, J. T. *Spectrochimica Acta Part a-Molecular and Biomolecular Spectroscopy* **2000**, *56*, 1681-1691.
- [107] Mardyukov, A.; Sanchez-Garcia, E.; Rodziewicz, P.; Doltsinis, N. L.; Sander, W. *Journal of Physical Chemistry A* **2007**, *111*, 10552-10561.
- [108] Gao, Q. Y.; Erley, W.; Sander, D.; Ibach, H.; Hemminger, J. C. *Journal of Physical Chemistry* **1991**, *95*, 205-211.
- [109] Gottlieb, C. A.; Palmer, P.; Rickard, L. J.; Zuckerma, B. *Astrophysical Journal* **1973**, *182*, 699-710.
- [110] Hollis, J. M.; Lovas, F. J.; Remijan, A. J.; Jewell, P. R.; Ilyushin, V. V.; Kleiner, I. *Astrophysical Journal* **2006**, *643*, L25-L28.
- [111] deVicente, P.; MartinPintado, J.; Wilson, T. L. *A hot ring in the Sgr B2 molecular cloud*, 1996; Vol. 102.
- [112] Jones, B. M.; Bennett, C. J.; Kaiser, R. I. *Astrophysical Journal* **2011**, *734*.
- [113] Bernstein, M. P.; Allamandola, L. J.; Sandford, S. A. "Complex organics in laboratory simulations of interstellar/cometary ices", 1997.
- [114] Bernstein, M. P.; Sandford, S. A.; Allamandola, L. J.; Chang, S.; Scharberg, M. A. *Astrophysical Journal* **1995**, *454*, 327-344.
- [115] Gerakines, P. A.; Moore, M. H.; Hudson, R. L. *Icarus* **2004**, *170*, 202-213.
- [116] Brucato, J. R.; Strazzulla, G.; Baratta, G. A.; Rotundi, A.; Colangeli, L. *Origins of Life and Evolution of the Biosphere* **2006**, *36*, 451-457.
- [117] Ferus, M.; Kubelik, P.; Civis, S. *Journal of Physical Chemistry A* **2011**, *115*, 12132-12141.
- [118] Lundell, J.; Krajewska, M.; Rasanen, M. *Journal of Physical Chemistry A* **1998**, *102*, 6643-6650.
- [119] Maier, G.; Endres, J. *European Journal of Organic Chemistry* **2000**, 1061-1063.
- [120] Duvernay, F.; Trivella, A.; Borget, F.; Coussan, S.; Aycard, J. P.; Chiavassa, T. *Journal of Physical Chemistry A* **2005**, *109*, 11155-11162.
- [121] Petersen, C.; Dahl, N. H.; Jensen, S. K.; Poulsen, J. A.; Thogersen, J.; Keiding, S. R. *Journal of Physical Chemistry A* **2008**, *112*, 3339-3344.

- [122] Leach, S.; Jochims, H. W.; Baumgartel, H. *Journal of Physical Chemistry A* **2010**, *114*, 4847-4856.
- [123] Lu, J. F.; Wu, Y. F.; Yu, Z. Y.; Lin, X. J. *Russian Journal of Physical Chemistry A* **2011**, *85*, 1384-1389.
- [124] Cataldo, F.; Lilla, E.; Ursini, O.; Angelini, G. *Journal of Analytical and Applied Pyrolysis* **2010**, *87*, 34-44.
- [125] Cataldo, F.; Patane, G.; Compagnini, G. *Journal of Macromolecular Science Part a-Pure and Applied Chemistry* **2009**, *46*, 1039-1048.
- [126] Miyakawa, S.; Cleaves, H. J.; Miller, S. L. *Origins of Life and Evolution of the Biosphere* **2002**, *32*, 195-208.
- [127] Benilan, Y.; Gazeau, M.-C.; Es-Sabbar, E.-T.; Jolly, A.; Arzoumanian, E.; Fray, N.; Cottin, H. *EPSC-DPS Joint Meeting Abstracts* **2011**, *6*.
- [128] Fogarasi, G.; Balazs, A. *Theochem-Journal of Molecular Structure* **1985**, *26*, 105-123.
- [129] Mortensen, A.; Nielsen, O. F.; Yarwood, J.; Shelley, V. *Journal of Physical Chemistry* **1994**, *98*, 5221-5226.
- [130] Itoh, K.; Shimanouchi, T. *Journal of Molecular Spectroscopy* **1972**, *42*, 86-99.
- [131] Torrie, B. H.; Brown, B. A. *Journal of Raman Spectroscopy* **1994**, *25*, 183-187.
- [132] Parmeter, J. E.; Schwalke, U.; Weinberg, W. H. *Journal of the American Chemical Society* **1988**, *110*, 53-62.
- [133] Hudson, R. L.; Khanna, R. K.; Moore, M. H. *Astrophysical Journal Supplement Series* **2005**, *159*, 277-281.
- [134] Khanna, R. K.; Lowenthal, M. S.; Ammon, H. L.; Moore, M. H. *Astrophysical Journal Supplement Series* **2002**, *140*, 457-464.
- [135] Ikeura-Sekiguchi, H.; Sekiguchi, T.; Kitajima, Y.; Baba, Y. *Applied Surface Science* **2001**, *169*, 282-286.
- [136] Sivaraman, B.; Raja Sekhar, B. N.; Jones, N. C.; Hoffmann, S. V.; Mason, N. J. *Chemical Physics Letters* **2012**, *554*, 57-59.
- [137] Flores, C. R.; Gao, Q. Y.; Hemminger, J. C. *Surface Science* **1990**, *239*, 156-168.
- [138] Ladell, J.; Post, B. *Acta Crystallographica* **1954**, *7*, 559-564.

- [139] Liu, M. H.; Chen, C.; Liu, C. W. *Structural Chemistry* **2004**, *15*, 309-315.
- [140] Fogarasi, G. *Journal of Molecular Structure* **2011**, *978*, 257-262.
- [141] Ding, Y.; Chu, X.; Hong, X.; Zou, P.; Liu, Y. *Applied Physics Letters* **2012**, *100*, 013701.
- [142] Niznansky, D.; Rehspringer, J. L. *Journal of Non-Crystalline Solids* **1995**, *180*, 191-196.
- [143] King, D. A. *Surface Science* **1975**, *47*, 384-402.
- [144] Raunier, S. A.; Chiavassa, T.; Marinelli, F.; Allouche, A.; Aycard, J. P. *Journal of Physical Chemistry A* **2003**, *107*, 9335.
- [145] Gerakines, P. A.; Schutte, W. A.; Greenberg, J. M.; Vandishoeck, E. F. *Astronomy & Astrophysics* **1995**, *296*, 810.
- [146] Loeffler, M. J.; Baragiola, R. A. *Journal of Chemical Physics* **2010**, *133*.
- [147] Gingell, J. M.; Mason, N. J.; Zhao, H.; Walker, I. C.; Siggel, M. R. F. *Chemical Physics* **1997**, *220*, 191-205.
- [148] Tan, G. L.; Lemon, M. F.; French, R. H. *Journal of the American Ceramic Society* **2003**, *86*, 1885-1892.
- [149] Pirronello, V.; Biham, O.; Liu, C.; Shen, L. O.; Vidali, G. *Astrophysical Journal* **1997**, *483*, L131-L134.
- [150] Pirronello, V.; Liu, C.; Shen, L. Y.; Vidali, G. *Astrophysical Journal* **1997**, *475*, L69-L72.
- [151] Jheeta, S.; Ptasinska, S.; Sivaraman, B.; Mason, N. J. *Chemical Physics Letters* **2012**, *543*, 208-212.
- [152] Bossa, J. B.; Theule, P.; Duvernay, F.; Borget, F.; Chiavassa, T. *Astronomy & Astrophysics* **2008**, *492*, 719-724.
- [153] Pendleton, Y. J.; Tielens, A.; Tokunaga, A. T.; Bernstein, M. P. *Astrophysical Journal* **1999**, *513*, 294-304.
- [154] Theule, P.; Duvernay, F.; Ilmane, A.; Hasegawa, T.; Morata, O.; Coussan, S.; Danger, G.; Chiavassa, T. *Astronomy & Astrophysics* **2011**, *530*.

- [155] McGibbon, G. A.; Burgers, P. C.; Terlouw, J. K. *International Journal of Mass Spectrometry* **1994**, *136*, 191-208.
- [156] Maeda, S.; Matsuda, Y.; Mizutani, S.; Fujii, A.; Ohno, K. *Journal of Physical Chemistry A* **2011**, *114*, 11896-11899.
- [157] Hamann, T.; Edtbauer, A.; da Silva, F. F.; Denifl, S.; Scheier, P.; Swiderek, P. *Physical Chemistry Chemical Physics* **2011**, *13*, 12305-12313.
- [158] Goumans, T. P. M.; Gianturco, F. A.; Sebastianelli, F.; Baccarelli, I.; Rivail, J. L. *Journal of Chemical Theory and Computation* **2009**, *5*, 217-221.
- [159] Zhang, W.; Du, B.; Feng, C. *Journal of Molecular Structure* **2004**, *679*, 121.
- [160] Schutte, W. A.; Khanna, R. K. *Astronomy & Astrophysics* **2003**, *398*, 1049-1062.
- [161] Liu, D.; Fang, W. H.; Fu, X. Y. *Chemical Physics Letters* **2000**, *318*, 291-297.
- [162] van der Rest, G.; Mourgues, P.; Nedev, H.; Audier, H. E. *Journal of the American Chemical Society* **2002**, *124*, 5561-5569.
- [163] Nguyen, V. S.; Leszczynski, J.; Orlando, T. M.; Nguyen, M. T. **2013**, (*to be submitted*).
- [164] Gauvin, R.; Hovongton, P.; Drouin, D.; Horny, P.; Demers, H.; Couture, A. R. monte CARlo SIMulation of electroN trajectory in sOLids; 2.0 ed. Université de Sherbrooke, 2000.
- [165] Lattelais, M.; Pauzat, F.; Ellinger, Y.; Ceccarelli, C. *Astronomy & Astrophysics* **2011**, *519*, 7.
- [166] Leach, S.; Jochims, H. W.; Baumgartel, H. *Journal of Physical Chemistry A*, *114*, 4847-4856.
- [167] Zhou, L.; Zheng, W. J.; Kaiser, R. I.; Landera, A.; Mebel, A. M.; Liang, M. C.; Yung, Y. L. *Astrophysical Journal* **2010**, *718*, 1243-1251.
- [168] Gronoff, G.; Lilensten, J.; Desorgher, L.; Fluckiger, E. *Astronomy and Astrophysics* **2009**, *506*, 955-964.
- [169] López-Moreno, J. J.; Molina-Cuberos, G. J.; Hamelin, M.; Grard, R.; Simões, F.; Godard, R.; Schwingenschuh, K.; Béghin, C.; Berthelier, J. J.; Brown, V. J. G.; Falkner, P.; Ferri, F.; Fulchignoni, M.; Jernej, I.; Jerónimo, J. M.; Rodrigo, R.; Trautner, R. *Geophys. Res. Lett.* **2008**, *35*, L22104.
- [170] Hudson, R. L.; Moore, M. H. *Icarus* **2004**, *172*, 466-478.

- [171] Ipolyi, I.; Michaelis, W.; Swiderek, P. *Physical Chemistry Chemical Physics* **2007**, *8*, 180-191.
- [172] Menor-Salvan, C.; Ruiz-Bermejo, M.; Osuna-Esteban, S.; Munoz-Caro, G.; Veintemillas-Verdaguer, S. *Chemistry & Biodiversity* **2008**, *5*, 2729-2739.
- [173] Moore, M. H.; Ferrante, R. F.; Moore, W. J.; Hudson, R. *Astrophysical Journal Supplement Series* **2010**, *191*, 96-112.
- [174] DelloRusso, N.; Khanna, R. K. *Icarus* **1996**, *123*, 366-395.
- [175] Bottger, G. L.; Eggers, D. F. *Journal of Chemical Physics* **1964**, *40*, 8.
- [176] Courtin, R.; Sim, C. K.; Kim, S. J.; Gautier, D. *Planetary and Space Science* **2012**, *69*, 89-99.
- [177] Abdulgalil, A. G. M.; Marchione, D.; Rosu-Finsen, A.; Collings, M. P.; McCoustra, M. R. S. *Journal of Vacuum Science & Technology A* **2012**, *30*.
- [178] Silva, S. C.; Devlin, J. P. *The Journal of Physical Chemistry* **1994**, *98*, 10847-10852.
- [179] Kim, Y. S.; Bennett, C. J.; Chen, L. H.; O'Brien, K.; Kaiser, R. I. *Astrophysical Journal*, *711*, 744-756.
- [180] Dawley, M. M.; Orlando, T. M. **2013**, (*unpublished work*).